INVESTIGATION OF A RADIANTLY HEATED AND COOLED OFFICE WITH AN

INTEGRATED DESICCANT VENTILATION UNIT

A Dissertation

by

XIANGYANG GONG

Submitted to the Office of Graduate Studies of
Texas A&M University
in partial fulfillment of the requirements of the degree of

DOCTOR OF PHILOSOPHY

August 2007

Major Subject: Mechanical Engineering

INVESTIGATION OF A RADIANTLY HEATED AND COOLED OFFICE WITH AN

INTEGRATED DESICCANT VENTILATION UNIT

A Dissertation

by

XIANGYANG GONG

Submitted to the Office of Graduate Studies of
Texas A&M University
in partial fulfillment of the requirements of the degree of

DOCTOR OF PHILOSOPHY

Approved by:

Chair of Committee,	David E. Claridge
Committee Members,	W. Dan Turner
	Warren Heffington
	Charles Culp
	David H. Archer
Head of Department	Dennis O'Neal

August 2007

Major Subject: Mechanical Engineering

ABSTRACT

Investigation of a Radiantly Heated and Cooled Office with an Integrated
Desiccant Ventilation Unit. (August 2007)
Xiangyang Gong, B.S., North China Institute of Electric Power, China;
M.S., Southern Illinois University
Chair of Advisory Committee: Dr. David E. Claridge

Radiant heating and cooling has a reputation of increasing the comfort level and reducing the energy consumption of buildings. The main advantages of radiant heating and cooling are low operational noise and reduced fan power cost. Radiant heating and cooling has been supplied in several forms, including floor heating, ceiling heating and cooling, radiant panels and façade heating and cooling. Among them, façade heating and cooling is the most recently developed system. This dissertation provides a comprehensive study of several technical issues relative to radiant heating and cooling systems that have received little attention in previous research. The following aspects are covered in this dissertation:

First, a heat transfer model of mullion radiators, one type of façade heating and cooling, is developed and verified by measured performance data. The simulation demonstrates that the heating or cooling capacity of mullion radiators is a semi-linear function of supply water temperature and is affected by the thermal conductive resistance of mullion tubes, the room air temperature, the supply water flow rate, and the outside air temperature.

Second, the impact of the positions of radiators on energy consumption and thermal comfort is studied. This dissertation compares the heating load and comfort level as measured by uniformity of operative temperature for two different layouts of radiators in the same geometric space. The air exchange rate has been identified as an important factor which affects energy saving benefits of the radiant heating systems.

Third, the infiltration and the interaction of infiltration and mechanical ventilation air to produce moisture condensation in a radiantly cooled office are examined. The infiltration of the studied office is also explored by on-site blower door measurement, by analyzing measured CO_2 concentration data, and through modeling. This investigation shows the infiltration level of the studied office to range between 0.46 and 1.03 air changes per hour (ACH).

Fourth, the integrated sensible heating and cooling system is simulated and compared with a single duct variable air volume (VAV) system. The results show that, at the current infiltration

level, the studied sensible heating and cooling system with an integrated active desiccant ventilation unit consumes 5.6% more primary energy than a single duct VAV system; it would consumes 11.4% less primary energy when the system is integrated with a presumed passive desiccant ventilation unit.

ACKNOWLEDGEMENTS

I would like to express my appreciation to Dr. David Claridge for his invaluable direction and input on this work, and for his guidance, encouragement and help throughout my graduate study. I would also like to extend my gratitude to Dr. David Archer, the project manager of this research. He spent a great deal of time and energy helping me collect data and coordinating among the team members. Without his contributions, this research would not have been completed. I would also like to acknowledge Dr. Dan Turner, Dr Charles Culp and Dr. Warren Heffington for their generous suggestions.

Special thanks should be given to Dr. Dan Turner. He brought me into the Energy Systems Laboratory so that I could work and support myself during my pursuit of this PhD.

I would also like to thank my friends, Dr. Yin, Dr. Yang, Dr. Hu, Dr. Gao, Ming, Nina, Fred, Sophie, Yun, and Chaoqin for their helpful information and input into this research.

I am grateful to my parents and my wife for their support, encouragement and patience during my six years of graduate study.

TABLE OF CONTENTS

LIST OF FIGURES

LIST OF TABLES

CHAPTER I

INTRODUCTION

1.1 Background

Rising energy prices during recent years have significantly increased the operating costs of educational buildings, which adds a substantial burden on both universities and students. In 2002, the U.S. Department of Energy initiated a research program aimed at applying advanced HVAC technology to educational buildings to investigate more comfortable, occupant-friendly and low energy consumption university building prototypes. The Intelligent Workplace (IW) at Carnegie Mellon University was selected as the test site for this research program. This program proposed to build a micro cogeneration unit as an energy supply source, and to use waste heat as well as heat from solar receivers to produce hot and chilled water (Yin 2006). The space uses radiant heating and cooling as its energy distribution system in the indoor space. Texas A&M University is taking part in this research program, and focusing its research on the radiant heating and cooling for the indoor space and the commissioning of the necessary systems.

1.2 Introduction of the Intelligent Workplace

The test site, the IW, is a small university office area which includes space for faculty, graduate student and staff offices and a meeting room. This office space is used by the Center for Building Performance and Diagnostics in the Department of Architecture at Carnegie Mellon University. The 580m^2 (6228 ft^2) space uses a radiant heating and cooling system combined with a solid desiccant ventilation system. In the north zone of the IW, "cool waves" are also used to supply partial cooling in summer. "Cool wave" is a chilled beam coupled with a slowly oscillating fan, which cools room air by forced air circulation. The "cool wave" units are recommended by the manufacturers to meet sensible load only, in order to avoid mold growth. 21 fan coil units are planned for installation in the south zone. The space uses two types of radiant panels. The first type is radiant mullions, as shown in Figure 1.1, which are installed vertically along the window frames and are an integrated part of the building façade. The mullion system is used to offset the heating and cooling load from the windows, and to increase indoor comfort levels. Another function of the mullion system is that grouped mullions can

_____

This dissertation follows the style and format of ASHRAE Transactions.

provide flexible heating and cooling set points based on the preference of the occupants. The second type is comprised of overhead radiant panels, as shown in Figure 1.2, which are used for spaces located away from the windows.

Figure 1.1 The Radiant Mullions in the IW

Figure 1.2 The Overhead Radiant Panels

These two types of radiant panels are used for cooling in summer and heating in winter. Chilled water currently is supplied by the campus loop, and hot water is supplied by a steam-to-water heat exchanger located in the basement which uses the steam from the campus loop. The IW chilled and hot water are switched in the same piping system between summer and winter, which corresponds to a two-pipe system.

1.3 Radiant Heating and Cooling System

The radiant heating and cooling systems have gradually gained popularity in Europe in the last decade and are frequently discussed in the United States. The discussions fall into two categories. One is thermal comfort and energy savings benefits from the application of the radiant heating and cooling (Brunk 1993, Busweiler 1993, Kulpmann 1993, Niu and Kooi. 1994, 1995, Behne 1995, Hodder et al. 1998, Imanari et al. 1999, Sodec 1999, Mumma 2001a, 2001b). The other is the operation and control issues of this system (Simmonds 1994, 1996, Mumma 2002). Several pilot projects have been constructed to test the concept of the radiant cooling system. A project which has been a frequent topic in publications appearing in recent years is a 3200 ft^2 educational office space in Pennsylvania State University which applied ceiling radiant cooling panels with a passive desiccant system (Shank and Mumma 2001, Jeong et al. 2003). The Intelligent Workplace is another pilot project using a radiant heating and cooling system. The distinctive characteristic of the IW radiant system is the application of mullion heating and cooling, which is one type of façade heating and cooling technology. The radiant mullions in the IW are based on a German patent entitled Integrated Façade System Gartner (1968), Patent number 1,784,864, which states that the heating device is formed by a hot water circuit which extends through cavities of the vertical or horizontal metal section of an exterior wall or window. This system is used to maximize the comfort level of spaces. Significant research has been done regarding radiant heating and cooling. However, mullion heating and cooling (façade heating and cooling) has received little attention in previous research. No detailed heat transfer models or thorough analysis have been reported in the open literature.

Radiant cooling is not well accepted in the United States. Moisture condensation is a major concern that restricts the application of radiant cooling. Theoretically, moisture condensation can be reduced or avoided by controlling indoor humidity levels. Mumma (2001c) and Niu (2002) have addressed the condensation issues in a radiantly cooled office. The indoor humidity level is determined by several factors such as indoor latent load, infiltration moisture, and moisture from

ventilation air. In the test case office, the IW, the ventilation air is provided by a solid desiccant ventilation unit. A better understanding of the interaction among these factors and the solid desiccant ventilation unit itself is necessary to ensure the safe operation of a radiant cooling system.

1.4 Desiccant Ventilation System

Some researchers (Mumma and Lee 1998, Coad 1999, Khattar and Brandemuehl 2002) in recent years have cast doubt on the capability of humidity control of all-air systems and instead have proposed the application of a dedicated outside air system (DOAS). The IW applied the DOAS concept because the radiant heating and cooling panels do not possess the ability to control humidity. The dehumidification of a radiantly heated or cooled space can be accomplished by using either desiccants (solids or liquids) or cooling coils. Gatley (2000) compared the economy of the application of these several forms of technology. He concluded that conventional cooling with recuperative reheat systems offers a better choice when the required dew point temperature is above 40˚F, and the active desiccants are generally a better choice when the dew point temperature is below 40˚F. The ventilation air of the IW was supplied by a passive desiccant unit before winter, 2005, which supplied 100% outside air for the indoor space. In the winter of 2005, the passive desiccant unit was replaced by an active desiccant ventilation unit. The new active desiccant ventilation system circulates some return air with the outside ventilation air. Detailed information and a literature review is provided in Chapters V and VII. The focus of analysis of the desiccant ventilation unit in this dissertation will be on the energy efficiency and performance of the integrated system under different infiltration conditions.

1.5 Research Motivation

The Intelligent Workplace provides a good demonstration of a low energy building that applies many emerging technologies such as façade heating and cooling, radiant ceiling panels, a DOAS system with a desiccant wheel, and powered curtains and shading. The IW AC system provides good indoor air quality for its occupants. The average energy consumption of the IW is only two-thirds of that of a similar building in the same climate zone. However, a low energy building is not just the result of applying one or more isolated technologies, but rather is a result achieved by enhanced integrated system performance. There are still some problems in the operation of the integrated AC system in the IW during the past several years, such as

insufficient cooling and condensation in summer. The motivation of this dissertation is to investigate the fundamental reasons for these problems by performing the following work. First, the radiant mullions and panels in the IW will be modeled to evaluate their performance and contributions to indoor thermal comfort; second, this research will simulate the integrated system to assess the energy efficiency and identify those problems that most affect the energy efficiency of the studied space.

1.6 Objective

Radiant heating and cooling have the potential to reduce energy consumption in buildings. They offer a prospective alternative to the currently overwhelming use of air heating systems. Although extensive research has been done on radiant heating and cooling, there are still several aspects that have not been thoroughly studied or fully understood. This dissertation aims to enhance the understanding of the heat transport physics of facade heating and cooling, the effect of infiltration on indoor moisture levels in a radiantly heated or cooled office, and the integrated system performance. The following aspects will be studied:

- Heat transfer models for mullion heating and cooling.
- Heat transfer models for overhead radiant panels.
- The impact of the position of radiators and ventilation rates on energy consumption and thermal comfort.
- Indoor humidity analysis of a radiantly cooled office integrated with a desiccant ventilation system under various infiltration conditions.
- Infiltration investigation.
- Performance analysis of the integrated sensible heating and cooling system with a desiccant ventilation unit.

1.7 Methodology

The above objectives can be accomplished by the following activities:

- Analyzing the fundamental heat transfer of mullion radiators along the flow direction and solving for mullion and window surface temperatures numerically. The simulated surface temperatures are compared with the measured data to verify the model.
- Studying the radiation, convection and conduction on each surface of a simplified radiantly heated office case to evaluate the heating load of the office with two different radiator positions, and numerically solving the mean radiant temperature distribution and

air temperature distribution to understand the impact of window radiators on indoor comfort.

▪ Studying the infiltration of IW by site measurement, and analyzing previous CO_2 measurement data.

▪ Simulating the IW by DOE2.1 to obtain hourly building loads and simulating the integrated radiant heating and cooling system by FORTRAN coding. Hourly building loads and weather data are used as an input for the integrated system model. Integrated system simulation models are run to evaluate the performance of the integrated system with a passive desiccant ventilation unit and an active desiccant ventilation unit, individually.

1.8 Description of Dissertation Chapters

This dissertation is organized in the following order. Chapter II describes the modeling of window mullion radiators and verifies the mullion model with measured data. Chapter III presents the heat transfer model of ceiling radiant panels. Chapter IV studies the impact of the different positions of the radiators on heating loads and thermal comfort based on two simplified cases. This chapter is helpful for understanding the different functions of the radiators studied in Chapters II and III. Chapter V studies the indoor humidity and condensation control in the space conditioned by a radiant heating and cooling system integrated with a desiccant ventilation unit. This chapter identifies the infiltration rate as a critical variable in controlling the condensation problem when radiant cooling is used in summer. Chapter VI investigates the possible range of the infiltration rate in the IW. Chapter VII studies the energy performance of the integrated sensible heating and cooling system with a desiccant ventilation unit. This chapter uses the infiltration study results from Chapter VI and compares the energy consumption of the integrated system with that of a single duct VAV air heating and cooling system. Chapter VIII provides the observations and conclusions resulting from this research. The literature review tied to each topic is provided in the individual chapters.

CHAPTER II

THE PERFORMANCE STUDY OF RADIANT MULLIONS

2.1 Introduction

The Intelligent Workplace (IW) uses heated mullions as its heating source in the winter. The system can also be used for cooling in the summer. The mullion heating and cooling system is based on a German patent entitled "Integrated Façade System Gartner." The advantages of this system are an enhanced comfort level and quiet operation. Many research studies have been done regarding the heat transfer model of windows (Muneer et al. 1997, Omori et al. 1997, Larsson et al. 1999, Collins et al. 2000, Collins 2004), but no publications on modeling and performance evaluation of mullion heating and cooling have been found in the open literature. Because the mullions are actually radiators and are located only centimeters from the window glazing, the heat transfer processes between the mullions and the window glazing, window frames, room surfaces and inside air are complicated. Understanding these principles is important for an accurate simulation of the IW Energy Supply System (IWESS). This chapter studies the heat transfer process of window mullion radiators. One model has been developed for the mullion heating and cooling simulation and has been verified by measured data. The simulated results match the measured data very well.

2.1.1 Mullion Heating and Cooling System

Mullion radiators and overhead panels were the only available heating devices in the IW in the past several years. Currently, only mullions are used for heating. The simplified system is shown in Figure 2.1. In winter, hot water is produced by a steam-water heat exchanger and is circulated between the mullions and heat exchanger by hot water pumps. Steam is supplied by the campus loop. In summer, chilled water is supplied by the campus loop and is circulated by the chilled water pump. The heat exchanger, hot water pumps and chilled water pump are all located in the basement. There is another 33-gpm mullion pump located on the roof of the fourth floor and underneath the IW. The mullion pump provides the additional pressure needed to overcome the head loss in the mullion system. There are 26 groups of mullions in the IW. Each group has four mullions controlled by one control valve. The mullion pump currently runs at about 24-gpm during the daytime schedule.
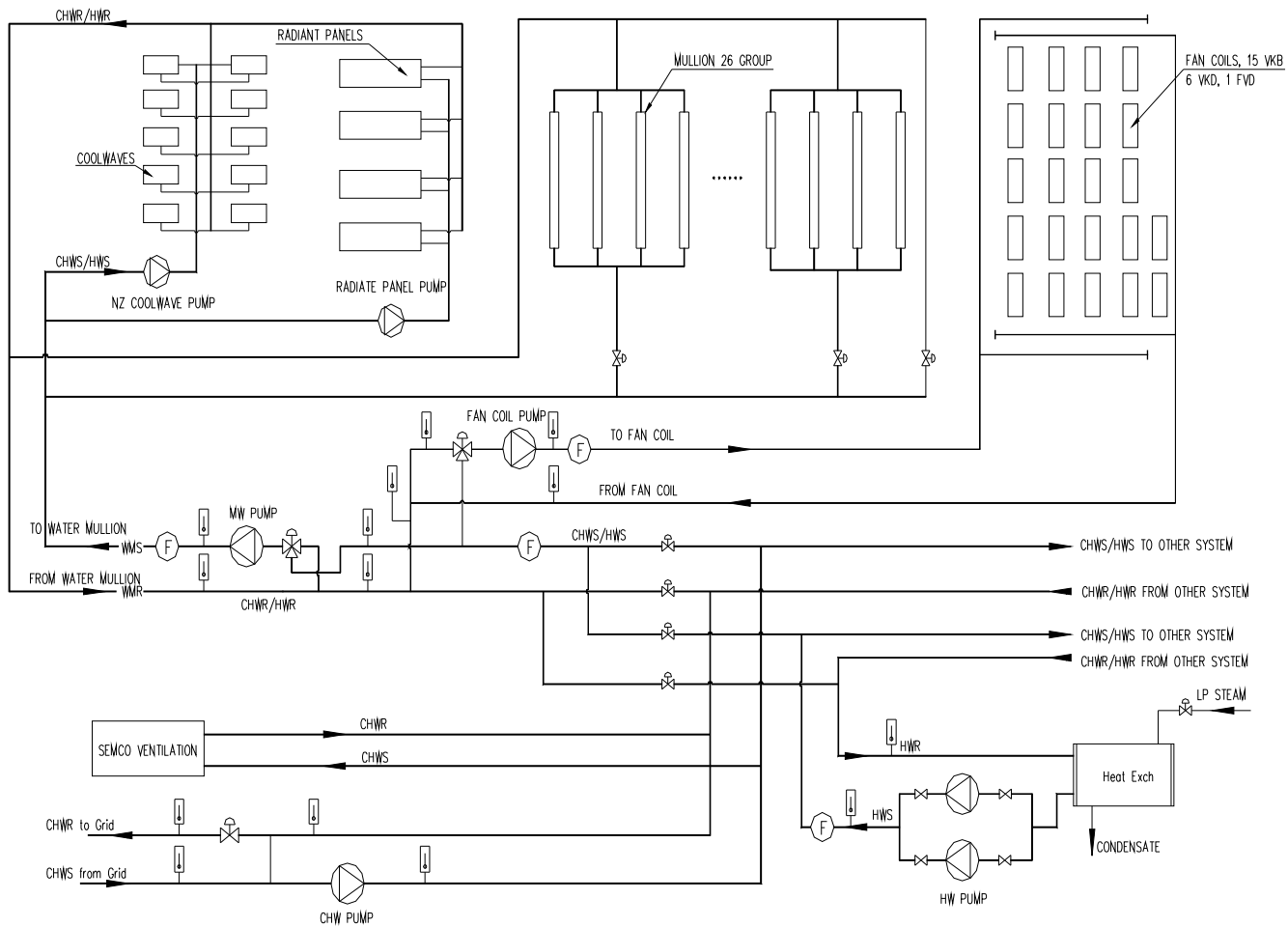
Figure 2.1 The Current HW/CHW Supply System in the IW

2.1.2 System Control

Currently, the IW mullion system is the only user of the hot water produced by the heat exchanger in the basement. The IW control system (Metasys) turns on the basement pump (HWP1 or HWP2) if the average south zone and north zone indoor temperatures $(\frac{T_{south}+T_{north}}{2})$ are below the pump set point (60°F) or if the schedule calls for it. The Metasys also turns on the fourth floor mullion water pump if the average indoor temperature $(\frac{T_{south}+T_{north}}{2})$ is below the mullion water pump set point (60°F) or if the schedule calls for it.

The hot water supply temperature set point is based on the indoor and outdoor temperatures, and on a comfort weighting factor. The hot water set point equation is:

$$T_{HW\_S} = (38-T_o)*f_{oA} + (72-\frac{T_{south}+T_{north}}{2})*f_{IA} + 120 \qquad (2.1)$$

T_{HW_S} is the hot water supply temperature set point. T_{south} and T_{north} are the indoor temperatures of the south and north zones, respectively. f_{OA} and f_{IA} are outside and inside air temperature weighting factors. The default values of these factors are both 1. The steam valve modulates to maintain the hot water set point temperature at the outlet of the heat exchanger.

The three way control valve before the mullion pump continuously modulates to maintain the mullion surface temperature set point. The mullion surface temperature set point is decided by the following equation:

$$T_{mullion-s} = \frac{\frac{T_{south}+T_{north}}{2} + T_{hws}}{2} \qquad (2.2)$$

2.2 Simulation Assumption

The mullion layout in the IW is shown in Figure 2.2. The mullions have a double tube structure, which is vertically attached to the window frame by an aluminum fin. The outer tube is aluminum. The inner tube is steel. The space between these two tubes is filled with epoxy resin. The detailed window frame structure is shown on the left side of Figure 2.3.

In order to set up an applicable model to evaluate the performance of the mullions, the space around the mullion is simplified as an enclosure represented by dotted lines in Figure 2.3. The dotted lines stand for an imaginary wall with a uniform surface temperature T_3. The imaginary wall is assumed to be infinitely long when calculating the view factors between the imaginary wall and other surfaces in the enclosure. T_3 is assumed to be equal to the mean radiant temperature (MRT) of the space (ASHRAE 2005). MRT is related to the indoor air temperature, the ratio of window area to exterior wall area, and the size of the space. ASHRAE recommends that the MRT should be equal to the room air temperature in a radiantly heated space. Gong and Claridge (2007), studied the mean radiant temperature distribution in a mixed radiant and air heated office. Their results showed that the mean radiant temperature would be 0 - 2 ^{o}F higher than the room air temperature, depending upon the location of the radiator in a 100% radiantly heated space. In the current simulation, the MRT is assumed to be 0.5 ^{o}F higher than room air temperature in the heating model.

The detail of the window frame is complicated. The window frame is an aluminum structure with a one-inch thermal gap. The U value of the frame is approximately 0.49 Btu/(ft^2-hr-$^{\circ}$F). On the left side of Figure 2.3, one of the common frame structures is shown. In this simulation, the window frame and mullion are simplified, as shown on the right side of Figure 2.3. The window frame is assumed to have a uniform thermal resistance of R=2.04 (ft^2-hr-$^{\circ}$F)/Btu.

The windows in the IW are double paned with an air space of ½ inch and a low e-coating. The typical U value of this kind of window in the heating season is 0.32 - 0.436 Btu/(ft^2-hr-$^{\circ}$F) (ASHRAE 2005). The measured data suggest that 0.43 Btu/(ft^2-hr-$^{\circ}$F) is close to the real U value in winter conditions. The corresponding R-value of the window is 2.295 (ft2-hr-$^{\circ}$F)/Btu. To evaluate the impact of the mullion radiators on heat transfer at the window surface, this thermal resistance has been decomposed into three parts: inside surface resistance (around 0.68 (ft^2-hr-$^{\circ}$F) /Btu), conductive thermal resistance (1.365 (ft^2-hr-$^{\circ}$F)/Btu), and outside surface resistance (around 0.25 (ft^2-hr-$^{\circ}$F)/Btu). The surface resistance varies with the surface temperature and radiant heat exchanges with other surfaces. Therefore, the inside and outside surface resistances are evaluated based on the operation and weather conditions instead of using a constant value.

The mullions have a double tube structure. The inner tube is steel and the outer tube is aluminum. Epoxy resin fills the gap between the inner tube and the outer tube. The total thermal

resistance of the double tube is estimated to be 0.03 - 0.08 (ft^2-hr-$^\circ$F)/Btu (U value of 12.5 - 33 Btu/(ft^2-hr-$^\circ$F)). The calibrated simulation has shown that the thermal resistance of the walls of the double tubes is close to 0.0406 (ft^2-hr-$^\circ$F)/Btu. The hot water flowing inside the mullions is assumed to be a fully developed flow and the entrance effects are ignored. The hot water is assumed to be evenly distributed in all the mullions in the IW.
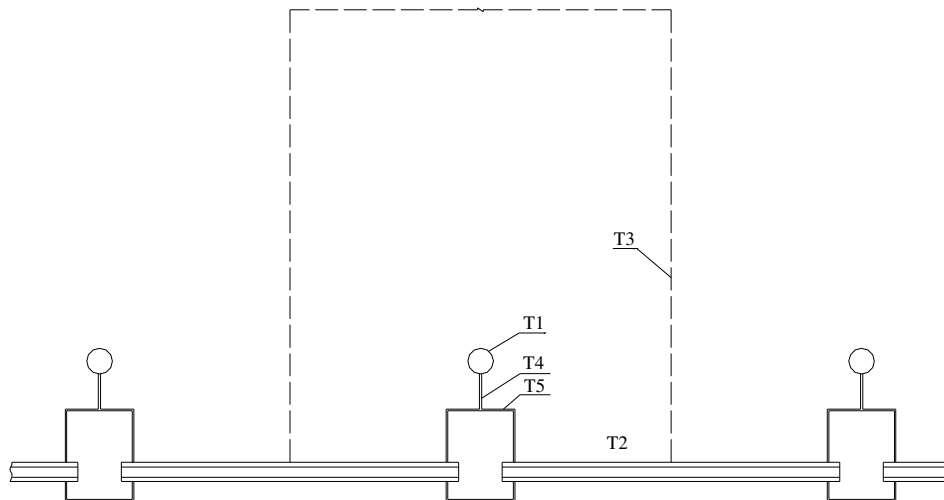
Figure 2.2 Window Mullion, Frame, and Glass (not to scale)
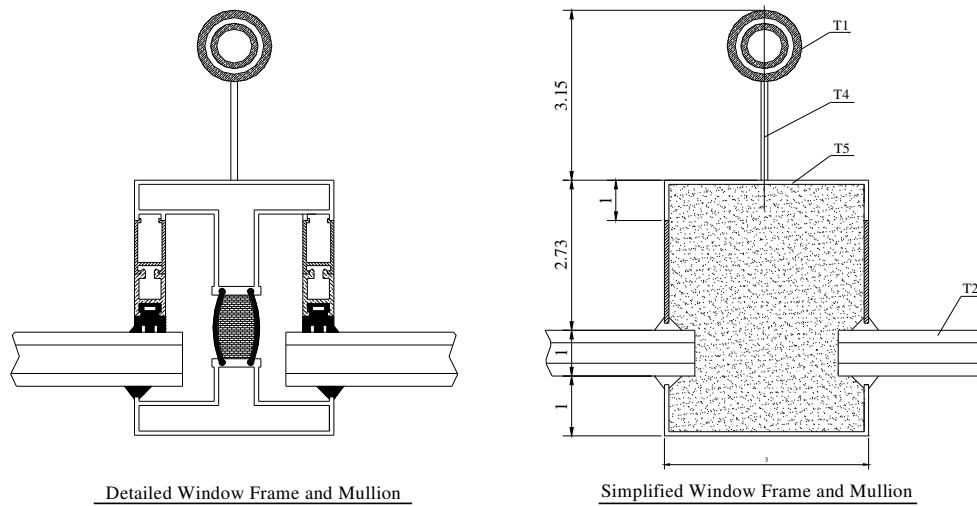
Figure 2.3 Detailed Window Frame Structure and Simplified Calculation Model

The major dimensions and parameters used in the mullion models are:

Window frame U value:	0.49 Btu/(ft²-hr-°F)
Wall overall U value:	0.049 Btu/ (ft²-hr-°F)
Mullion outer tube:	OD=1.315 inches, ID=1.049 inches
Mullion inner tube:	OD=0.84 inches, ID=0.6296 inches
Mullion fin length:	1.8363 inches
Window frame width:	3 inches
Window frame shoulder height:	3 inches above the glass (indoor side)
Window height:	7 feet 5 inches
Window width:	3 feet 11 inches
Hot/cold supply/return pipe diameter:	1.5 inches
Insulation thickness of pipe:	0.5 inches

2.3 Heat Transfer Models for Mullion Heating and Cooling System[1]

As show in Figure 2.2, five surface temperatures are assumed to be in the enclosure: tube surface T_1, window glass surface T_2, imaginary wall surface T_3, window frame surface T_4 and tube fin T_5. The imaginary wall surface T_3 is assumed to be constant. At steady state, each surface exchanges radiant heat with the other surfaces and convectively exchanges heat with room air. The window glass and frame also lose heat to the outside environment by conduction. The heat is supplied to the enclosure by hot water flowing inside the mullion tube.

There are two basic heat transfer models in the above control enclosure. The first model is the surface temperature model, which is used to solve for the tube surface temperature T_1 and the window glass surface temperature T_2. The second model is the mullion "T" shape fin model, which considers the mullion fin and window frame to be one integrated part. This model is used to solve for fin surface temperature, window frame temperature, and conduction heat loss from the mullion surface to the fin and window frame. These two models are coupled together.

---

[1] The system is described when the heating process is engaged. It also applies to cooling with appropriate changes in terminology and flow direction, unless otherwise stated.

2.3.1 Surface Temperature Model

The objective of the first model is to determine the convection and radiation heat transfer coefficients in order to solve for the surface temperature. The convection heat transfer coefficient is determined by the temperature difference between the wall surface and the room air. The radiation heat transfer coefficient is decided by the average temperature level of the two corresponding surfaces, as shown in the following equations. The units of temperature and heat transfer coefficients are °R (which is used for radiant heat transfer coefficient calculation) and Btu/ (ft^2-hr-°F). Please refer to the nomenclature for symbol definitions.

$$h_c = 0.26(T_s - T_a)^{0.32} \tag{2.3}$$

$$h_{ri} = 4\varepsilon\sigma T_{mi}^3 \tag{2.4}$$

$$T_{mi} = \frac{T_i + T_s}{2} \tag{2.5}$$

In the equations above, h_c is the convection heat transfer coefficient and h_{ri} is the radiant heat transfer coefficient. T_s is the surface temperature. T_{mi} is the average temperature of surfaces s and i. If all surface temperatures are assumed to be uniform, the energy balance equation for the window glass can be written as:

$$\frac{T_o - T_2}{R_{win}} + h_{c-win}(T_a - T_2) + \sum_i F_{win-i}\varepsilon\sigma(T_i^4 - T_2^4) = 0 \tag{2.6}$$

F_{win-i} is the view factor from the window glass to the enclosure surface i. T_2 is the window glass inner surface temperature. The energy balance equation for the tube surface can be written as:

$$\dot{q}_s^{''} = h_{c-m}(T_1 - T_a) + \sum_i F_{1-i}h_{ri}(T_1 - T_i) + \dot{q}_{fin}^{''} \tag{2.7}$$

where $\dot{q}_{fin}^{''}$ is the conduction heat flux at the fin base. $\dot{q}_s^{''}$ is the heat supply from hot water, which can be determined from Equation (2.8).

$$\dot{q}_s^{''} = h_{in}(T_{ins} - T_b) \tag{2.8}$$

T_{ins} is the inside surface temperature of the inner tube, T_b is the bulk temperature of the hot water, and h_{in} is the convection heat transfer coefficient at the inner surface of the tube. For one

differential length, dL, in Figure 2.4, $\dot{q}_s^{''}$ also equals the enthalpy change of the fluid in the differential length dL as shown in Equation (2.9).

$$h_{in}(T_{ins} - T_b) = \dot{m} * C_p * \frac{dT_b}{dL} \qquad (2.9)$$

h_{in} can be calculated by Equation (2.10). The Nusselt number can be determined using Equations (2.11) and (2.12) for the turbulent flow and the laminar flow, respectively.

$$h_{in} = \frac{NU * D_{in}}{K} \qquad (2.10)$$

$$NU_D = \frac{\frac{f}{8}(\text{Re}_D - 1000) * \text{Pr}}{1 + 12.7\left(\frac{f}{8}\right)^{\frac{1}{2}}\left(\text{Pr}^{\frac{2}{3}} - 1\right)} \quad \text{(for turbulent flow)} \qquad (2.11)$$

$$NU = 4.364 \quad \text{(for laminar flow)} \qquad (2.12)$$

$$\text{Re} = \frac{VD}{\upsilon} \qquad (2.13)$$
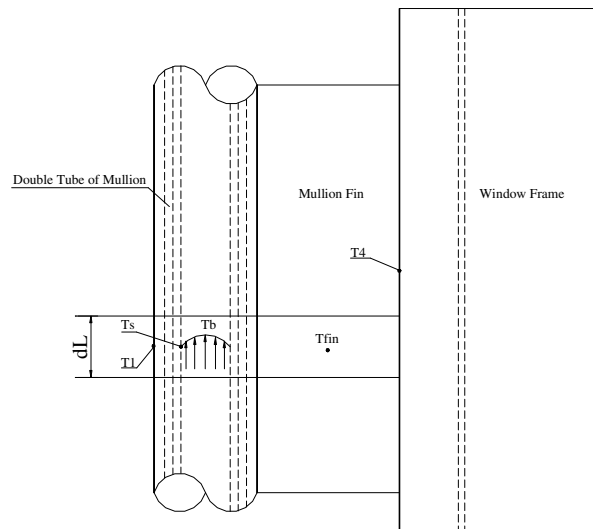
Figure 2.4 Window Mullion

Assuming the conductive thermal resistance from the inside surface of the inner tube to the outside surface of the outer tube is R_t, the heat flux from the fluid to the inside surface of the inner tube will equal the heat flux from the inside surface to the outside surface of the mullion tube, which can be expressed by the equation:

$$\dot{q}_s^{"} = \frac{T_{ins} - T_1}{R_t} = h_{in}(T_{ins} - T_b) \tag{2.14}$$

The inner surface temperature T_{ins} can be solved as:

$$T_{ins} = \frac{T_1 - R_t * h_{in} * T_b}{1 - R_t h_{in}} \tag{2.15}$$

While $\dot{q}_s^{"}$ can be expressed as:

$$\dot{q}_s^{"} = \frac{h_{in}(T_b - T_1)}{1 - R_t * h_{in}} \tag{2.16}$$

If the differential length dL is small enough (less than 1 inch), the bulk fluid temperature, T_b, can be seen as equal to the differential inlet temperature of the fluid. In a differential calculation, this T_b can be assumed to be known. Substituting Equation (2.16) into Equation (2.7), we obtain the equation

$$\frac{h_{in}(T_b - T_1)}{1 - R_t * h_{in}} = h_{c-m}(T_1 - T_a) + \sum_i F_{1-i} h_{ri}(T_1 - T_i) + \dot{q}_{fin}^{"} \tag{2.17}$$

In the enclosure of Figure 2.2, T_3 is known. T_4 and T_5 are considered to be surface temperatures of the T shaped fin, and can be solved by the T shaped fin model. $\dot{q}_{fin}^{"}$ can also be obtained from the T shaped fin model. By guessing the heat transfer coefficients, the unknowns in the enclosures would be the mullion tube surface temperature T_1 and the window glass temperature T_2. By combining Equation (2.6) and Equation (2.17) as a two-equation matrix, T_1 and T_2 can be solved using a small differential length. Once the surface temperature is solved, the heat transfer coefficients are then recalculated and submitted to the first and second models to again solve for surface temperature. The process is iterated until the heat transfer coefficient converges; then the heat flux, $\dot{q}_s^{"}$, is calculated for the differential length. Once $\dot{q}_s^{"}$ of the differential length is obtained, the fluid outlet temperature can also be found. The fluid outlet

temperature of one differential length will be used as the inlet temperature of the next differential length. By dividing the mullion double tubes along the flow direction into a certain number of differential lengths, the temperatures of the mullion tube surface and the window glass surface can be solved numerically. The heat input of one mullion can be found by summing $\dot{q}_s^{"} * dA$ of all the differential segments along the flow direction.

2.3.2 T Shaped Fin Model

In the first model, the ability to determine the mullion surface temperature T_1 and window glass temperature T_2 depends upon the ability to determine fin surface temperature T_5, frame temperature T_4 and the heat flux at fin base, $\dot{q}_{fin}^{"}$. These temperatures can be solved using the fin model. Because the fin and window frame are one aluminum part, they are treated as a T shaped fin. The two shoulders of the window frame can be seen as the extension of the "horizontal bar" of the T shaped fin.

The T shaped fin can be simulated as two parts. The first part is the fin of L1 (the vertical part) in Figure 2.5. The second part is the window frame surface (the horizontal part) in Figure 2.5. Assuming that the overall heat transfer coefficient on the surface of part 1 is U_{in1} and applying the energy balance on a differential length, dy, of the part, the following differential equation can be obtained:

$$\frac{d^2T}{dy^2} = \frac{2 * U_{in1} * (T - T_a)}{k * thk} \tag{2.18}$$

Using a differential equation to express the heat transfer model of the real window frame, as shown in Figure 2.3, is almost impossible. However, if the overall heat transfer coefficient from the inside surface of the window frame to the outside air is assumed to be U_{out}, the window frame surface can be simplified as a fin with an inside overall heat transfer coefficient of U_{in2}, and an outside overall heat transfer coefficient of U_{out}. By applying the energy balance for a differential length of the window frame, the differential equation can be obtained as:

$$\frac{d^2T}{dx^2} = \frac{U_{in2} + U_{out}}{k * thk} T - \frac{U_{in2} * T_a + U_{out} * T_o}{k * thk} \tag{2.19}$$
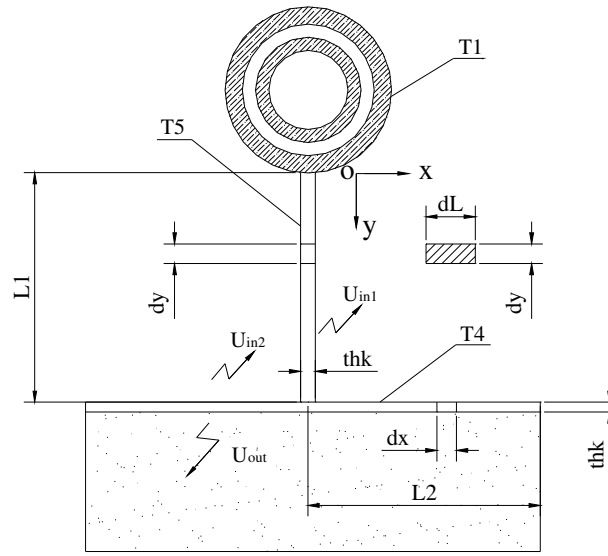
Figure 2.5 Simplified Calculation Diagram for Window Mullion

In order to simplify the calculation, the thicknesses of parts 1 and 2 are assumed to be the same. The tip condition of part 2 is assumed to be adiabatic. The boundary conditions for Equations (2.18) and (2.19) are:

$$Y = 0, \quad T = T_1 \tag{2.20}$$

$$Y = L1, \quad T_{Y=L1} = T_{X=0} \tag{2.21}$$

$$\left.\frac{\partial T}{\partial Y}\right|_{Y=L1} = 2 * \left.\frac{\partial T}{\partial X}\right| \tag{2.22}$$

$$\left.\frac{\partial T}{\partial Y}\right|_{Y=L2} = 0 \tag{2.23}$$

The general solution of governing Equation (2.18) is:

$$\theta_1 = C_1 e^{ay} + C_2 e^{-ay} \tag{2.24}$$

$$\theta_1 = T - T_a \tag{2.25}$$

$$a = \left(\frac{2 * U_{in1}}{k * thk}\right)^{0.5} \tag{2.26}$$

The general solution of governing Equation (2.19) is:

$$\theta_2 = C_3 e^{s_1 x} + C_4 e^{s_1 x} \tag{2.27}$$

$$\theta_2 = T - T_{a1} \tag{2.28}$$

$$T_{a1} = \frac{S_2^{\,2}}{S_1^{\,2}} \tag{2.29}$$

$$S_1 = \left(\frac{U_{in2} + U_{out}}{k * thk} \right)^{0.5} \tag{2.30}$$

$$S_2 = \left(\frac{U_{in2} * T_a + U_{out} * T_o}{k * thk} \right)^{0.5} \tag{2.31}$$

Applying boundary conditions (2.20) and (2.21) to Equations (2.24) and (2.27), the constants C_1, C_2, C_3, C_4 can be solved as shown in Equations (2.32) - (2.35). The temperature distribution along the T shaped fin can be calculated with Equations (2.24) and (2.27) after solving for C_1, C_2, C_3, and C_4 as:

$$C_1 = \frac{(2S_2 * T_{a1} - 2S_2 * T_a + \theta_1 * a * e^{-a*L1} - 2\theta_1 * S_2 * e^{-a*L1})e^{S_1 * L2} + (2S_1 * T_a - 2S_1 * T_{a1} + \theta_1 * a * e^{-a*L1} + 2\theta_1 * S_1 * e^{-a*L1})e^{-S_1 * L2}}{(a * e^{S_1 * L2} + a * e^{-S_1 * L2} - 2S_1 * e^{-S_1 * L2} + 2S_2 * e^{S_1 * L2})e^{a*L1} + (a * e^{S_1 * L2} + a * e^{-S_1 * L2} + 2S_1 * e^{-S_1 * L2} - 2S_2 * e^{S_1 * L2})e^{-a*L1}} \tag{2.32}$$

$$C_2 = \frac{(-2S_2 * T_{a1} + 2S_2 * T_a + \theta_1 * a * e^{a*L1} + 2\theta_1 * S_2 * e^{a*L1})e^{S_1 * L2} + (-2S_1 * T_a + 2S_1 * T_{a1} + \theta_1 * a * e^{a*L1} - 2\theta_1 * S_1 * e^{a*L1})e^{-S_1 * L2}}{(a * e^{S_1 * L2} + a * e^{-S_1 * L2} - 2S_1 * e^{-S_1 * L2} + 2S_2 * e^{S_1 * L2})e^{a*L1} + (a * e^{S_1 * L2} + a * e^{-S_1 * L2} + 2S_1 * e^{-S_1 * L2} - 2S_2 * e^{S_1 * L2})e^{-a*L1}} \tag{2.33}$$

$$C_3 = \frac{(2\theta_1 + T_a * e^{a*L1} + T_a * e^{-a*L1} - T_{a1} * e^{a*L1} - T_{a1} * e^{-a*L1}) * a * e^{-S_1 * L2}}{(a * e^{S_1 * L2} + a * e^{-S_1 * L2} - 2S_1 * e^{-S_1 * L2} + 2S_2 * e^{S_1 * L2})e^{a*L1} + (a * e^{S_1 * L2} + a * e^{-S_1 * L2} + 2S_1 * e^{-S_1 * L2} - 2S_2 * e^{S_1 * L2})e^{-a*L1}} \tag{2.34}$$

$$C_4 = \frac{(2\theta_1 + T_a * e^{a*L1} + T_a * e^{-a*L1} - T_{a1} * e^{a*L1} - T_{a1} * e^{-a*L1}) * a * e^{S_1 * L2}}{(a * e^{S_1 * L2} + a * e^{-S_1 * L2} - 2S_1 * e^{-S_1 * L2} + 2S_2 * e^{S_1 * L2})e^{a*L1} + (a * e^{S_1 * L2} + a * e^{-S_1 * L2} + 2S_1 * e^{-S_1 * L2} - 2S_2 * e^{S_1 * L2})e^{-a*L1}} \tag{2.35}$$

In the equations above, $\theta_1 = T_1 - T_a$. T_1 is the mullion tube surface temperature. Once the temperature distribution along the fin is known, the conduction heat flux at the fin base, $\dot{q}_{fin}$, can be solved by Equation (2.36). Correspondingly, the average temperature of the fin (T_5) and the window frame (T_4) can be found by using integration methods. By substituting $\dot{q}_{fin}$, T_4, and T_5 into the surface temperature model, the first model can be solved.

$$\dot{q}_{fin} = (thk * dL) \frac{\partial T}{\partial Y} \bigg|_{Y=0} \tag{2.36}$$

In the fin model, the overall heat transfer coefficients U_{in1} and U_{in2} are the summation of the convection heat transfer coefficient and the weighted radiation heat transfer coefficient. The overall heat transfer coefficient can be found by the equation:

$$U = h_c + \sum_i f_i * h_{ri} \tag{2.37}$$

where h_c is the convection heat transfer coefficient at the studied surface, f_i is the view factor from the studied surface to another surface, $i,$ in the enclosure, and hr_i is the radiation heat transfer coefficient from the studied surface to another surface, $i,$ in the enclosure. h_c and hr_i are decided by the surface temperature differences, as shown in Equations (2.3) and (2.4). The radiant temperature is assumed to be the same as the air temperature in order to simplify the fin model calculation.

2.4 Comparison of Simulated Results with Measured Data

The heat transfer models introduced in the previous section combined numerical analysis with theoretical analysis methods. A program has been written based on these models. The program uses hot water supply temperature, flow rate, indoor zone temperature and outside air temperature as inputs to calculate mullion system hot water return temperature, mullion surface temperature distribution (tube surface and fin surface), window frame temperature distribution, window surface temperature distribution, and heat input by the mullion system. The program calculates the average mullion and window surface temperatures (T_1, T_2, T_4 and T_5 in Figure 2.2).

The mullion system operation data are recorded by the IW operation engineer. The available measured data were collected from February 24, 2006, to March 4, 2006. The data were trended every 30 minutes by the IW engineer. During the 10 day measurement period, the system was shut down either by the control system or manually for certain periods of time. When the system is down, a small amount of hot water runs through the system due to mullion valve leakage. The measured data, during the system shut downs show a large variation in mullion and window surface temperatures for different window orientations. The reason appears to be that hot water is unevenly distributed among the parallel mullions when the flow rate is very small. This part of the measured data is not used in the analysis because the data do not reflect the normal operating conditions. The measured mullion temperatures at the north window are used for comparison

with the simulated data, because sensors in this window receive fewer disturbances due to occupant activities and radiation than in other windows.

The measured data are compared with simulated results. The simulated hot water return temperature T_{ret}, mullion surface temperature T_{mu}, and window surface temperature T_{win}, have been found to be sensitive to several input parameters such as hot water supply temperature T_{hws}, conductive thermal resistance of double tube R_t, window frame heat transfer coefficient U_{out}, and window glass conductive thermal resistance R_{win}. These parameters are adjusted using regression to obtain the best results. At $R_t = 0.0406\dfrac{ft^2 - h - {}^oF}{Btu}$, $U_{out} = 0.49\dfrac{ft^2 - h - {}^oF}{Btu}$ and $R_{win} = 1.365\dfrac{ft^2 - h - {}^oF}{Btu}$, the simulated results match the measured results very well. The sensitivity study is described in the discussion section of this chapter. The final simulated results are shown below.

2.4.1 Hot Water Return Temperature

Figures 2.6 and 2.7 show the comparison of the simulated results with the measured results as a time series and as a function of supply water temperature, respectively. The simulated results are quite consistent with the measured results. Figure 2.7 indicates that the return water temperature is close to a linear function of the supply water temperature. This indicates that the mullion return water temperature can be estimated based on the supply water temperature, when the indoor air temperature remains relatively constant at 72°F.
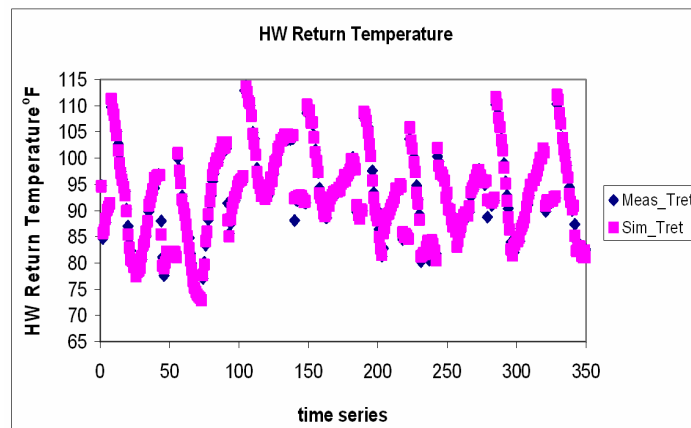
Figure 2.6 Measured HW Return Temperature vs. Simulated HW Return Temperature
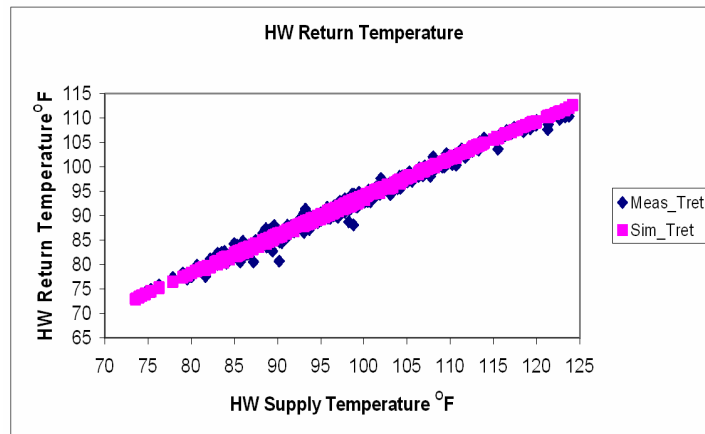
Figure 2.7 Measured and Simulated HW Return Temperatures as Functions of HW Supply Temperature
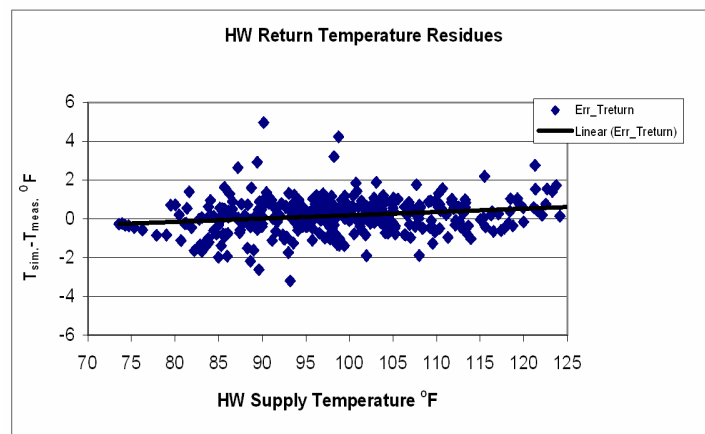
Figure 2.8 Residuals of Hot Water Return Temperature as a Function of Hot Water Supply Temperature

Figures 2.8 and 2.9 show the residuals of the hot water return temperature. The residuals are defined as the simulated results minus the measured results. The root mean square error (sample deviation) of the simulation residuals is 0.9°F. Figure 2.8 shows that the residual trend line has a non-zero slope when the residuals are plotted as a function of the supply water temperature. The non-zero slope may point to a factor or parameter other than the supply water temperature, which also affects the simulation errors. Figure 2.9 shows that the residual trend line slope is close to zero when they are plotted as a function of the difference between supply temperature and zone

temperature. The flat slope indicates that the return water temperature may be more accurately modeled as a function of the difference between supply temperature and zone temperature. Figure 2.9 considers the effects of the zone temperature (average temperature of the south zone and the north zone) on the simulation results.
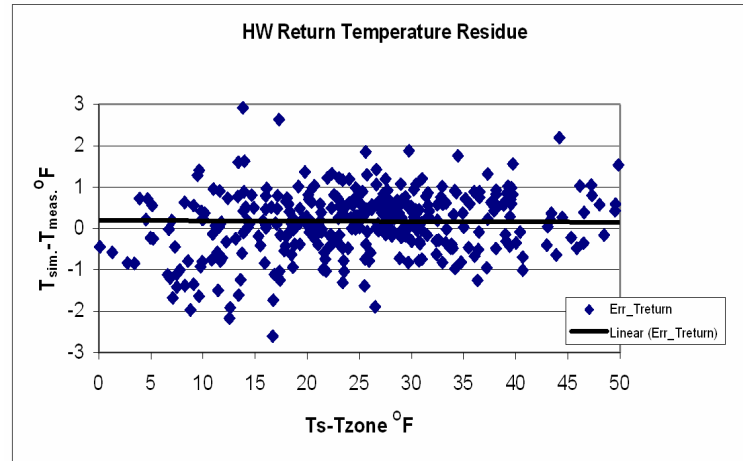
Figure 2.9 Residuals of Hot Water Return Temperature as a Function of the Difference Between Supply Temperature and Zone Temperature

2.4.2 Mullion Surface Temperature

The program calculates the temperature distribution along the mullion tube, fin and window frame. The output surface temperatures are the average values of the temperatures of these surfaces. All the mullion temperature sensors in the IW are installed on the fin surface at a height of 38cm (15 inches) above the floor. Therefore, the fin surface temperatures at the sensor points are used as the mullion surface temperatures in this chapter in order to compare those values with the measured mullion temperature at the same point.

The measured and simulated mullion surface temperatures are plotted in Figures 2.10 and 2.11, as a function of the hot water supply temperature and the mullion temperature set points. The simulated temperatures match the measured temperature very well except for some outlier points. Figure 2.10 shows that mullion surface temperature is close to a linear function of the hot water supply temperature. The mullion surface temperatures are controlled by the set points of

the average zone temperature and the supply water temperature. Figure 2.11 shows that the mullion surface temperatures are also a linear function of the mullion temperature set points.
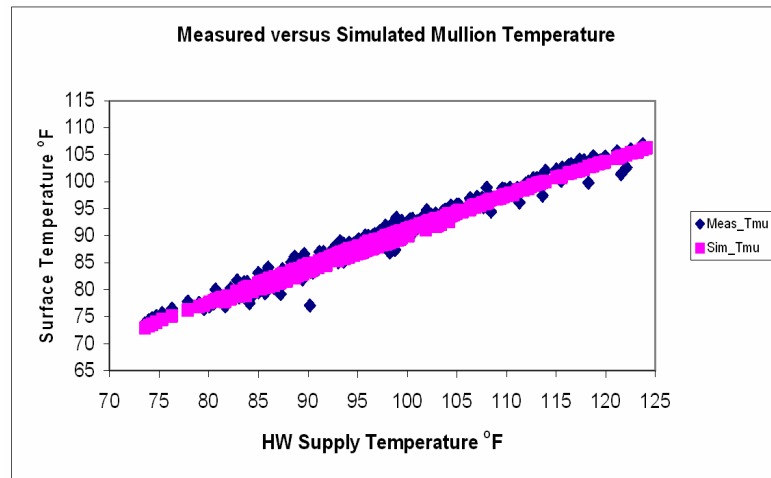
Figure 2.10 Measured vs. Simulated Mullion Surface Temperature as a Function of Hot Water Supply Temperature
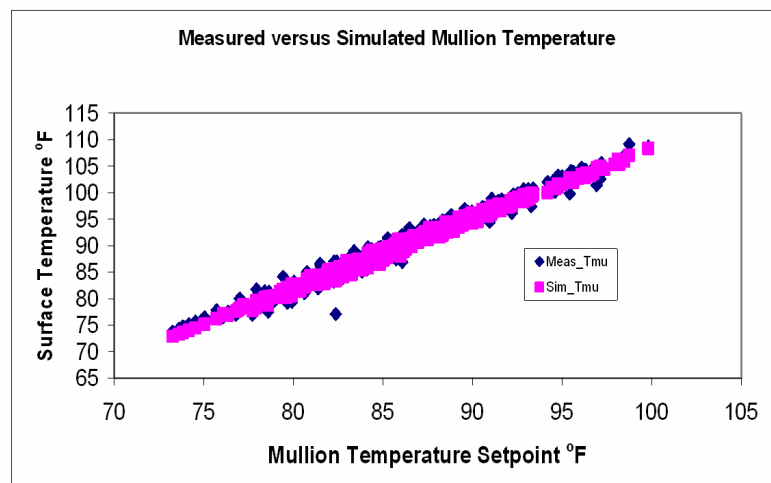
Figure 2.11 Measured vs. Simulated Mullion Surface Temperature as a Function of Mullion Temperature Set Point
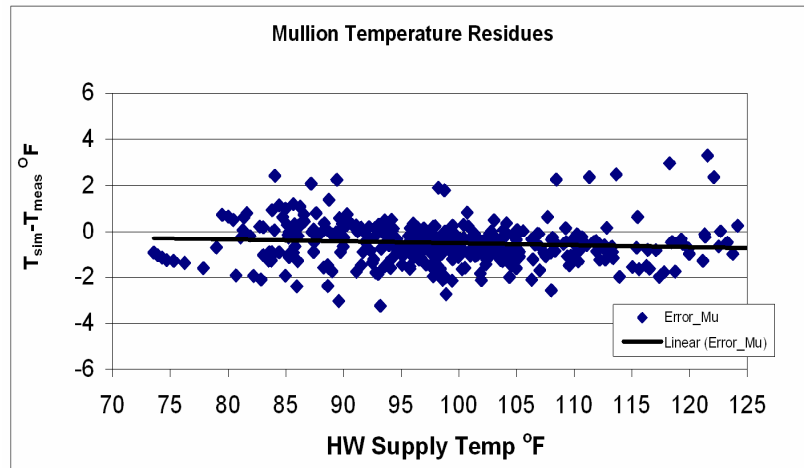
Figure 2.12 Residuals of Mullion Surface Temperature as a Function of Mullion Temperature Set Point
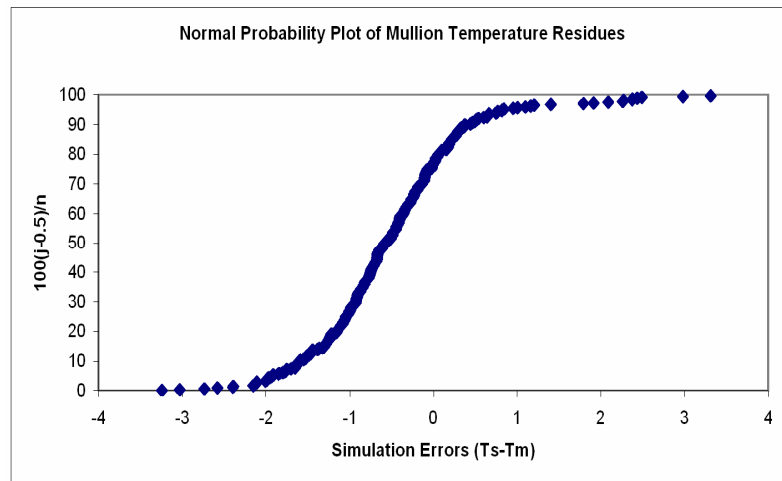
Figure 2.13 Normal Probability Plot of Mullion Temperature Residuals
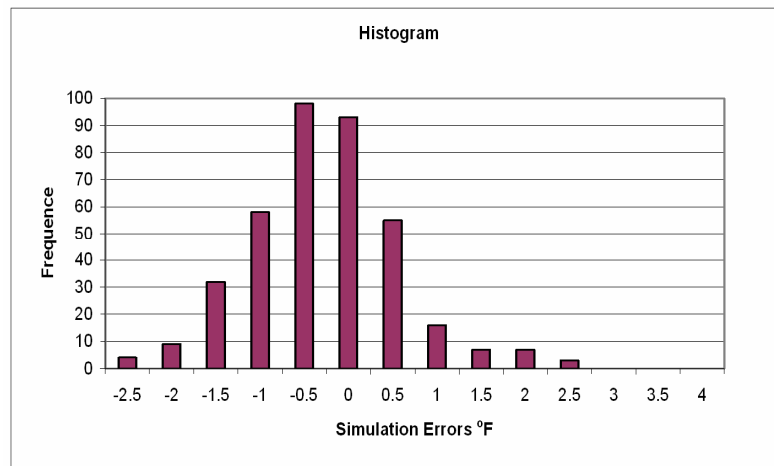
Figure 2.14 Histogram of Mullion Temperature Residuals

The residuals plot in Figure 2.12 shows that the simulation residuals are nearly evenly distributed along the x-axis. The small non-zero slope may be caused by a sensor error or errors in estimation of the thermal conductivity of the mullion tube and fin. The root mean square error of the mullion surface temperature (sample deviation) is 0.98°F. The probability plot and histogram of the mullion temperature residuals are shown in Figures 2.13 and 2.14. Figure 2.13 indicates that the residuals are normally distributed with two small tails. The histogram in Figure 2.14 also confirms that the simulation residuals are close to normally distributed.
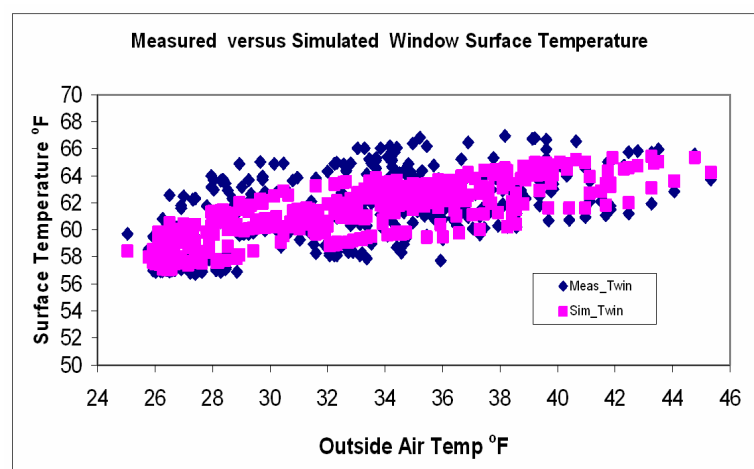
Figure 2.15 Measured vs. Simulated Window Surface Temperature as a Function of the Outside Air Temperature

2.4.3 Window Surface Temperature

The simulated and measured window surface temperatures are plotted in Figure 2.15 as functions of the outside air temperature. Both measured and simulated data are scattered, which means that other factors also have an impact on the window glass temperature. The root mean square error of the window temperature simulation is 1.15°F. The window glass temperature sensor on the north window is located 8 inches from the bottom edge of the window and 3 inches from the edge of the window frame. The type of surface sensor is a T type thermal couple embedded in a copper block. The relative error of the thermal couple itself is approximately 0.75% above 32°F, and 1.5% below 32°F (www.omega.com). The maximum error should be less than 0.2°F in winter and less than 0.5°F in summer. The structure of the sensor eliminates the partial influence of radiation, and the reading is close to the average window surface temperature. The window surface temperature in the simulation output is the average temperature of the window. Figure 2.16 shows the residuals of window inside surface temperature simulation. The residuals are nearly evenly distributed along the x-axis. The error of the thermal couple sensor or the estimation of the thermal conductivity of the window glass may cause the small non-zero slope.
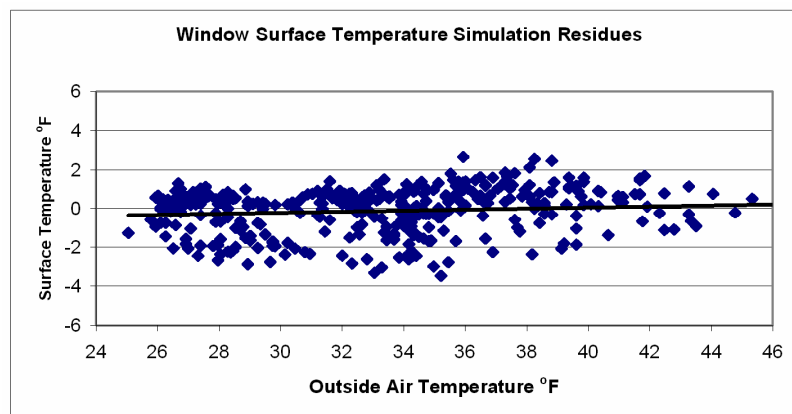
Figure 2.16 Residuals of the Window Inside Surface Temperature

2.4.4 Mullion Fin and Window Frame Temperature

Figure 2.17 shows the simulated average temperature of the mullion fin and the window frame. The figure indicates that the fin surface temperatures are close to the window frame

temperatures when the hot water temperature is low. When the water temperature is high, the fin temperature is slightly higher than the window frame temperature. At a hot water supply temperature of 125°F, the difference between the average fin temperature and the average frame is about 2°F. The simulation results illustrate the benefits of mullion heat. The temperature of the aluminum window frame is increased. The increased window frame surface temperature enhances the comfort level of the indoor space.
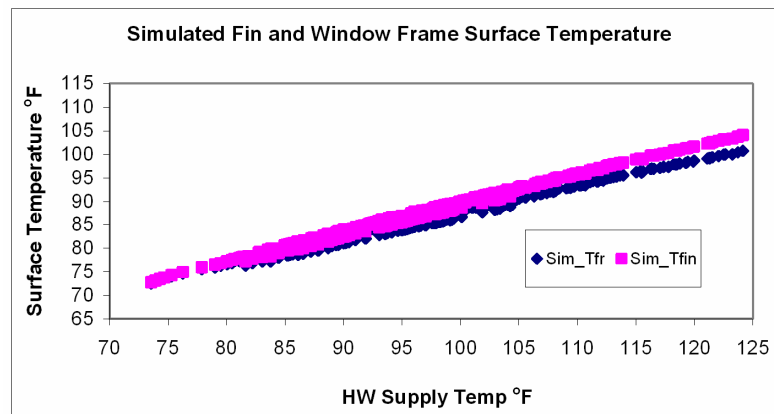
Figure 2.17 Simulated Fin and Window Frame Temperatures

2.5. Heating Capacity of Mullion Radiators

From the above comparison, it was found that the hot water return temperature, mullion surface temperature and window frame temperature are all quasi-linear functions of the supply water temperature. Therefore, the above three parameters can be approximately predicted by knowing the hot water supply temperature.

Once the hot water return temperature is known, the heat input by the mullion system can be easily calculated by the following equation. The performance table of one mullion at the heating condition state is shown in Appendix 1.

$$\dot{q} = \dot{m} * C_p * (T_{hws} - T_{ret}) \tag{2.38}$$

2.6. Cooling Capacity of Mullion Radiators

The above model can also be used for cooling calculations. In the cooling model, the room radiation temperature may be the same as the room air temperature (ASHRAE 2005) or higher

than the room air temperature depending upon the geometry and window size of the thermal envelope. Kilkis (1995) studied the average mean radiant temperature under radiant cooling conditions. The average uncontrolled surface temperature, AUST, was used as an indicator of the mean radiant temperature in his study. He developed the following correlation:

$$AUST = T_a - c * \frac{7}{T_o - 45} \qquad T_o < 45°C \qquad (2.39)$$

In the equation (2.39), the temperature is in °C. The constant c is 0.5 for a room without outdoor exposure. It is 1 for a room with one side exposed to the outdoors and a fenestration less than 5% of the total indoor surfaces. It is 2 for a room with one side exposed to the outdoors and a fenestration of more than 5% of the total indoor surfaces. If the room has two or more outdoor exposed sides, c is 3. Based on this equation, the AUST (MRT) will be larger than the zone air temperature, T_a, in Pittsburgh, PA. The summer average temperature in Pittsburgh, PA is around 68.6°F. To simplify the simulation, the MRT value based on equation (2.39) is 0.85°F higher than the room air temperature. This corresponds to a MRT of 72.85°F when the room air is 72 °F in the cooling season.

Figure 2.18 shows the performance of a window mullion when cooling, assuming the outside air temperature is 68.6°F and the room air temperature is 72°F. The chilled water return temperature, T_{ret}, the tube surface temperature, T_{tube}, and the window frame temperature, T_{fr}, are all linear functions of the chilled water supply temperature. Once the return temperature is solved, the cooling capacity of the mullion system can be found by Equation (2.38).

The dew point of the indoor space is approximately 61°F at 50% RH with an air temperature of 72°F. Figure 2.18 indicates that the cold water supply temperature can be no lower than 57 °F, in order to maintain a mullion tube surface average temperature that is higher than 61°F.

Figure 2.19 shows that the total heat transfer coefficient under natural convection conditions is 1.48-1.6 Btu/(ft^2-hr-$°F$) under cooling conditions. The performance table of one mullion under the cooling conditions is shown in Appendix 2.
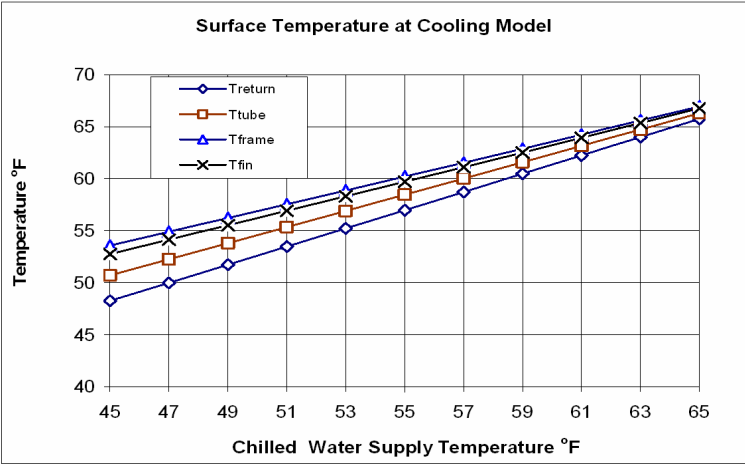
Figure 2.18 Simulated Mullion Temperatures When Cooling
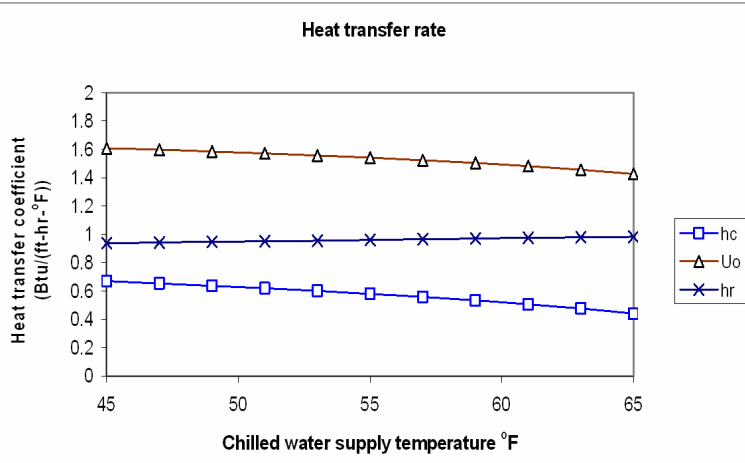
Figure 2.19 Heat Transfer Coefficients for the Cooling Model

2.7. Discussion

Typical winter and summer conditions assumed for the discussion in this section are a zone temperature of 72°F, with a winter outside air temperature of 38°F and a summer value of 68.6°F.

2.7.1 Window Surface Temperature

As discussed in the model section, the window surface temperature is assumed to be uniform over one differential length when the radiation heat transfer between the mullion surface and the window surface is calculated. However, the window surface temperature changes from the window frame to the center of the window glass. During heating, the closer to the window frame, the higher the glass temperature. Differentiating the view factor from the window glass to the mullion at each numerical length, as discussed in the modeling section, allows the temperature distribution along the horizontal direction to be found by an energy balance analysis. Figure 2.20 shows the temperature profiles of the window glass at four different hot water supply temperatures.
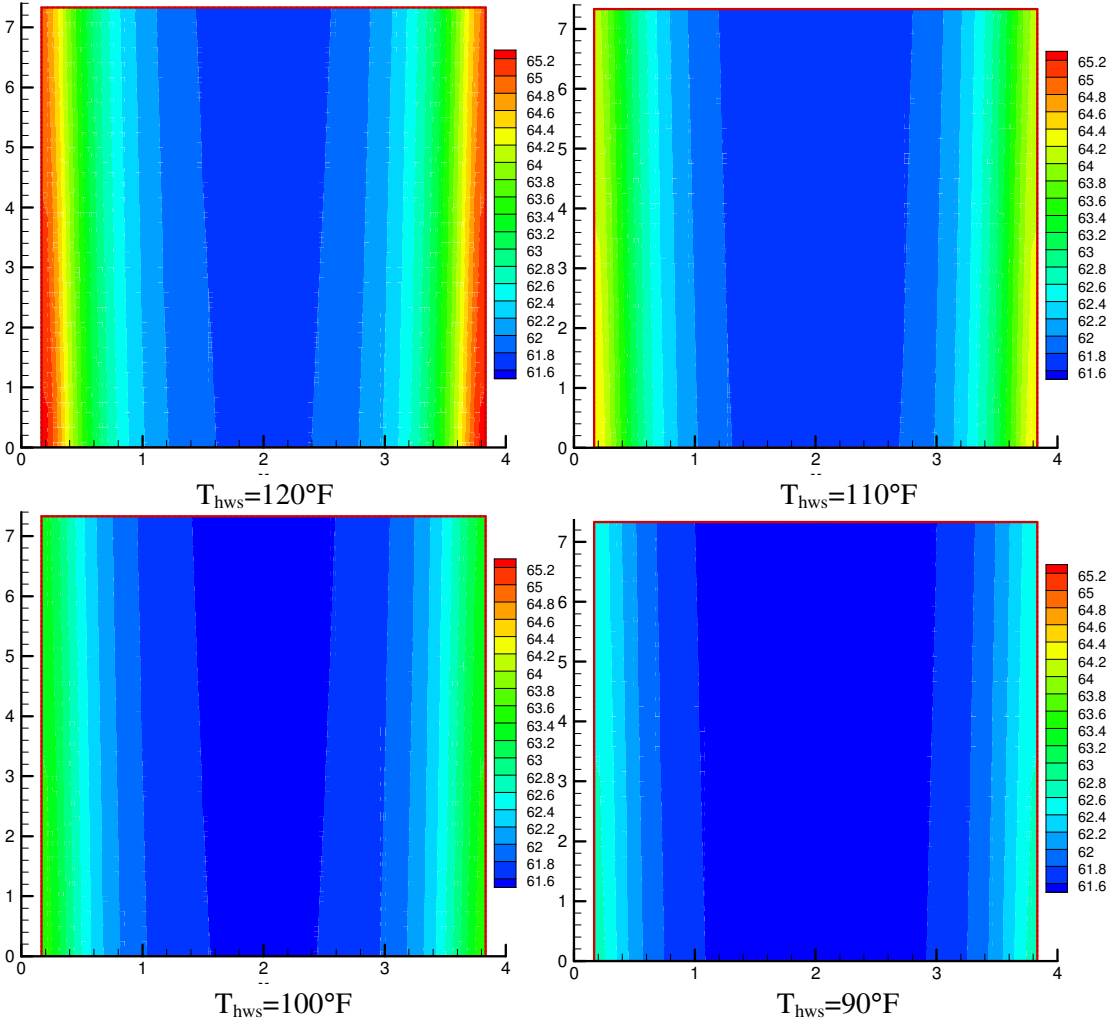
Figure 2.20 Window Temperature Profiles for Four Different Hot Water Conditions

As shown in Figure 2.20, the higher the hot water supply temperature, the higher the window edge temperature. The temperature variation from frame to center is higher when the mullion radiation temperature is high. The variation is about 3°F when the hot water temperature is 120°F. The variation decreases to 1°F, when the hot water temperature is 90°F. However, the temperature at the center of the glass only increases by approximately 0.2°F, as shown in Figure 2.21, when the supply water temperature increases from 90°F to 120°F. The inner window glass has a large temperature gradient within 1 foot from the window mullion. The temperature gradients in the two feet of glass in the center of the window are very small.

Table 2.1 Window Glass Temperature Variation at Four Different Hot Water Supply Temperature Conditions with $T_o=38^oF$

	$T_{hws}=120^oF$	$T_{hws}=110^oF$	$T_{hws}=100^oF$	$T_{hws}=90^oF$
Edge	64.867	64.074	63.297	62.535
Center	61.706	61.622	61.539	61.459
Average	62.56	62.289	62.017	61.752
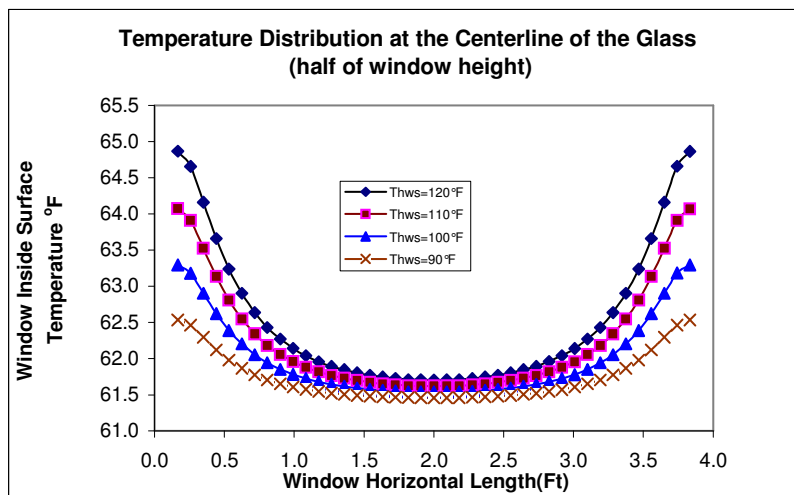
Figure 2.21 Inner Surface Temperature Distributions at the Midpoint of the Window Height

Table 2.1 shows the maximum and minimum temperatures at the halfway mark of the window height for four conditions. The overall average temperatures are also shown in Table 2.1.

It can be found that the average temperature only varies about 0.8 $°$F, when the hot water supply temperature varies from 90 $°$F to 120 $°$F.

2.7.2 The Effect of Space between Mullions

The space between two mullions has an insignificant impact on the heating capacity of each mullion, which can be deduced from Table 2.2. The heating capacity of each mullion depends upon the supply water temperature, the conductive resistance of each mullion and the total surface area of the mullion radiator (the tube surface plus the fin), and is almost independent of the space between the two mullions. However, the space between the two mullions affects the inside temperature distribution of the window glass. Figures 2.20 and 2.21 show that the inside glass temperatures within one foot from the mullions are affected by mullion temperature. When mullion spacing is small, a greater percentage of window glass surface will be affected by the mullion temperature. The average inside surface temperature of the window glass will be slightly increased. Table 2.2 shows the heating capacity and surface temperatures for four different mullion spacings. It can be seen that the surface temperatures are almost the same at four mullion spacings or window widths. The average window temperature is affected slightly.

Table 2.2 Mullion Performance at Different Window Widths

Window Width (Mullion Space)	L=3.5ft	L=4.0ft	L=4.5ft	L=5.0ft
Hot Water Supply Temperature $°$F	120	120	120	120
Heating Input Per Mullion (Btu/(hr*mullion)	801.036	801.500	801.614	801.710
Tube Surface Temperature $°$F	107.886	107.884	107.882	107.881
Fin Surface Temperature $°$F	103.390	103.388	103.387	103.386
Window Frame Temperature $°$F	101.540	101.540	101.539	101.528
Average Window Glass Inside Surface Temperature $°$F	62.726	62.559	62.427	62.318

2.7.3 Mullion Fin Length

The mullion fin length affects the total heat transfer area. The heat transfer rate from mullion to room air and window glass increases when the mullion fin length increases. The average

window inside glass temperature will also increase. Table 2.3 compares the heating input per mullion and surface temperatures at four different fin lengths when the hot water supply temperature is 120°F. Table 2.3 shows that the heating input to the indoor space increases with an increasing mullion fin length. The heating capability will increase about 5% when the fin length increases by 15mm (0.59in) from its current value of 45mm (1.83in). The window frame temperature and average fin surface temperature decrease when the fin length increases.

Table 2.3 Mullion Performance at Different Mullion Fin Lengths

Mullion Fin length	L=30mm (1.18in)	L=45mm (1.83in)	L=60mm (2.36in)	L=75mm (2.95in)
Hot water Supply temperature °F	120	120	120	120
Heating Input Per Mullion Btu/(hr*mullion)	764.40	801.30	824.636	848.77
Tube Surface Temperature °F	108.41	107.89	107.54	107.23
Fin Surface Temperature °F	105.74	103.40	101.84	100.00
Window Frame Temperature °F	103.21	100.5	98.42	96.27
Average Window Glass Inside Surface Temperature °F	62.38	62.56	62.70	62.86

The length of the mullion fins is not only decided by the heating load, but also by the space available and the window appearance. A long fin will make some space close to windows not as useful, and affect the overall aesthetics of the indoor space.

2.7.4 Thermal Conductivity of Mullion Double Tubes

The thermal conductivity of the mullion double tubes is a primary factor affecting the heating capacity and surface temperature of the mullions. The double tubes and gap-filling material are used to control the surface temperature of the mullion. The total mullion tube conductive thermal resistance can be varied by using different gap-filling materials. The filling lowers the mullion heating capacity. However, when the mullion is used for cooling, the double tube structure and gap-filling material will increase the mullion surface temperature and reduce the risk of moisture condensation on the mullion surface.
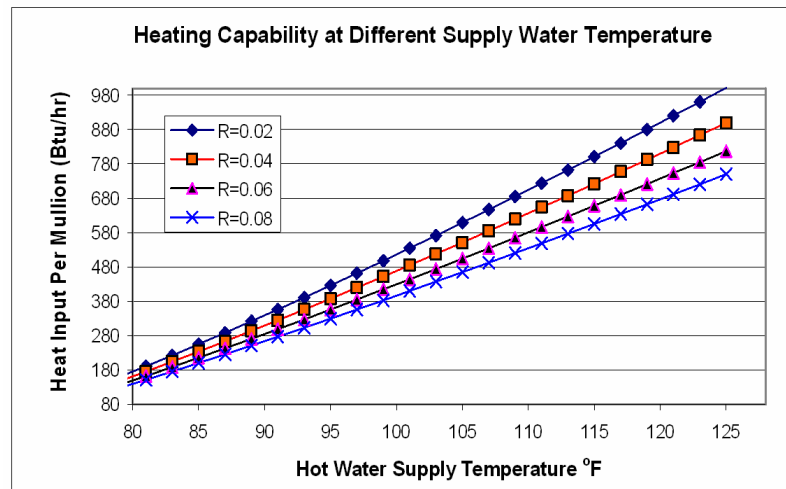
Figure 2.22 Heating Capacity of Mullions at Four Different Values of Tube Wall Thermal Resistance

Figure 2.22 shows the mullion heating input to the space at four different values of tube wall thermal resistance. From this figure, it can be seen that the heating capacity of one mullion can increase about 11% if the conductive resistance of the tube is reduced from 0.04 (ft^2-hr-$^\circ$F)/Btu to 0.02 (ft^2-hr-$^\circ$F)/Btu. The mullion heating capacity will decrease about 9% if the conductive resistance of the tube increases from 0.04 (ft^2-hr-$^\circ$F)/Btu to 0.06 (ft^2-hr-$^\circ$F)/Btu.

Figure 2.23 shows that the mullion tube surface temperature varies dramatically with changes in mullion tube thermal resistance. The tube surface temperature can increase about 4°F, if the conductive resistance of the tube decreases from 0.04 (ft^2-hr-$^\circ$F)/Btu to 0.02 (ft^2-hr-$^\circ$F)/Btu at a hot water temperature of 125°F.
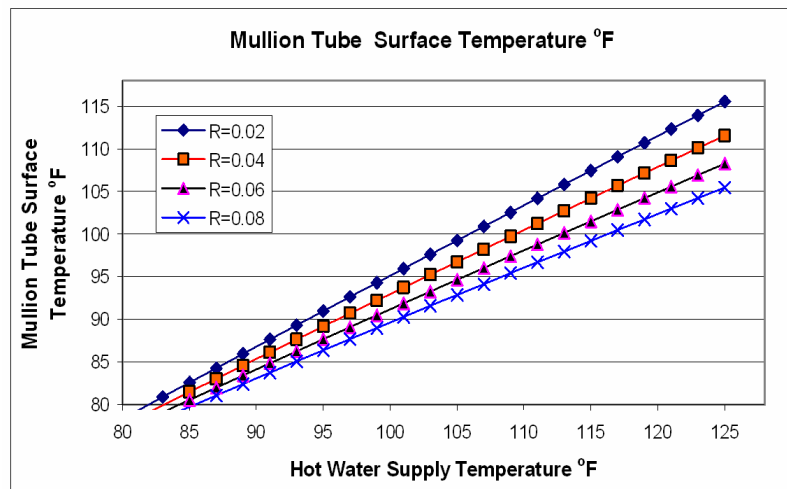
Figure 2.23 Mullion Tube Surface Temperature at Four Different Values of Tube Wall Thermal Resistance

2.7.5 Window Frame Thermal Conductivity

The current window frame has a one-inch insulated thermal gap. The typical thermal conductivity of this type of window frame is about 0.49Btu/(ft^2-hr-$°F$). The corresponding R-value is 2.04(ft^2-hr-$°F$)/Btu. The thermal resistance of the window frame affects the heat loss from the inside to the outside. Figure 2.24 shows that the heat input from the mullion increases about 9% when the window frame thermal resistance drops from 2.0 (ft^2-hr-$°F$)/Btu to 1.0(ft^2-hr-$°F$)/Btu. The window frame temperature also drops from 104.3°F to 101.7°F, because the conduction heat loss increases. However, when the thermal resistance of the window frame increases from 2.0(ft^2-hr-$°F$)/Btu to 3.0(ft^2-hr-$°F$)/Btu, the heat input from a mullion only decreases about 3%. The change in heat input from a mullion is not a linear function of the change of window frame thermal resistance.
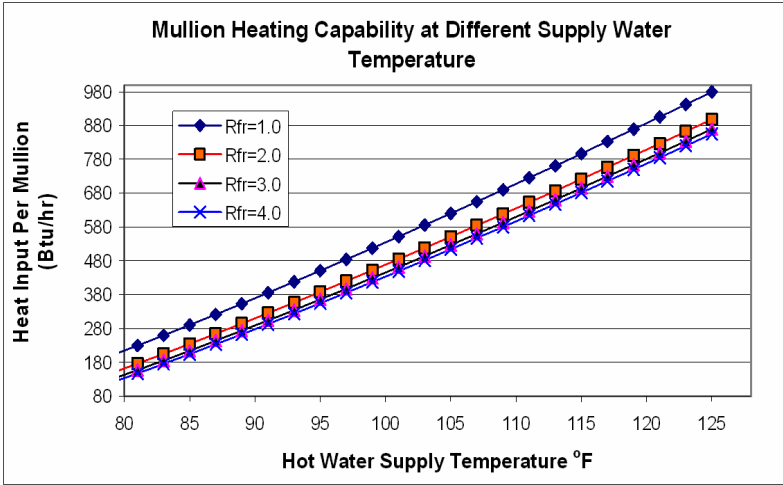
Figure 2.24 Heating Capacity of Mullions at Four Different Window Frame Thermal Resistances
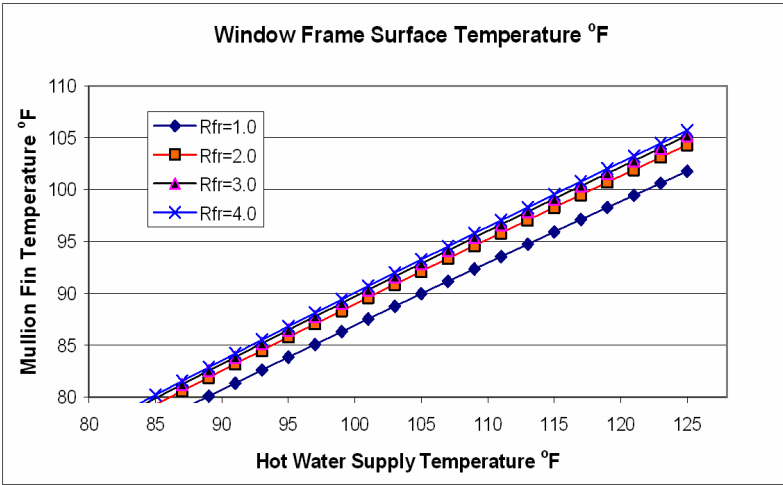
Figure 2.25 Window Frame Surface Temperature at Four Different Window Frame Thermal Resistances

Figure 2.25 shows how the window frame temperature varies with different window frame thermal resistances. At a hot water temperature of 125°F, the frame temperature drops about 2.6°F when the frame resistance decreases from 2.0(ft^2-hr-$^{\circ}$F)/Btu to 1.0(ft^2-hr-$^{\circ}$F)/Btu. The frame temperature increases about 0.9°F when frame resistance increases from 2.0(ft^2-hr-$^{\circ}$F)/Btu to 3.0(ft^2-hr-$^{\circ}$F)/Btu. The change of frame surface temperature is not a linear function

of the change of frame thermal resistance. The smaller the window frame thermal resistance, the larger the temperature drop from mullion tube to the frame and the higher the heat loss from the window frame to the outside air.

2.7.6 Effect of Solar Radiation

The incidence of solar radiation on the window surface varies with the orientation of the windows, the location of surrounding buildings, and the season. Solar radiation definitely affects window surface temperatures and the building load. It is very difficult to evaluate the effect of solar radiation on all window surfaces. The south and west-facing windows gain significant solar radiation in the winter when the outside louver of the IW is at an angle of 90° - 145°. The north and east-facing window gain much less solar radiation in winter. Because of the effect of solar radiation, the measured window inside surface temperatures at different orientations vary by up to 6°F, which includes errors with the sensors. In the summer, the solar radiation seldom strikes directly on the surface of the windows because of the louver shades. Thus, variations in the window surface temperature should be smaller. Solar incidence rarely affects the mullions because of the shading of the window frame.
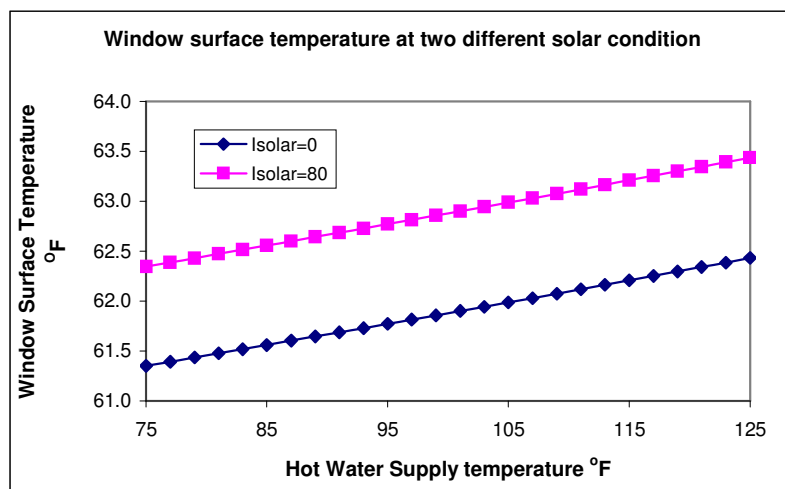
Figure 2.26 South Facing Window Inside Surface Temperature at Two Different Solar Conditions
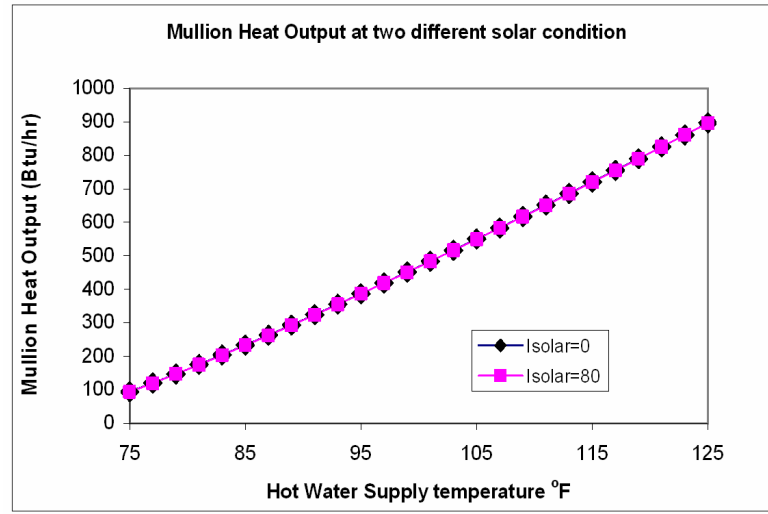
Figure 2.27 Mullion Heat Input at Two Different Solar Conditions

To evaluate the effect of the solar radiation on the window surface, the following assumptions were made: (1) The window faces south; (2) The average Pittsburgh in January radiation, 960 Btu/(ft^2*day), is equal to an average of 80 Btu/(ft^2*hr) in daytime; (3) all window areas face the sun; (4) The outside air temperature is 38°F and the zone air is 72°F; (5) The absorption of the outside layer of double panes is 0.2 (ASHRAE 2006).

The simulated results are shown in Figure 2.26. For a south-facing window, the average inner glass surface temperature increases about 1.0°F when the whole south-facing glass can see the sun in winter. Figure 2.27 illustrates that the mullion heat input to the space is almost the same, with or without the presence of solar radiation.

2.8 Performance Correlations for the IW Mullion Heating and Cooling System

The performance of IW mullion system can be estimated by the following equations, which are based on the analysis of the detailed simulation results.

At the heating condition:

$$T_{ret0} = 0.7845 * T_{hws} + 15.369 \tag{2.40}$$

$$D_1 = -72 * \left[0.0268 * \frac{T_{hws} - 80}{40} + 0.1351 \right] \tag{2.41}$$

$$D_2 = 0.3199 * \left[\frac{\dot{m}}{0.23}\right]^3 - 1.0182 * \left[\frac{\dot{m}}{0.23}\right]^2 + 1.1185 * \left[\frac{\dot{m}}{0.23}\right] + 0.5798 \quad (2.42)$$

$$T_{ret} = D_2 * \left[\left(0.0268 * \frac{T_{hws} - 80}{40} + 0.1351\right) * T_a + D_1 + T_{ret0}\right] \quad (2.43)$$

At the cooling condition:

$$T_{ret0} = 0.8067 * T_{cws} + 13.485 \quad (2.44)$$

$$D_1 = -72 * \left[\left(\frac{T_{cws} - 45}{20}\right) * (-0.0166) + 0.1577\right] \quad (2.45)$$

$$D_2 = -0.2 * \left(\frac{\dot{m}}{0.23}\right)^3 + 0.6406 * \left(\frac{\dot{m}}{0.23}\right)^2 - 0.71 * \left(\frac{\dot{m}}{0.23}\right) + 1.2694 \quad (2.46)$$

$$T_{ret} = D_2 * \left[\left(\frac{T_{cws} - 45}{20} * (-0.0166) + 0.1577\right) * T_a + D_1 + T_{ret0}\right] \quad (2.47)$$

$$\dot{Q}_{total} = \dot{m}_{total} * 4.186 * (T_{hws} - T_{ret}) \quad (2.48)$$

In above equations, $\dot{m}$ is the water flow rate passes through single mullion. $\dot{m}_{total}$ is the total flow rate of mullion system. D_1 is room air temperature correction factor; D_2 is the flow rate correction factor. The correlations described above only apply to the IW system, because they are derived based on the dimensions and material properties of the mullions used in the IW.

2.9 Summary

This chapter studies the heat transfer principles of window mullion heating and cooling. Two heat transfer models have been set up through differential analysis. The simulation results have been compared with 10 day's measured data. The comparison shows that the heat transfer models predict the measured temperatures with a root mean square error (RMSE) of the hot water return temperature, the mullion surface temperature, and the window surface temperature of 0.90°F, 0.98°F and 1.15°F, respectively. The simulation study leads to the following conclusions:

Hot water supply temperature and chilled water supply temperature are the primary factors that affect the heating or cooling capacity of window mullions and the mullion surface

temperature. Hot/chilled water return temperature, mullion surface temperature and window frame temperature are all quasi-linear functions of the hot water supply temperature.

Window surface temperature distribution is affected by the mullion surface temperature and the outside air temperature. The temperature gradient on the glazing surface within one foot from mullions is much higher than in the central part of the window. The temperatures in the central 2 feet of a 4-foot window show almost no influence by the mullion surface temperature.

The sensitivity study in the discussion section showed that the conductive thermal resistance of the mullion double tubes plays a decisive role in controlling the mullion and window frame temperatures. The double tubes and gap fillings increase the thermal resistance of the mullion tubes, which results in a lower surface temperature for heating and a higher surface temperature for cooling. The higher surface temperature for cooling may be intended to lower the risk of moisture condensation on the surface of the mullion in the cooling condition. However, the enhanced thermal resistance decreases the heating and cooling capacity of the mullion. If the mullions are only used for heating, a single tube structure is recommended.

Window frame thermal resistance affects the frame surface temperature and heat loss from the mullion to the outside air. The change of frame surface temperature and the heat loss to the outside air is a non-linear function of the change of framed thermal resistance, as expected. At a hot water temperature of 125°F, the frame temperature drops about 2.6°F, when frame resistance decreases from 2.0(ft^2-hr-$^{\circ}$F)/Btu to 1.0(ft^2-hr-$^{\circ}$F)/Btu. The frame temperature increases about 0.9°F when frame resistance increases from 2.0(ft^2-hr-$^{\circ}$F)/Btu to 3.0(ft^2-hr-$^{\circ}$F)/Btu. The smaller the window frame thermal resistance, the larger the temperature drop from the mullion tube to the frame and the higher the heat loss from the window frame to the outside.

From a design perspective, the window width or spacing between the mullions has little impact on the heating capacity or mullion surface temperature. However, the space between the mullions will somewhat affect the window's inner surface temperature distribution and the window's average temperature. When the window width decreases from 5 feet to 3.5 feet, the average window surface temperature increases from 62.32°F to 62.73°F at an ambient temperature of 38°F. Increasing the mullion fin length will increase the heating or cooling capacity of the mullion because of the heat transfer area increase. If the fin length increases from 45mm (1.83 inchs) to 60mm (2.36 inches), the heating capacity of one mullion will increase about 3.1%.

The effect of solar radiation on the temperature distribution of the window panes depends upon window orientation, building location and season of the year. For a south-facing window under the sun on a typical winter day, the inside glass temperature will increase about 1°F when solar radiation is considered.

CHAPTER III

THE PERFORMANCE STUDY OF OVERHEAD RADIANT PANELS

3.1 Introduction

The overhead radiant panels are the other type of radiant device in the IW, as shown in Figure 1.2. This type of radiant panel is also called a free-hanging ceiling radiant panel. The overhead radiant panel can be used for both heating and cooling in the IW, and there is no topside insulation on these panels. The overhead radiant panels are supposed to meet a part of the sensible load of the IW, with panel output varied by controlling the supply water temperature. Significant research has been done regarding the heat transfer models, and the thermal comfort and efficiency of ceiling radiant panels. Chen and Kooi (1988) developed a radiant panel simulation model which considered the radiant ceiling panel as an indoor surface exchanging heat with room air by convection and other room surfaces through radiation. Kilkis et al. (1994) proposed an in-slab type panel model. They pointed out that the heat transfer in a panel-cooled room and the cooling panel itself might be represented by a quasi-steady state natural convection model by assuming uniform panel surface temperatures. Stetius and Feustel (1995) developed a 2-D radiant panel model by simplifying heat diffusion equations for an in-slab type panel. Conroy and Mumma (2000) derived an analytical model for a top insulated metal ceiling radiant panel. This model was based on the study of solar collectors conducted by Duffie and Beckman (1991). The basic methodology in this model was to determine the panel cooling capacity by finding the unknown mean panel surface temperature (Tpm) in an iterative process. However, the detailed structure of radiant panels varies greatly; it is hard to use one general model to estimate the ceiling panel capacity in the IW. The objective of this chapter is to develop a specific model to estimate the heating and cooling capacity of the radiant panels used in the IW (no topside insulation) with a focus on the impact of thermal contact resistance between the tubes and aluminum panels.

Some researchers (Awbi and Hatton 2000, Jeong and Mumma 2003b), in recent years, have proposed a mixed convection heat transfer coefficient to calculate the radiant panel capacity, because the ventilation diffusers near the ceiling panels create a forced air flow across the ceiling panels. However, the air velocity near the panel surfaces is related to the diffuser locations. In the IW, the ventilation diffusers are either on the occupants' desks or on the floor, and thus have

little impact on the convection heat transfer across the radiant panels. This chapter will use the natural convection heat transfer coefficient recommended by ASHRAE 2004.

3.2 Simulation Assumptions

The overhead panel shown in Figure 1.2 consists of several panel modules. The two pieces of the panels are connected together by a U-shaped tube to form one module. One panel is about 7ft long, and one module is 14ft long (including the two panels). A cross section of the copper tube and aluminum panel is shown in Figure 3.1. The left side of Figure 3.1 is the detailed cross-section of the panel, which is simplified as the right side in the simulation process. The bottom of Figure 3.1 is the simplified thermal resistance network. The first term, $\dfrac{1}{h_{in}\pi r}$, is the thermal resistance between the water and the tube surface. The second term, $R_s + \dfrac{L}{kD}$, is the thermal contact resistance and thermal conduction resistance of the fin root section. The third term, $\dfrac{1}{U_o(D + F_f(W + D))}$, is the thermal resistance of the aluminum fin. U_o is the average convection heat transfer coefficient of the upper and bottom surfaces of the panel. F_f is the fin coefficient, defined in the next section. The tube is a 0.5 inch nominal diameter copper tube. The width of the panel is about 8 inches. All the symbols used in this figure can be found in the nomenclature section.

Figure 3.1 Detail of an Overhead Radiant Panel

3.3 Heat Transfer Model for Overhead Radiant Panels

3.3.1 Heat Transfer Through the Aluminum Panel

The heat transferred from the radiant panel to the indoor space can be divided into two parts. One is the heat transferred from the root section, $\dot{q}_1$, which corresponds to the width of D in Figure 3.1. The other is the heat transferred from the fin section, $\dot{q}_2$, which equals the width of (W-D) in Figure 3.1. These two parts of the heat flux can be calculated by the following equations:

$$\dot{q}_1 = D\frac{U_o}{2}(T_b - T_a) \tag{3.1}$$

$$\dot{q}_2 = F_f U_o (W - D)(T_b - T_a) \tag{3.2}$$

T_a is the air temperature. T_b is the temperature in the shaded section in Figure 3.1. F_f is the fin heat transfer coefficient, which can be determined by the following equations:

$$F_f = \frac{\tanh(M(W-D)/2)}{M(W-D)/2} \tag{3.3}$$

$$M = \sqrt{\frac{2U_0}{k*\delta}} \tag{3.4}$$

The total heat transfer from the panel can be written as:

$$\dot{q}_p = \dot{q}_1 + \dot{q}_2 = \frac{T_b - T_a}{\dfrac{1}{U_o(\dfrac{D}{2} + F_f(W - D))}} \tag{3.5}$$

By considering the water-side resistance, contact resistance and conduction resistance, shown in Figure 3.1 as the thermal network, the heat transferred from the water to the radiant panel can be expressed as:

$$\dot{q}_p = \frac{T_f - T_a}{\dfrac{1}{h_{in}\pi r} + \dfrac{L}{KW} + R_s + \dfrac{1}{U_o(\dfrac{D}{2} + F_f(W - D))}} \tag{3.6}$$

The panel heat transfer can also be calculated by defining the panel heat transfer efficiency factor F_1, which is a ratio of the overall heat transfer coefficient between the fluid and the room air to the overall heat transfer coefficient between fin and the room air.

$$\dot{q}_p = WU_o(T_f - T_a) * F_1 \qquad (3.7)$$

The factor F_1 can be found by equating Equations (3.6) and (3.7).

$$F_1 = \frac{\dfrac{1}{WU_o}}{\dfrac{1}{h_{in}\pi r} + \dfrac{L}{kW} + R_s + \dfrac{1}{U_o(\dfrac{D}{2} + F_f(W+D))}} \qquad (3.8)$$

The water-side convection heat transfer coefficient, h_{in}, can be found by Equations (2.10) and (2.11) in the previous chapter.

3.3.2 Panel Average Temperature T_{pm}

The panel average temperature can be found by performing an integration along the water flow direction of one module. Taking one element, as shown in Figure 3.2, the energy balance can be written as the following equations:

$$\dot{q}_p * dx + \dot{q}_s * dx = -\dot{m}_f C_P * dT_f \qquad (3.9)$$

$$\dot{q}_s \approx \frac{U_o}{2}\left(\frac{\pi D}{2} + 2L + D\right)\left(T_f - T_a\right) \qquad (3.10)$$
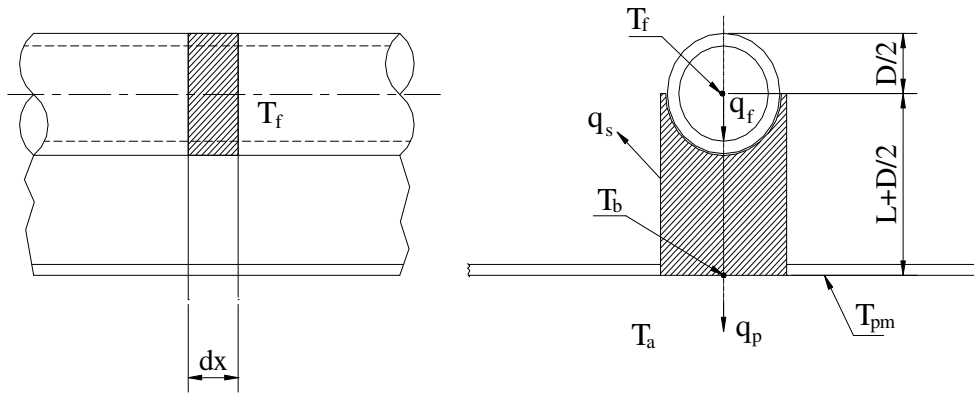
Figure 3.2 Differential Element Diagram of a Radiant Panel

By substituting Equations (3.7) and (3.10) into Equation (3.9), the following governing equation can be obtained:

$$P * U_o * (T_f - T_a) = -\dot{m}_f C_P \frac{dT_f}{dx} \tag{3.11}$$

$$P = F_1 W + \frac{1}{2}\left(\frac{\pi D}{2} + 2L + D\right) \tag{3.12}$$

Letting $T = T_f - T_a$, Equation (3.11) can be written as the differential equation:

$$\frac{dT}{T} = -\frac{PU_o}{\dot{m}C_P} dx \tag{3.13}$$

with the boundary condition:

$$x = 0, \qquad T = T_{fi} - T_a \tag{3.14}$$

Equation (3.13) can be solved as:

$$\theta = \frac{T_f - T_a}{T_{fi} - T_a} = e^{-\frac{PU_o}{\dot{m}C_P}x} \tag{3.15}$$

At the module outlet, the water temperature is T_{fo}, which can be expressed as the following equation:

$$T_{fo} = T_a + (T_{fi} - T_a) * e^{-\frac{PU_o}{\dot{m}C_P}*L1} \tag{3.16}$$

L1 is the length of one module, which equals two panel lengths in the IW. Conroy and Mumma (2001) defined a heat recovery factor F_R that relates the actual sensible heat of a panel to the sensible heat if the whole panel surface were at the fluid inlet temperature. The total sensible load can be expressed as in Equation (3.18). Once the outlet temperature is known, the heat recovery factor of the panel can be calculated by the following equation:

$$F_R = \frac{\dot{m}C_P(T_{fo} - T_{fi})}{A_P U_o (T_a - T_{fi})} \tag{3.17}$$

The overall heating or cooling capacity of one module can be written as the following equations by applying the concept of the heat recovery factor and the panel mean temperature:

$$\dot{q}_o = F_R A_P U_o (T_a - T_{fi}) = \dot{m} C_P (T_{fo} - T_{fi}) \tag{3.18}$$

$$\dot{q}_o = U_o A_P (T_a - T_{pm}) \tag{3.19}$$

Based on Equations (3.18) and (3.19), the panel average temperature can be obtained as:

$$T_{pm} = T_{fi} + \frac{\dot{m} C_P (T_{fo} - T_{fi})}{A_p U_o F_R} (1 - F_R) \tag{3.20}$$

3.3.3 Overall Heat Transfer Coefficient, U_o

The overall heat transfer coefficient, U_o, in the previous process is unknown. U_o can be found by the following procedure. The total heat transfer rate per unit panel area can be expressed as the summation of bottom convection, radiation, and top convection and radiation.

$$\dot{q}_o = (\dot{q}_c + \dot{q}_r)_b + (\dot{q}_c + \dot{q}_r)_t \tag{3.21}$$

$$\dot{q}_{c,b} = h_{c,b} (T_{pm} - T_a) \tag{3.22}$$

$$\dot{q}_{r,b} = h_{r,b} (T_{pm} - AUST) \tag{3.23}$$

$$\dot{q}_{c,t} = h_{c,t} (T_{pm} - T_a) \tag{3.24}$$

$$\dot{q}_{r,t} = h_{r,t} (T_{pm} - AUST) \tag{3.25}$$

The AUST in the above equation is defined in Equation 2.39. The convection heat transfer coefficient can be found by the following equations, which are from Chapter 6 of the *ASHRAE Handbook*, 2004.

$$h_{c,b} = 0.13 * (T_{pm} - T_a)^{0.25} \quad \text{(Heating)} \tag{3.26}$$

$$h_{c,b} = 0.31 * (T_a - T_{pm})^{0.31} \quad \text{(Cooling)} \tag{3.27}$$

$$h_{c,t} = 0.13 * (T_a - T_{pm})^{0.25} \quad \text{(Cooling)} \tag{3.28}$$

$$h_{c,t} = 0.31 * (T_{pm} - T_a)^{0.31} \quad \text{(Heating)} \tag{3.29}$$

The radiant heat transfer coefficients $h_{r,t}$ and $h_{r,b}$ can be obtained from Equation (3.30). The AUST, which is close to room air temperature, can be obtained from Equation (2.39).

$$h_r = 4\varepsilon\sigma \left(\frac{T_{pm} + AUST}{2} \right)^3 \tag{3.30}$$

Once the overall heat transfer rate, $\dot{q}_o$, is known, the overall heat transfer coefficient can be calculated by the following equation:

$$U_o = \frac{\dot{q}_o}{T_{pm} - T_a}$$ (3.31)

The actual U_o can be found by first giving an estimated T_{pm} value at the beginning of the calculation, and then iterating the T_{pm} and the U_o value from Equation (3.1) until the two parameters converge.

3.4 Discussion

3.4.1 The Performance of Radiant Panels in Summer

Figure 3.3 shows the radiant panel performance in summer. The cooling capacity of the panel decreases as the supply temperature of chilled water increases. When the chilled water supply temperature is 45°F, the cooling capacity of the panel is approximately 71.0 Btu/(hr-ft^2). It decreases to 44.6 Btu/(hr-ft^2), when the chilled water supply temperature increases to 55°F. In order to avoid condensation over the panel surface, the supply water temperature is normally higher than 55 °F. The cooling capacity of the overhead panel is normally between 16.9 and 44.6 Btu/(hr-ft^2) as the chilled water supply temperature varies between 55°F and 65°F. Several factors affect the cooling capacity of the panel. Room air temperature is an important factor that can affect the cooling capacity of the radiant panel; the higher the room air temperature, the higher the temperature difference between the panel surface and the room air. The panel cooling capacity increases about 58.9% when the room air temperature increases from 68°F to 75°F at a chilled water temperature of 55°F. It may drop about 22.4% when the room air temperature decreases from 72°F to 68°F. The chilled water flow rate also has some impact on the panel's cooling capacity. The panel's cooling capacity decreased about 11.4% when the flow rate decreased to half of the design flow rate.

Figure 3.4 indicates the average surface temperature of the radiant panel, which is about 0.5 °F to 3.5°F higher than the inlet chilled water temperature, depending upon the room air temperature and the inlet water condition. Figure 3.4 also illustrates that the room air temperature has little impact on the panel surface temperature. The panel surface average temperature increases about 0.7°F when the room air temperature increases from 68°F to 75°F. The performance of the radiant panel in the heating mode is shown in Appendix III.
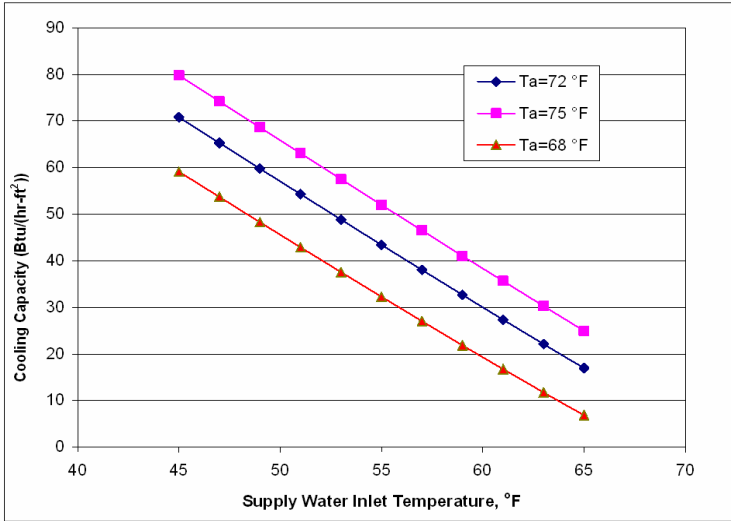
Figure 3.3 The Cooling Capacity of the Overhead Panel
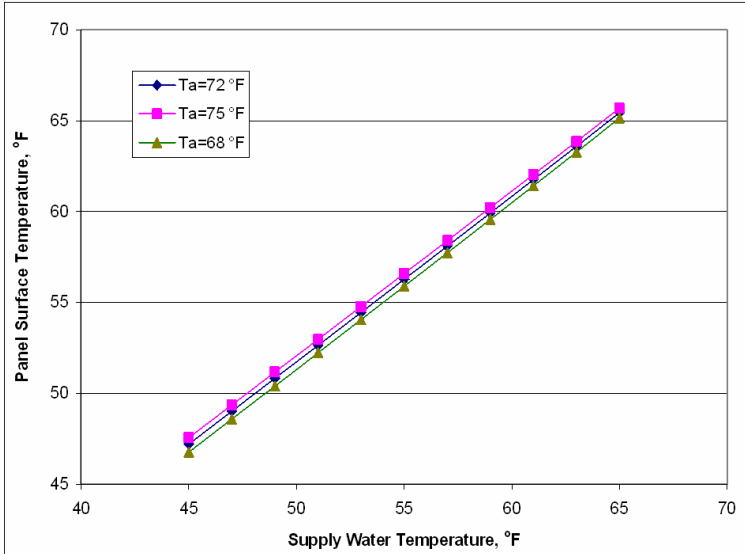
Figure 3.4 The Average Panel Surface Temperature
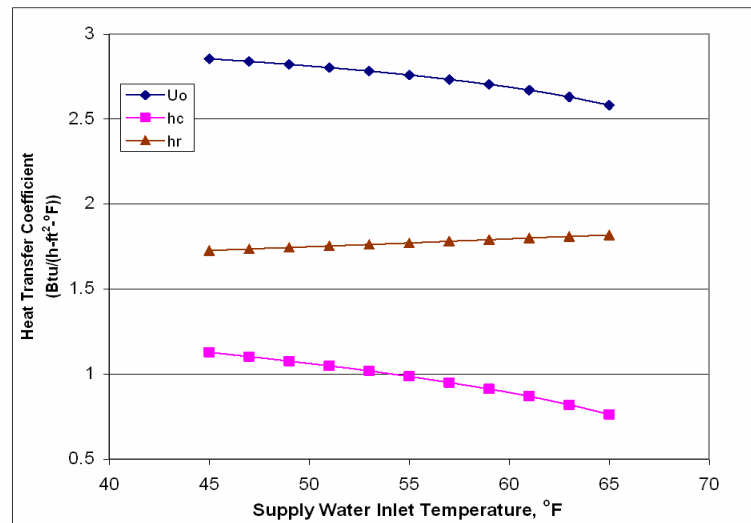
Figure 3.5 Heat Transfer Coefficients of the Radiant Panel in the Cooling Model

Figure 3.5 shows the change in the heat transfer coefficient in the panel cooling model. The convection heat transfer coefficient decreases when chilled water supply temperature increases, because the temperature difference between the panel surface and the room air gets smaller. The radiant heat transfer coefficient increases when supply water temperature increases because the radiant coefficient is a function of the average temperature of the panel surface and the room air. The overall heat transfer coefficient, U_o, decreases when the supply water temperature increases. In general, the overall heat transfer coefficient does not vary significantly.

3.4.2 The Performance of the Radiant Panel in Winter

Figure 3.6 shows the heating capacity of the overhead radiant panel, which increases as the hot water supply temperature increases. At the hot water supply temperature of 120°F, the heating capacity of the panel is 144.1 Btu/(hr-ft^2), while it is 19.9 Btu/(hr-ft^2) at a hot water supply temperature of 80°F. The supply water temperature is a primary factor that affects the heating capacity of the overhead panel, but the room air temperature also affects the heating output of the radiant panel. The lower the room air temperature, the higher the panel heating output. The heating capability increases about 8.5% at a supply water temperature of 120ºF, when the room air temperature decreases from 72ºF to 68°F. The simulation study also finds that the hot water flow rate has a slight impact on the heating capacity of the panels. The heating capacity decreases about 14.2%, if the flow rate is reduced to half of the design value.

Figure 3.7 shows that the average panel surface temperature is proportional to the inlet water temperature. The average surface temperature is about 0.5 °F to 6.0ºF lower than the inlet hot water temperature when the hot water supply temperature varies between 80°F and 120°F. Figure 3.7 also indicates that the room air temperature slightly affects the panel surface temperature. The higher the room air temperature, the higher the radiant panel surface temperature. The performance of the radiant panel at cooling condition is shown in Appendix IV.

Figure 3.8 illustrates the overall heat transfer coefficient, U_o, the convective heat transfer coefficient, hc, and the radiant heat transfer coefficient, hr, all of which increase as the supply water temperature increases. The overall panel heat transfer coefficient varies from 2.7 Btu/(hr-ft^2-°F) to 3.4 Btu/(hr-ft^2-°F) and the natural convection heat transfer coefficient changes from 0.79 Btu/(hr-ft^2-°F) to 1.32 Btu/(hr-ft^2-°F), as the supply water temperature changes from 80ºF to 120°F. The reason is that the temperature difference between the panel surface and the room air increases when the hot water supply temperature increases.
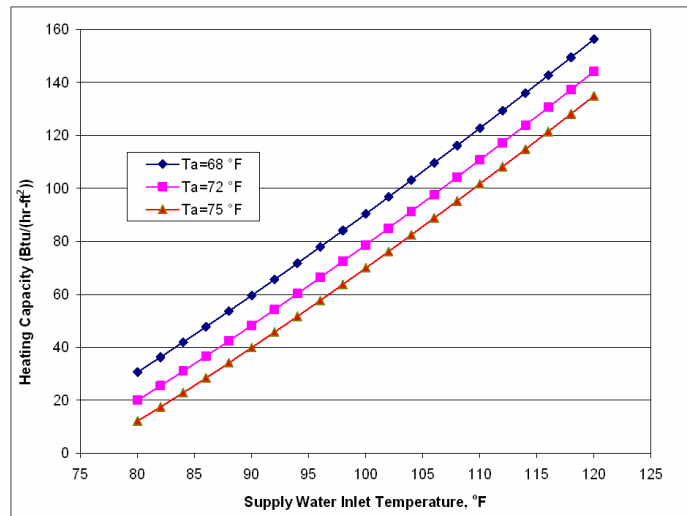
Figure 3.6 The Heating Capacity of the Overhead Panel
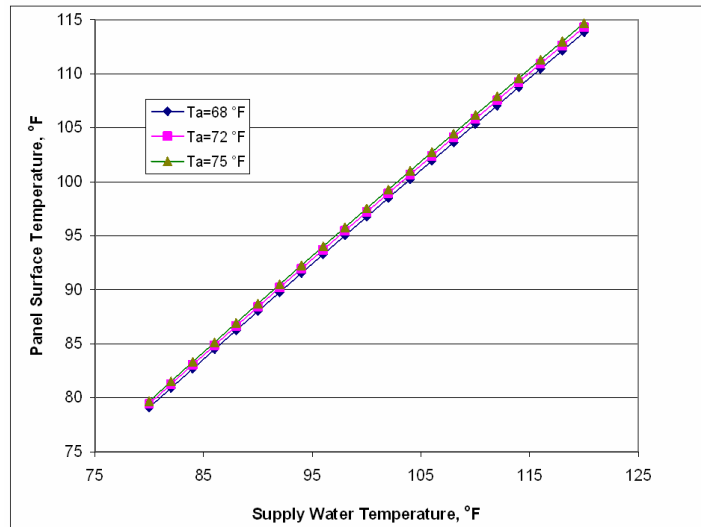
Figure 3.7 The Overhead Panel Surface Average Temperature
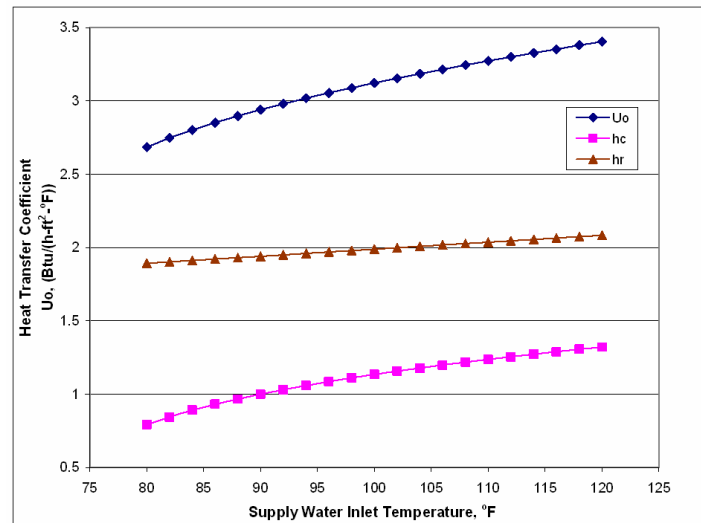
Figure 3.8 Heat Transfer Coefficient of the Radiant Panel in the Heating Model

3.4.3 The Impact of the Thermal Contact Resistance on the Performance of the Radiant Panel

In Figure 3.1, the aluminum panel is attached to the water tube by a clip-shaped structure. The heat flows from the water tube to the aluminum panel. When the two solid bodies make contact, a temperature drop across the interface occurs. This is caused by contact thermal

resistance between the water tube and the clip, which affects the radiant panel performance. Thermal contact resistance is a complicated phenomenon, influenced by the contact pressure, contact area, surface roughness, etc. Calculation of the thermal contact resistance is difficult, even impossible, because of the difficulty inherent in measuring the contact area. When aluminum panels are attached to the copper water tube, normally a thermally conductive gel is used to fill the air cavity and increase the thermal conductivity between the tube and the panel. In the above analysis, contact is assumed to be ideal. The thermal contact resistance, Rs, in Equation (3.6) and Equation (3.8) is assumed to be zero. In a real case it is impossible for the thermal resistance to be zero if any air gaps exist.

Figures 3.9 and 3.10 show the overhead panel performance under different thermal contact resistances, when the room air temperature is 72°F. As shown in Figure 3.9, the cooling capacity decreases 18.8% when the thermal contact resistance increases to 0.2 (hr-ft^2-^{o}F)/Btu at an inlet water temperature of 55ºF. The cooling capacity loss varies from 19.2% to 18.1% when the supply water temperature increases from 45°F to 65°F. In Figure 10, the panel heating capacity also decreases when the thermal contact resistance increases. When the thermal contact resistance increase to 0.2 (hr-ft^2-^{o}F)/Btu, the heating capacity loss varies between 18.9% and 22.2% for a supply hot water range of 80ºF to 120ºF, as compared to no thermal contact resistance.
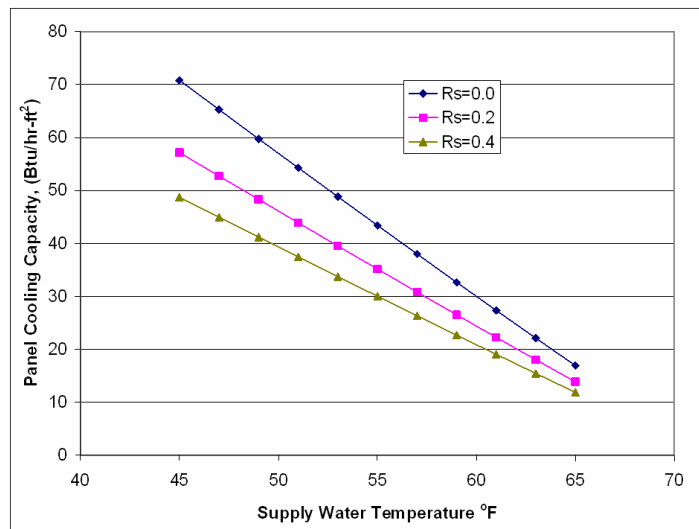
Figure 3.9 Panel Cooling Capacity at Different Thermal Contact Resistances
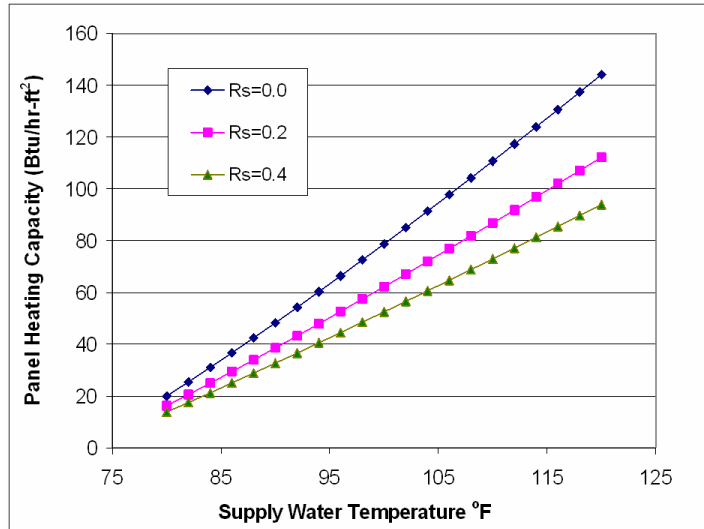
Figure 3.10 Panel Heating Capacity at Different Thermal Contact Resistances

The above analysis indicates that thermal contact resistance has a significant impact on the thermal performance of the radiant panels. Therefore, the design of the connection between the water tube and the aluminum panel is very important. To increase the heating or cooling capacity, the thermal contact resistance should be kept as small as possible. The clip section in Figure 3.1 is normally designed in a circular shape (Xia and Mumma 2006), and the thermally conductive gel is used when the radiant panels are installed. Xia and Mumma, 2006, have estimated that the contact thermal resistance is around 17 Btu/hr-ft^2-°F (R value of 0.06 hr-ft^2-°F/Btu) for a half inch water tube.

3.5 Performance Correlations for Radiant Panels

The performance of the IW overhead radiant panels can be estimated by the following correlations based on the above detailed simulation study.

At the heating condition:

$$\dot{Q}_{h0}^{''} = -6 \times 10^5 * T_{hws}^3 + 0.0263 * T_{hws}^2 - 0.3325 * T_{hws} - 90.977 \tag{3.32}$$

$$D_1 = 9.97 * \frac{T_a - 72}{3.5} \tag{3.33}$$

$$D_2 = -0.1412 * \left(\frac{\dot{m}}{0.22}\right)^2 + 0.4384 * \left(\frac{\dot{m}}{0.22}\right) + 0.7026 \tag{3.34}$$

$$\dot{Q}_H = A * D_2 * \left(\dot{Q}_{ho}^{"} + D_1 \right) \tag{3.35}$$

At the cooling condition:

$$Q_{c0}^{"} = 0.0001 * T_{cws}^3 - 0.015 * T_{cws}^2 - 2.1465 * T_{cws} + 186.79 \tag{3.36}$$

$$D_1 = 9.98 * \frac{Ta - 72}{3.5} \tag{3.36}$$

$$D_2 = -0.1099 * \left(\frac{\dot{m}}{0.22} \right)^2 + 0.3989 * \left(\frac{\dot{m}}{0.22} \right) + 0.7109 \tag{3.37}$$

$$\dot{Q}_C = A * D_2 * \left(\dot{Q}_{Co}^{"} + D_1 \right) \tag{3.38}$$

In the equations above, the units of $\dot{Q}_{h0}^{"}$ and $\dot{Q}_{C0}^{"}$ are Btu/(hr-ft^2) and the units of $\dot{Q}_H$ and $\dot{Q}_C$ are Btu/hr, where $\dot{Q}_H$, $\dot{Q}_C$ are total heating and cooling input of the radiant panels. A is the total panel area. D_1 is the room air correction factor; and D_2 is flow rate correction factor. $\dot{m}$ is the water flow rate in single panel. The correlation equations apply to the IW radiant panels only.

3.6 Summary

This Chapter presents the heat transfer principles of overhead radiant panels. One heat transfer model has been set up, which can be solved for the supply water outlet temperature, the panel average surface temperature, and the overall panel surface heat transfer coefficient. This study has found that the heating and cooling capacity of the overhead panel without top insulation is a semi-linear function of the supply water temperature when the flow rate is fixed.

The cooling capacity of the overhead radiant panel is around 44.63 Btu/(hr-ft^2) at a chilled water supply temperature of 55°F , which is greatly affected by room air temperature and slightly affected by water flow rate. The heating capacity of the overhead radiant panel is around 144.12 Btu/(hr-ft^2) at a hot water supply temperature of 120°F. If the contact thermal resistance is assumed to be 0.06 hr-ft^2-°F/Btu (Xia and Mumma 2006), the heating and cooling would be reduced by 8.3% and 6.8%, respectively. Room air temperature and supply water flow rate both affect the heating input of the overhead radiant panels. The panel capacity increases about 8.5% in heating and decreases about 22.4% in cooling when the room air temperature drops from 72°F to 68 °F, and it decreases about 14.2% if the hot water flow rate is reduced to half the design flow rate.

Thermal contact resistance between the water tubes and the aluminum radiant panels has a significant impact on the thermal performance of the overhead radiant panels. When the thermal contact resistance increases to 0.2 (hr-ft^2-°F)/Btu, the cooling capacity drops about 18.6% and the heating capacity drops about 20.6%. The thermal contact resistance should be reduced to be as small as possible in the design process.

CHAPTER IV

THE THEORETICAL ANALYSIS OF THE IMPACT OF RADIATOR POSITION ON
ENERGY CONSUMPTION AND THERMAL COMFORT

4.1 Introduction

Chapters II and III modeled the heat transfer processes of radiant mullions and overhead radiant panels. However, some questions remain unanswered by this modeling analysis. These questions are what the benefits are by using radiant heating or cooling, why radiant mullions are used, and what is the impact of radiant mullions and overhead radiant panels on energy consumption and thermal comfort. The objective of this Chapter is to quantitatively analyze the impact of the position of radiators on energy consumption and thermal comfort.

4.1.1 Radiant Heating

Radiant heating has a reputation for increasing the comfort level of a space and for lowering energy bills. A radiant heating system uses one or more temperature controlled indoor surfaces on the floor, walls or ceiling to heat the enclosure surfaces and objects first. The warm surfaces then heat the inside air via convection. Because warm enclosure surfaces radiate more energy to a human body than cold surfaces, people tend to feel comfortable even if the air temperature is several degrees lower than in a room with a forced air heating system. A temperature controlled surface is called a radiant panel where the temperature is maintained by circulating water, air or electric current. According to the ASHRAE Handbook (2005), the panel surface temperature is normally lower than 300°F. The radiant heating system may be combined with a central forced air system to supply the heating or cooling required by the space. Such systems are called mixed radiant and convective heating systems or hybrid HVAC systems (ASHRAE Handbook 2004).

Floor heating is one of the oldest and most popular radiant heating systems. Stove and flue gas ducts underneath a building floor constitute the ancient heating systems used in East Asian countries thousands of years ago. The advantages of floor heating are quiet operation and superior comfort. Several investigations (Dale 1993, Olesen 1994, Gibbs 1994) have evaluated the energy consumption and comfort levels provided by this type of heating.

For office buildings, the most practical application of radiant heating is wall or ceiling-mounted heating panels combined with a forced air system. The Hybrid HVAC system provides

more flexible control over the space operative temperature, air distribution velocity and humidity level.

Significant research has been done regarding the mean radiant temperature distribution and comfort level of radiant systems. Steinman et al. (1989) proposed a calculation method for mean radiant temperature and noted that the temperature difference between the room air and unheated internal surfaces may not be small with a radiant heating system when an enclosure has a large set of window surfaces or a high percentage of exterior walls. Tassou et al. (2000) compared radiant and forced air heating systems in two churches. They found that properly located heaters can create a more uniform temperature distribution than a single air heating system in a large space. Chapman et al. (1997) analyzed mean radiant temperature (MRT) distribution in a bedroom and a kitchen in order to analyze the thermal comfort conditions, where the heating panels are mounted to the ceiling.

Several studies have examined the energy consumption associated with radiant heating systems and some compare the consumption of radiant systems to that of air heating systems. DeGreef and Chapman (1998) used an improved methodology to analyze the energy consumption of a 48 square foot bathroom with a radiator mounted to the center of the ceiling. Degreef and Chapman (1998) indicated that the energy required by a 100% radiant heating system is 25% less than that required by a 100% convective heating system to achieve the same average MRT, in the case analyzed. By keeping the operative temperature constant, Chapman et al. (2000) found that the energy consumption of 100% radiant heating is slightly less than (6%) that of a 100% convective heating system in a 3 meter square enclosure without a window. Hanibuchi and Hokoi (2000) compared a floor heating system with a convective heating system; they pointed out that when convective heat exchange is dominant, heat loss through poorly insulated windows is larger than when radiant heat exchange is dominant. Their conclusion was based on keeping the operative temperature at the central point of the tested room constant in the case of floor heating. Most of these studies tend to conclude that radiant heating can save energy compared with a forced air heating system when keeping the operative temperature or the MRT constant.

One of the important factors still untouched by these studies is that the position of the radiators relative to the windows and the outside air supply rate has an impact on energy consumption and comfort distribution in a given space. The location of a radiator can

significantly affect the enclosure surface temperature nearby. If a radiator is near windows, it increases the inside surface temperature of the window and counteracts the down draft to make people near the window feel comfortable. However, this arrangement may increase the heating load. If a radiator is located away from the windows, the surface temperature of the windows is lower. The comfort level near the window may not be as high as in the previously described layout.

4.1.2 Thermal Comfort

The primary objective of the HVAC design is to satisfy the thermal comfort requirement of a conditioned space. Any energy management measures must consider this goal first. ASHRAE Standard 55-2004 defines thermal comfort as the "condition of mind which expresses satisfaction with the thermal environment." Six primary factors affect the thermal comfort of an occupied space: metabolic rate, clothing insulation, air temperature, radiant temperature, air speed and humidity. ASHRAE Standard 55 (2004) specifies the comfort zones appropriate for spaces where 80% of sedentary or slightly active persons find their environment thermally acceptable when their clothing provides between 0.5clo and 1.0clo of thermal insulation. Of the six factors noted above, air temperature, radiant temperature, air speed and humidity can be controlled by the HVAC system. Therefore, the comfort zone is expressed as a range of operative temperatures and levels of humidity for environments where the air speeds are not greater than 40 ft/min (0.20 m/s).

From the viewpoint of a heat transfer analysis, radiation, convection and evaporation control heat loss from the human body. These three factors are determined by the mean radiant temperature, air temperature, humidity and air speed of a space. Humidity is normally controlled by the HVAC system for the entire area served by one air handler. Air velocity is maintained by the ventilation and air supply system in an individual room at the level needed to provide relatively uniform temperatures and avoid drafts. Air temperature and velocity determine the convection heat transfer rate between the human body and indoor air with heat loss proportional to the temperature difference. The mean radiant temperature (MRT) determines the radiation heat exchange between the human body and the surrounding surfaces. In a typical room, the air temperature, air speed and the MRT are the variables a design engineer can control (Palmer and Chapman 2000).

The MRT is defined as "the uniform temperature of an imaginary enclosure in which radiant heat transfer from the human body equals the radiant heat transfer in the actual non-uniform enclosure" (ASHRAE Handbook, 2005). The MRT can be calculated from the surface temperatures and the corresponding angle factors from the occupant and the surrounding surfaces by the following equation (ASHRAE Handbook, 2005):

$$T_r = \left[\sum_i F_{p-i} T_i^4 \right]^{\frac{1}{4}}$$

(4.1)

T_r is the mean radiant temperature; F_{p-i} is the angle factor between the person and the surface; and T_i is the surface temperature. The mean radiant temperature can also be determined by the discrete ordinate method (Degreef and Chapman 1997) using the following equation:

$$T_r = \left[\frac{\sum_j I^j A_P^j w^j}{A_{eff} \sigma} \right]^{\frac{1}{4}}$$

(4.2)

I^j is the intensity coming from a discrete direction; w^j is the quadrature weighting factor for the direction; A_p^j is the projected area in the given direction; and A_{eff} is the effective area of a person. When the temperature differences among the various surfaces in an enclosure are small, there is no significant difference in the results of these two equations.

Both the MRT and the room air temperature have a significant influence on thermal comfort, although they are not the only conditions influencing human thermal comfort. The operative temperature, which is a term combining air temperature and mean radiant temperature, was suggested by Fanger (1967) as a measure of local thermal comfort. Operative temperature is defined as "the uniform temperature of an imaginary black enclosure in which an occupant would exchange the same amount of heat by radiation plus convection as in the actual nonuniform space." According to ASHRAE Standard 55-2004, operative temperature can be calculated by the following equation:

$$T_{op} = AT_a + (1-A)T_r$$

(4.3)

The value of A is a function of relative air speed V_r and can be found using Table 4.1

Table 4.1. Value of A in Equation (4.3)

Air Speed Vr	<40 fpm (<0.2 m/s)	40 to 120 fpm (0.2 to 0.6 m/s)	120 to 200 fpm (0.6 to 1.0 m/s)
A	0.5	0.6	0.7

(Source: ANSI/ASHRAE Standard 55-2004)

When the air speed is small (less than 0.2m/s) or the difference between the mean radiant and the air temperature is small (less than 4˚C or 7˚F), the operative temperature can be approximated to be the mean of the average air temperature and the MRT.

When a space has a large area of window as shown in Figure 4.1, the temperature difference between the interior walls and the surface of the exterior window is large in winter. Convective heating systems sometimes encounter some difficulty in counteracting the discomfort caused by the cold window surface. Radiant heating is efficient in this situation to neutralize this deficiency and minimize radiation losses by the human body. This leads to the question of how the radiator should be located to achieve energy efficiency and improve the thermal comfort in the space.

This chapter analyzes the heating load and the operative temperature distribution in two cases. In Case 1, the radiators are located close to a large window. In Case 2, the radiator is located in the center of the ceiling. The heating energy consumption for these two cases is analyzed for different radiant and convective heating ratios. The thermal comfort distributions in these two cases are also analyzed by numerical methods.

4.2 Simulation Cases

Some people may have experienced discomfort when sitting close to a window or near sliding glass doors during the winter. To counteract this effect, panel radiators may be installed close to windows or on the ceiling. Two different radiator positions are studied in a typical office geometry. The office has the dimensions of 15 feet long, 10 feet wide and 8 feet high. Radiant heating combined with a central forced-air system is assumed to be the heating system. The configuration of this office is shown in Figures 4.1 and 4.2. The office is assumed to be in a "middle" floor of an office building. To simplify the calculation, we assume the ceiling, floor, back wall and sidewalls to be adiabatic. The entire exterior wall is assumed to be a double glazed window with an R value of 1.64 hr·ft^2·°F/Btu. This resistance value excludes the internal surface convective and radiation resistance, which will be evaluated separately later.

In Case 1, two 2x8 foot radiators are positioned, as shown, next to the window. In Case 2, one 4x8 foot radiator is positioned in the center of the ceiling. The outside temperature is presumed to be 30°F (-1.1°C) and the operative temperature is set to be 73°F (22.8°C). This chapter studies the impact of radiator position on heating consumption and thermal comfort for different ratios of radiant and convective heating in these two cases at outside air supply rates of 10cfm, 20cfm and 40cfm. The occupant-sensible load is 75W for one person. The lighting and equipment load is 160W.
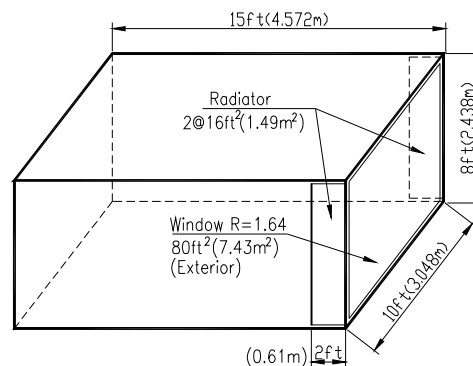
Figure 4.1 Geometry of an Office (Case 1)
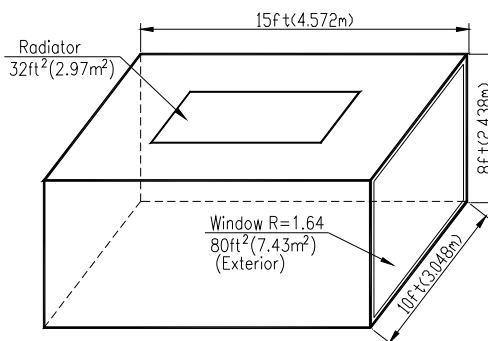
Figure 4.2 Geometry of an Office (Case 2)

4.3 Heat Transfer and Energy Model

The heat transfer at an internal surface in the enclosure shown in Figures 4.1 and 4.2 consists of irradiation from other surfaces, emissions to other surfaces, convection between the surface and the inside air, and conduction loss to the outside. For all adiabatic surfaces, the conduction

term vanishes. The window is the only component where heat can be conducted outside. Heat is supplied to the radiator by hot water and can be seen as a generation term, with units of Btu/ft^2.

The heat balance on the occupants includes irradiation from and emission to each surface in the enclosure, convection loss to the inside air, and heat generation from the human body. The heat balance can be illustrated as shown in Figure 4.3. The energy equation for a control surface can be written as:

$$\nabla \bullet (k\nabla T_s) + h_c(T_a - T_s) + \dot{q}'' + \dot{q}_r = \rho c_p \frac{\partial T}{\partial t} \tag{4.4}$$
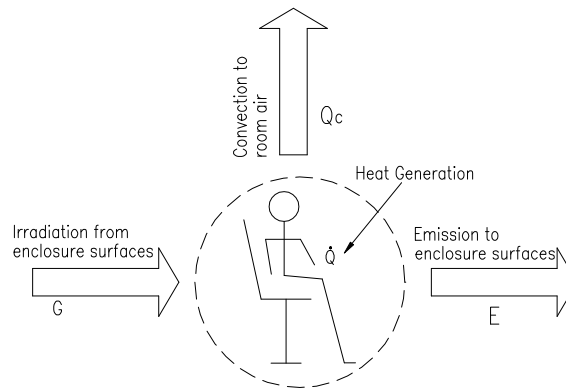
Figure 4.3 Energy Balance on Occupant

In Equation (4.4), h_c is the surface convection coefficient which is a temperature dependent variable. Each surface has a different h_c. This will be discussed later. $\dot{q}_r$ can be written as follows:

$$\dot{q}_r = -\sum_i F_{s-i}\varepsilon\sigma\left(T_s^4 - T_i^4\right) \tag{4.5}$$

F_{s-i} is the view factor from surface s to surface i. At a steady state, Equation (4.4) can be simplified as:

$$\frac{T_o - T_s}{R_s} + h_c(T_a - T_s) + \dot{q}'' + \sum_i F_{s-i}\varepsilon\sigma(T_i^4 - T_s^4) = 0 \tag{4.6}$$

In the simulated cases, all walls are adiabatic except for the window. Therefore, the energy balance for the entire space can be written as:

$$\dot{q}_{radiator} + \dot{q}_{air} + \dot{q}_{gain} - \dot{m}_{fa}c_p(T_a - T_o) - \dot{m}_{vent}c_p(T_a - T_{vent}) - \frac{T_{win} - T_o}{R_{win}} = 0 \tag{4.7a}$$

The term $\dot{q}_{gain}$ represents the internal heat gain, which includes the heat gain from occupants, lighting and equipment load. The term $\dot{m}_{fa}c_p(T_a-T_o)$ is the classic term used to approximate the heat needed to increase the temperature of the infiltration air from the outside temperature T_o to the inside air temperature T_a. T_{vent} is the ventilation air temperature and is considered to be T_0. For the remainder of this chapter, we will assume that infiltration air is included in the ventilation air, $\dot{m}_{vent}$. Therefore, the relevant form for the energy balance equation becomes:

$$\dot{q}_{radiator}+\dot{q}_{air}+\dot{q}_{gain}=\dot{m}_{vent}c_p(T_a-T_o)+\frac{T_{win}-T_o}{R_{win}} \qquad (4.7b)$$

If we assume all interior walls are adiabatic and the temperature of each surface is uniform, the energy balance equation for each surface can be expressed as follows by simplifying Equation (4.6).

For radiator surface temperature T_p:

$$h_{c-p}(T_a-T_p)+\dot{q}''+\sum_i F_{p-i}\varepsilon\sigma(T_i^4-T_p^4)=0 \qquad (4.8)$$

For window surface temperature T_{win}:

$$\frac{T_o-T_{win}}{R_{win}}+h_{c-win}(T_a-T_{win})+\sum_i F_{win-i}\varepsilon\sigma(T_i^4-T_{win}^4)=0 \qquad (4.9)$$

Equations for side wall temperature T_{w1}, back wall temperature T_{w2}, floor temperature T_{w3}, and ceiling temperature T_{w4} can be generalized as follows (all four equations have the same form).

$$h_{c-wj}(T_a-T_{wj})+\sum_j F_{wj-i}\varepsilon\sigma(T_i^4-T_{wj}^4)=0 \qquad (4.10)$$

Because of symmetry, the two side walls can be assumed to have the same temperature. Therefore, a total of six equations can be obtained. If the inside air temperature T_a and radiation heating value $\dot{q}''$ is given, then theoretically, the six surface temperatures can be solved. However, these equations are nonlinear and convection coefficient h_c also depends upon the temperature difference between the surface and the room air. To simplify these equations, the radiation term can be approximated as (Mills, 1999):

$$\dot{q}_r=\sum_i F_{s-i}\varepsilon\sigma\left(T_i^4-T_s^4\right)=\sum_i F_{s-i}h_{ri}(T_i-T_s) \qquad (4.11)$$

$$h_{ri} = 4\varepsilon\sigma T_{mi}^3 \qquad (4.12)$$

$$T_{mi} = \frac{T_i + T_s}{2} \qquad (4.13)$$

Mills (1999) has shown that when the temperature difference is less than 100K, the error of this approximation is less than 2%. When the temperature difference is less than 10K, the error is less than 0.03%. Equations (3.8), (3.9) and (3.10) can be simplified into six linear equations, as follows:

$$h_{c-p}(T_a - T_p) + \dot{q}'' + \sum_i F_{p-i} h_{rp}(T_i - T_p) = 0 \qquad (4.14)$$

$$\frac{T_o - T_{win}}{R_{win}} + h_{c-win}(T_a - T_{win}) + \sum_i F_{win-i} h_{rwin}(T_i - T_{win}) = 0 \qquad (4.15)$$

$$h_{c-wj}(T_a - T_{wj}) + \sum_j F_{wj-i} h_{rwj}(T_i - T_{wj}) = 0 \qquad (4.16)$$

The convection heat transfer coefficient h_c is not easy to establish. In most of the previous related research, a constant coefficient is used for all vertical walls. This over-simplified method may give inaccurate results. The convection intensity between a cold window pane and the inside air is quite different from the convection between warm interior walls and the inside air. Natural convection at the interior walls and windows falls within the range of the turbulent flow, according to the laminar flow criterion, $L^3\Delta T < 63$ (US units) (2002). Min et al. (1956) studied the natural convection in a panel-heated room. The equations determined by Min and proposed by ASHRAE (2005) are (US units):

For a heated or cooled wall:

$$h_c = 0.26(T_s - T_a)^{0.32} \qquad (4.17)$$

For a partially heated ceiling:

$$h_c = 0.13(T_s - T_a)^{0.25} \qquad (4.18)$$

For a heated floor or cooled ceiling:

$$h_c = 0.31(T_s - T_a)^{0.31} \qquad (4.19)$$

For a heated ceiling:

$$h_c = 0.02(T_s - T_a)^{0.25} \qquad (4.20)$$

Based on Equations (4.17) – (4.20), the convection coefficient needed for Equations (4.14), (4.15), and (4.16) can be determined. In the computation program, initial guessed values are

given to all h_c and h_r. Then the matrix of these six equations can be solved. The surface temperatures obtained are then submitted into the coefficient calculation and the matrix is re-solved until the results converge.

4.4 Simulation Results

The objective of the simulation is to obtain the surface temperatures and analyze the heating load at different radiator positions. Once the surface temperatures of the enclosure are known, the heating load of the entire space can be easily found by using Equation (4.7a). The heating load must be compared on the basis of the same comfort level for the two cases. The operative temperature is used as a comfort indicator. In the simulations performed for this chapter, the operative temperature in the space is set at a constant value. The mean radiant temperature in the center of the space can be calculated by Equation (4.1). However, the value obtained by this equation only reflects the MRT at a certain point. The weighted surface temperature may better represent the average MRT inside an enclosure. The following equation is used to calculate the mean radiant temperature in the space:

$$T_r = \left(\frac{\sum\limits_i A_i T_{si}^{\ 4}}{A_{total}} \right)^{\frac{1}{4}}$$

(4.21)

T_{si} is the individual surface temperature. The air temperature is assumed uniform and determined from Equation (4.3), assuming that the air speed is less than 40fpm, so A=0.5, resulting in the following equation:

$$T_a = 2T_{op} - T_r$$

(4.22)

Based on the heat transfer model described above, a simulation program has been written and the calculation flow chart is illustrated in Figure 4.4.
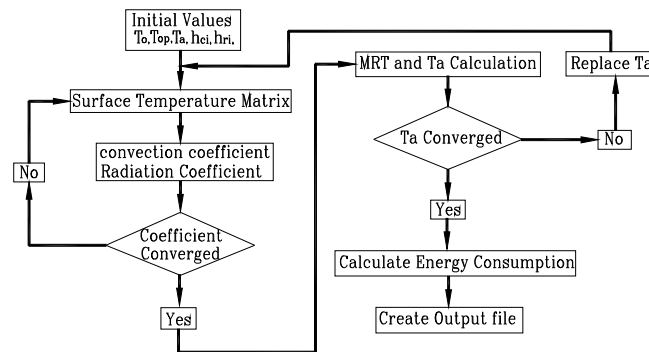
Figure 4.4 Calculation Flow Chart

By setting the outside temperature to be 30°F (-1.1^{o}C), the operative temperature to be 73°F, and the ventilation rate to 20CFM, the simulation results can be shown in Figures 4.5 and 4.6.

4.4.1 Case 1: Two 16 ft^2 Radiators Next to a Window

By increasing the radiant heating ratio and keeping the operative temperature constant at 73°F (22.78^{o}C), the surface temperature, air temperature and mean radiant temperature trends are all shown in Figure 4.5. From left to right, the radiant heating ratio increases from 0 to 1. Simultaneously, the convective heating ratio decreases from 1 to 0. At 100% convective heating on the left hand side, the window surface temperature is measured at about 61.0^{o}F (16.1^{o}C). This temperature gradually increases to 62.7^{o}F (17.1 ^{o}C), when the radiant heating increases to 100%. From Figure 4.5, it can be seen that the slope of the window surface temperature is larger than that of the back wall temperature. Because the radiators are much closer to the window than the back wall, the radiator surface temperatures have a greater influence on the window surface temperature. The increased window surface temperature increases the comfort level for an occupant who is seated near the window. However, the increased surface temperature also raises the temperature difference between the inside surface and the outside environment. The higher temperature difference will result in a higher level of heat loss through the window which may cause the overall heating consumption of the space to rise.

As shown in Figure 4.5, when the heating system switches from 100% convective to 100% radiant heating (from left to right), the room air temperature can be reduced from 76.6^{o}F (24.8^{o}C) to 72.8 ^{o}F (22.6^{o}C), a 4.0^{o}F (2.2^{o}C) difference. The lower room air temperature reduces the energy used to heat the ventilation air. This is one of the advantages of radiant heating. The

mean radiant temperature increases from 69.4^{o}F (20.7 ^{o}C) to 73.2 ^{o}F(22.9 ^{o}C), when the enclosure is heated by 100% radiant heating.

4.4.2 One 32 ft^{2} Radiator Located in the Center of the Ceiling

Figure 4.6 shows the temperature trends when the radiator is located in the center of the ceiling and the radiant heating ratio increases from 0% to 100%. As compared to Figure 4.5, the mean radiant and room air temperatures demonstrate the same trend. The room air temperature is reduced from 75.6^{o}F (24.2^{o}C) to 71.4^{o}F (21.8^{o}C), a 4.2^{o}F (2.3^{o}C) reduction, as the radiant heating increases to 100%. The most significant difference between Figures 4.5 and 4.6 is the slope of the window surface temperature as the radiant heating ratio changes. The slope of the window surface temperature is flatter in Figure 4.6. The increase in the window surface temperature is less than 1°F when the space switches from 100% convective heating to 100% radiant heating. The lower window surface temperature reduces the heat loss from the window, as compared with Case 1. However, it may reduce the comfort level near the window. The room air temperature reduction is larger in Case 2 than in Case 1, which saves more energy.
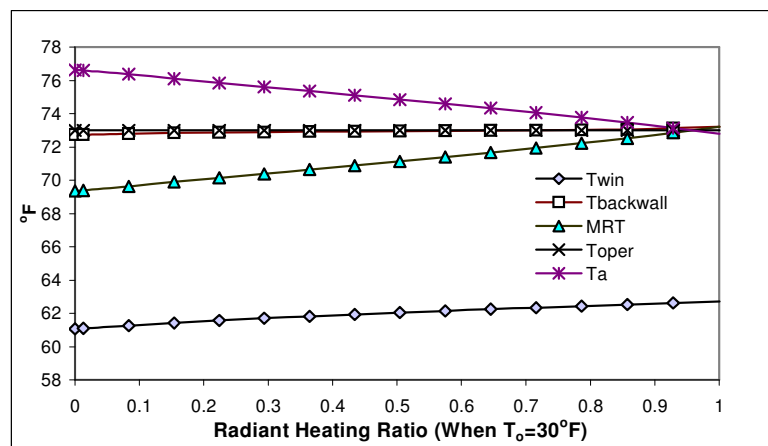
Figure 4.5 Temperature Trends at Different Radiant Heating Ratios for Case 1
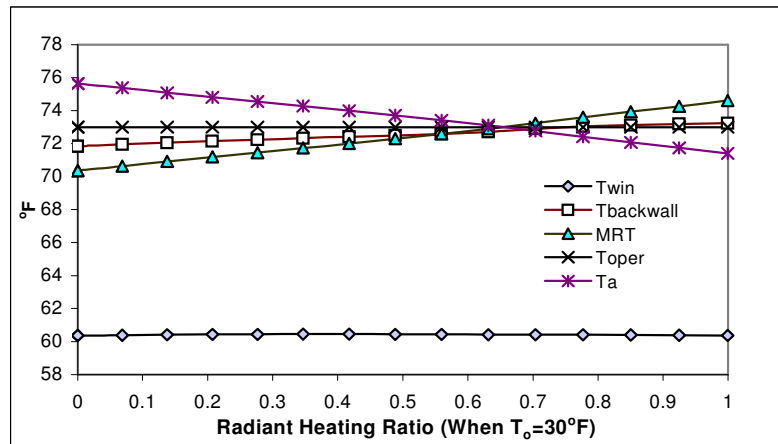
Figure 4.6 Temperature Trends at Different Radiant Heating Ratios for Case 2

The above observation is based on an outside air flow of 20cfm. When the outside air flow is changed, the temperature trends of window surface, MRT and room air temperatures are almost the same. The starting and ending points of the trend lines are slightly different.

4.5 Heating Load Comparison

In the two cases analyzed above, two factors affect the heating load: room air temperature and window surface temperature. When radiant heating increases, the reduced room air temperature helps to decrease the heating load. On the other hand, the increased window surface temperature adds to energy use. Figure 4.7 shows the total heating load for these two cases. In Case 1, the heating load increases about 2.5% for 100% of the radiant heating, as compared with 100% of the convective heating. In Case 2 the heating load decreases about 1.8%. It shows that the position of the radiator(s) in a typical office has some impact on the heating load, but the impact is small. This observation is based on an outside air supply of 10CFM, which is equivalent to 0.5 ACH of the infiltration rate. This is the night time operation condition, in which the mechanical ventilation stops and natural infiltration is the only source of outside air.

As the amount of outside air increases, the energy used to heat the ventilation air also increases [see Equation (4.7a)]

This increases the relative importance of changes in room air temperature relative to changes in window surface temperature. We illustrate this concept by considering two higher ventilation rates for one and two occupants in the daytime.

Figure 4.8 shows the heating load of the two cases when the outside air supply rate equals 20cfm, which is the fresh air requirement for one occupant in this office, according to ASHRAE Standard 62-2001. For Case 1, the heating load by 100% radiant heating is close to that of 100% convective heating. When the ratio of radiant heating goes up, the heating load first rises and then decreases. This occurs since the term, $\dot{m}_{vent} c_p T_a + \dfrac{T_{win}}{R_{win}}$, from Equation (4.7a), first increases in size, then decreases as the radiant heating ratio increases. This causes the total heating consumption to increase slightly and then go down. For Case 2, it can be seen that the ventilation heating always decreases faster than the window heating increases, and 100% radiant heating can reduce heating by about 3.7%.

If the simulated space (150 ft^2) is occupied by two employees, the outside air requirement would be 40cfm, according to ASHRAE Standard 62-2001. The heating load shown in Figure 4.9 applies when the heating system is switched from convective to radiant heating. It can be seen that the heating load declines about 3.6% for Case 1 and 7.6% for Case 2. Figures 4.7, 4.8 and 4.9 illustrate that the outside air supply rate has an important effect on the energy savings provided by radiant heating. In a real situation, the outside ventilation air is normally preheated to about 55°F before it is supplied to the conditioned space. The maximum radiant heating ratio in this case is less than 100% because of the preheating of the ventilation air, which provides a correspondingly smaller level of heating savings.
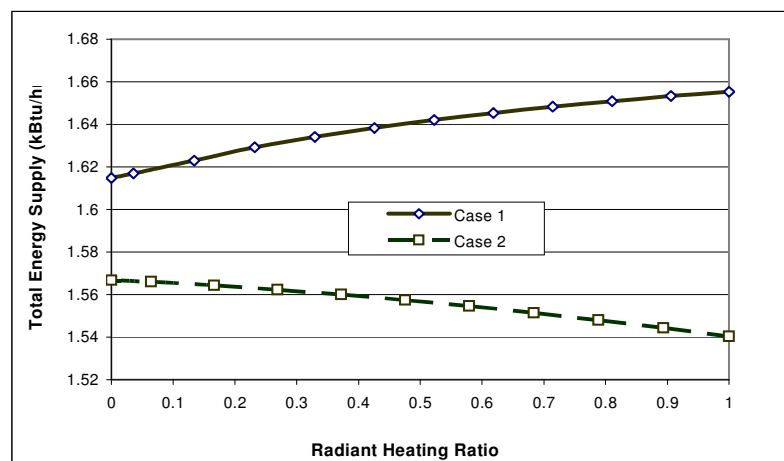
Figure 4.7 Heating Load at Different Radiant Heating Ratios (OA=10cfm)
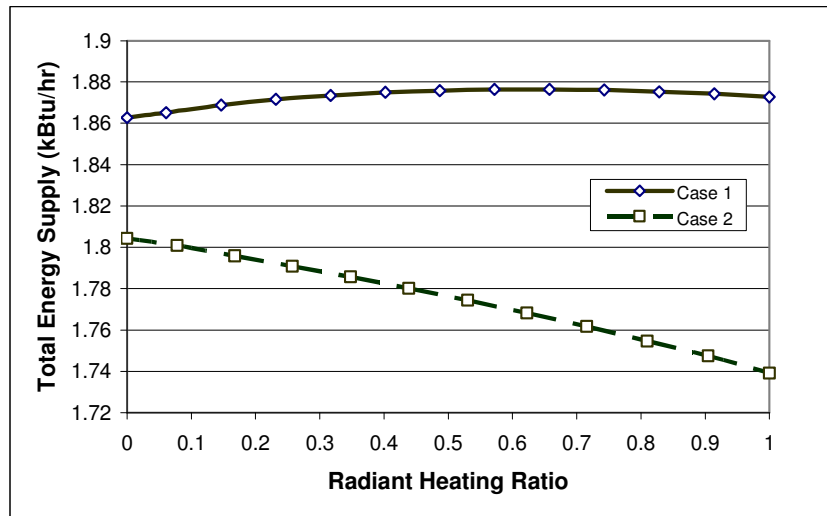
Figure 4.8 Heating Load at Different Radiant Heating Ratios (OA=20cfm)
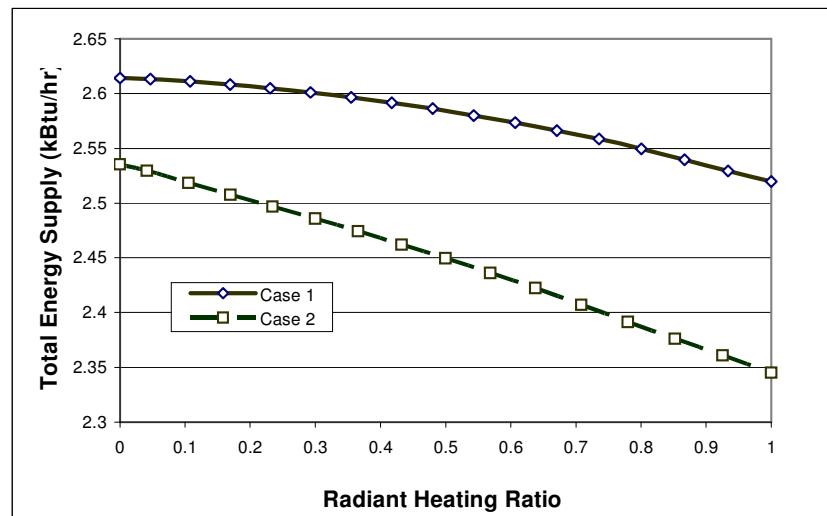
Figure 4.9 Heating Load at Different Radiant Heating Ratios (OA=40cfm)
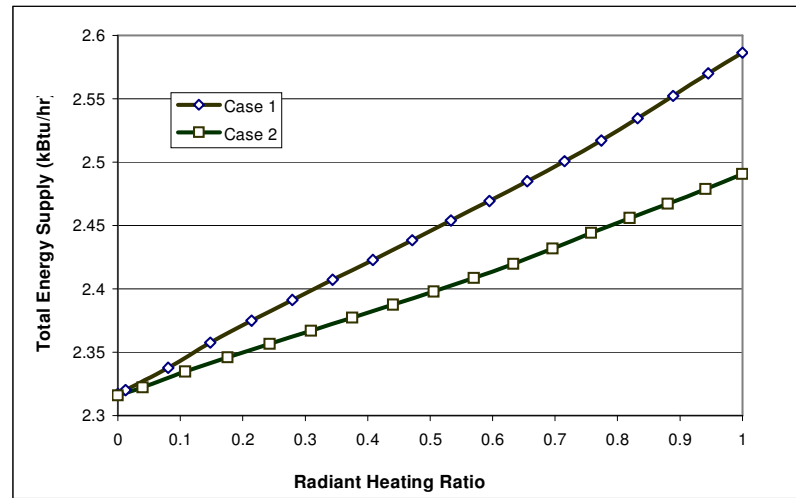
Figure 4.10 Heating Load at Different Radiant Heating Ratios (OA=40cfm, T_{air}=73˚F)

The above observation is based on keeping the operative temperature constant in order to keep a constant comfort level. In a real radiant heating application, the heating load of a radiantly heated space also depends upon the type and location of the thermostats. If an operative temperature thermostat is used, only a small energy savings can be expected. If a dry bulb temperature thermostat is used and the set point is kept the same as for air heating, the heating load will increase for the cases examined. Figure 4.10 shows the heating load trends at different radiant heating ratios, if the room air temperature is kept constant. Figure 4.10 indicates that, for Case 1 at a 40CFM ventilation rate, the heating load increases about 11.5% when the space switches from 100% convective heating to 100% radiant heating. For Case 2 at a 40CFM ventilation rate, the heating load increases about 7.7%. The above observation is based on keeping the room air temperature constant at 73˚F. For lower ventilation rates, the heating requirement will increase by the same amount, but the percent will be different since the total heating requirements will decrease.

4.6 Thermal Comfort Distribution

In the theoretical analysis section of this chapter, the area weighted surface temperature is considered to be the average room radiant temperature. The operative temperature is kept at a constant value. However, the mean radiant temperature actually varies with the location within the enclosure. When the occupant is close to the radiator, he/she may feel warmer. When the

occupant is far from the radiator, he/she may feel cooler. The thermal comfort in the two cases is not uniform. A numerical method, as implemented in a popular computational fluid dynamics program (FLUENT6.2, Fluent Inc.), was used to calculate the mean radiant temperature, room air temperature, and operative temperature in the three dimensional space using 100% radiant heating. The results at 4 ft (1.22 m) above the floor are shown in Figures 4.11 and 4.12.

The heat fluxes obtained from the theoretical calculation were used as the boundary conditions for radiators in the numerical analysis. Floor, ceiling, and walls were all simulated as adiabatic surfaces with an emissivity of 0.9. The window was simulated as an opaque surface with an emissivity of 0.9. The discrete ordinate model was selected for radiation intensity calculation. This model has been evaluated by Truelove (1987), and by Chapman and Zhang (1995), and has been shown to provide quite accurate results. The Grashof numbers for windows and walls fall within the range of 1.3e14 to 1.3e15, which means that all of the surfaces have a turbulent boundary layer. Therefore, the $K - \varepsilon$ turbulence model was selected for the natural convection calculation. Nielson (1998) compared four turbulence models for the prediction of room airflow and showed that the $K - \varepsilon$ model was quite accurate for general application.

In Figure 4.11, the room air temperature is 0.5K higher close to the radiator. In the remaining area, the room air temperature is almost uniform. There is a very thin layer close to the window where the air temperature is near 60°F (288.5K). The effect of the cold window and the hot radiator surfaces can be seen clearly in the mean radiant temperature distribution. Close to the radiators, the radiant temperature gradient is much higher, and the MRT becomes higher. On the other hand, the MRT becomes lower and the negative mean radiant temperature gradient becomes larger when close to the window, as in Case 1. The operative temperature is around 73°F (296K), except for small areas near the radiators and the window. The natural convection is created by the temperature difference between the air and the window inside surface. The down draft is normally caused by this natural convection in a radiantly heated space. This arrangement has the benefit of reducing the down draft effects near the window. When the radiators are close to the window, they heat up the nearby air and the air flows up in an inverse direction to the down draft air. Therefore, the downdraft is greatly reduced in window area.
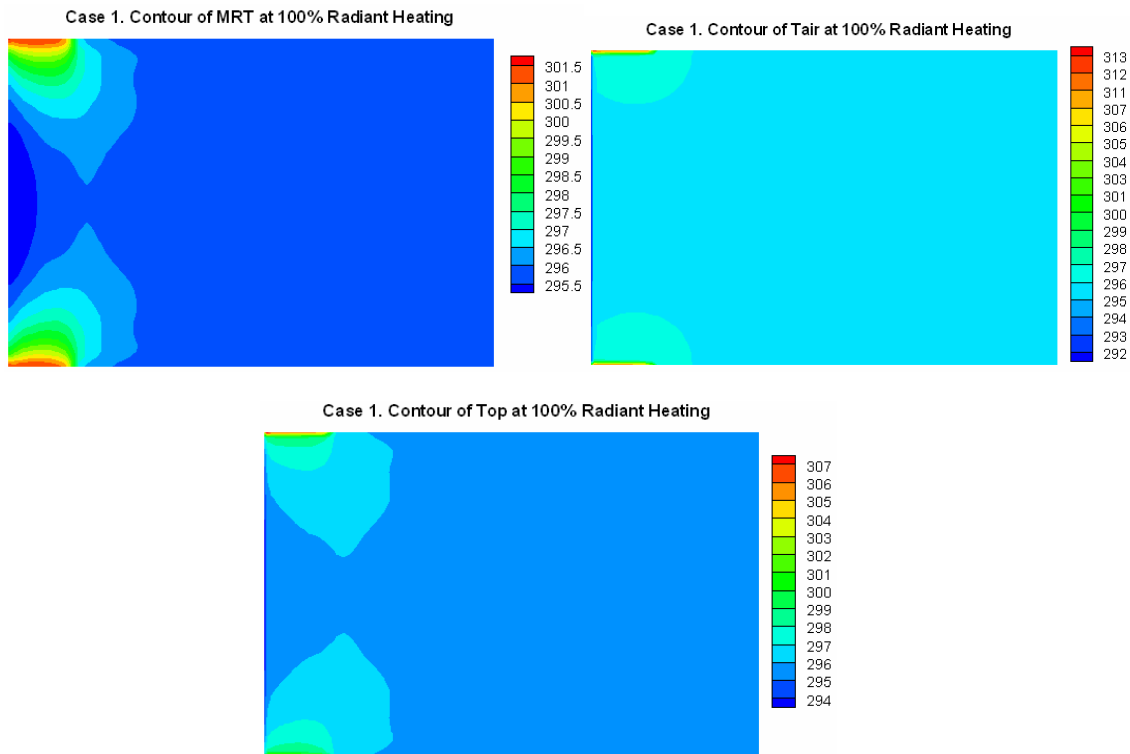
Figure 4.11 Temperature Distribution (K) of MRT, T$_{air}$, and T$_{op}$ for 100% Radiant Heating, Case 1, 4 ft Level (Window is at the Left Side of the Space)

In Figure 4.12, the room air temperature is very even, but the mean radiant temperature has a larger gradient. The MRT increases from 64°F (291K, 18˚C) close to the window to 81°F (300K, 27˚C) close to the center of the radiator, then decreases to 77°F (298K, 25˚C) at the back wall. The radiant temperature in one half of the room is clearly higher than in the other half. The operative temperature shows that thermal comfort is distributed unevenly. One third of the room is lower than 73°F (296K, 23˚C). Furthermore, the down draft effect may be obvious because there are no measurements to control the natural convection near the window. Figure 4.11 shows that the thermal comfort is more uniform in Case 1 than in Case 2. This demonstrates that the radiators near the window prevent cold penetration inside the space and enhance comfort, although this layout uses slightly more energy.
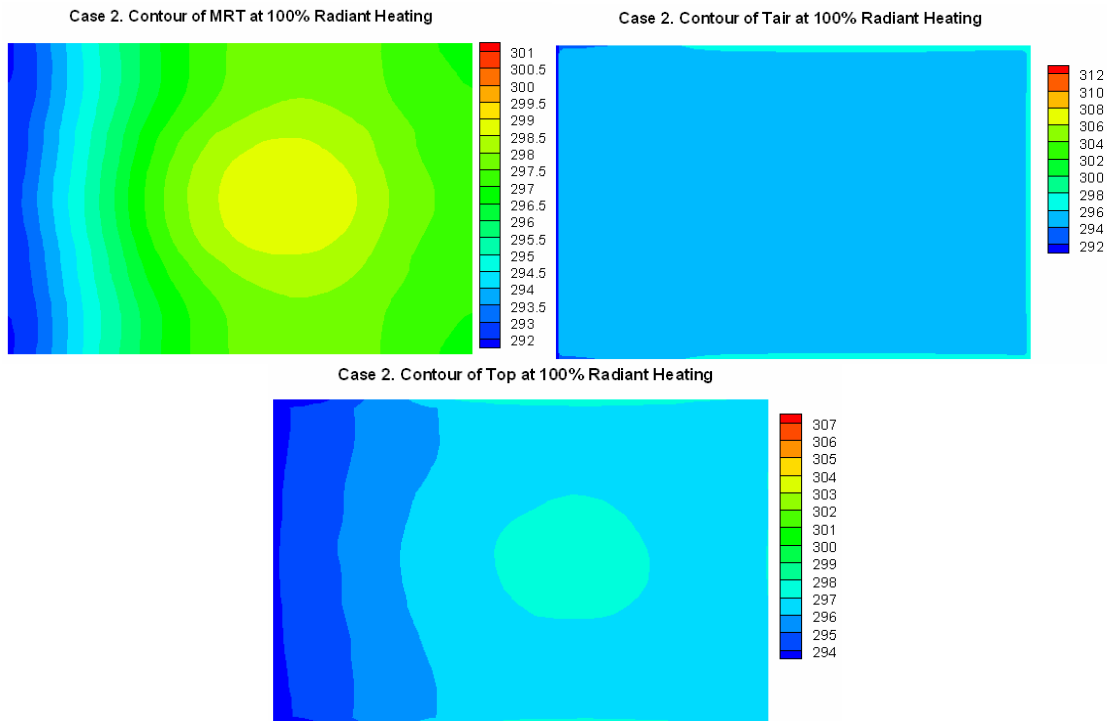
Figure 4.12 Temperature Distribution (K) of MRT, T_{air}, and T_{op} for 100% Radiant Heating, Case 2, 4 ft Level

4.7 Summary

The position of the radiation source(s) in a radiantly heated office with a double-glazed window acting as the exterior wall has been shown to impact both the heating load and the thermal comfort distribution inside the room. When radiators are close to the window (Case 1), the increase of window surface temperature is higher than when the radiator is located in the center of the ceiling (Case 2). The layout of Case 1 increases the heating load at an outside temperature of 30°F by 2.5% in an unoccupied space. When the radiator is located in the center of the ceiling, the window surface temperature increase is very small. This layout uses 1.8% to 7.6% less heating energy than convective heating for the three ventilation rates analyzed, as shown in Table 4.2. The energy savings relative to the convective system depend on the outside air supply rate. When the outside air supply rate is larger than 20cfm, both layouts slightly reduce their heating requirements, as compared to the air heating system. The heating load analysis in this chapter does not include possible fan power savings offered by the radiant heating system.

Table 4.2. Energy Savings of Radiant Heating vs. Convective Heating for Cases Analyzed

OA	Case 1	Case 2
10 CFM	-2.5%	1.8%
20 CFM	-0.5%	3.7%
40 CFM	3.6%	7.6%

The control device used also affects the energy consumption of a radiant heating system. If a dry bulb temperature thermostat is used in a radiantly heated space and the temperature is set at the same point as for air heating, the radiant heating will increase the heating load for those cases considered here. At the 40cfm ventilation rate, the heating loads of Layouts 1 and 2 increase approximately 11.5% and 7.7%, respectively, when the office temperature is set to be constant at the value used for air heating.

On the basis of thermal comfort, radiators located close to the window can reduce the down draft, prevent cold penetration inside a room and make the operative temperature distribution much more uniform than when the radiator is located in the center of the ceiling. This means that radiators close to the window improve the thermal comfort level inside a room although they will cause the heating load to increase slightly relative to ceiling radiators.

CHAPTER V

THE INDOOR HUMIDITY ANALYSIS OF AN INTEGRATED RADIANT
COOLING AND DESICCANT VENTILATION SYSTEM

5.1 Introduction

Chapter IV studied the functions of different radiators in the heating condition. This chapter will study the operation of the radiant system in the cooling condition. Radiant cooling panels cool the surrounding air by convection and cool objects within their direct view by radiation. In a radiant cooling system, the chilled water supply temperature can be increased by more than 10ºF, as compared to that required by the cooling coil in an air handler. This will significantly reduce the chiller electricity consumption. The radiant cooling system can also save energy by cutting the supply fan power. Stetiu (1999) simulated a radiant cooling system in a 700 square meter building and reported a 30% energy savings, as compared to an all air system. Niu et al. (2002) compared a chilled ceiling combined with a desiccant cooling system with a conventional constant volume all air system and reported 44% primary energy savings in hot and humid climates such as Hong Kong.

However, condensation is a major problem that restricts the application of radiant cooling. Because radiant cooling systems lack the capability to remove moisture, and thus ventilation is required, a radiant cooling system must be used in conjunction with a dedicated outside air system. The dedicated outside air system can be a 100% outside air AHU or a desiccant wheel combined with a chilled water coil.

Several studies have examined the moisture condensation problem in radiantly cooled offices. Mumma (2001c, 2002, 2003, 2005) explored the condensation issues related to chilled ceilings combined with a dedicated outside air system. He studied the mechanisms of water formation on chilled panels when occupants in the space exceeded the design, and investigated the consequent necessary control measures. Zhang et al. (2003) studied the indoor relative humidity behavior of all air systems with total heat recovery, chilled ceilings with an AHU, and chilled ceilings with desiccant cooling. They reported that a system combining a chilled ceiling with air dehumidification offers more annual hours in the comfort region than with other ventilation systems. They concluded that condensation can be avoided if the AHU ventilation unit begins operating one hour earlier than the chilled ceiling. One aspect that has received little

attention in previous research is the impact of infiltration on condensation in a space where radiant cooling is integrated with a desiccant ventilation unit.

In the design of a radiant cooling system, the capacity of the ventilation system is decided by either the space latent load or the indoor fresh air requirement, whichever is larger. When the latent load fluctuates widely such as in a meeting room or a classroom, the design value of the ventilation air flow often needs to be very large in order to meet peak conditions. In these cases, the radiant cooling can only meet 10% to 30% of the space cooling load, which substantially reduces the energy savings that could be obtained from radiant cooling. How does the ventilation rate affect the indoor humidity and moisture condensation on chilled panels? This is another question that has not received enough attention in previous studies.

This chapter studies the hourly absolute humidity ratio in the IW with an integrated passive desiccant ventilation system. It illustrates the interaction between infiltration and mechanical ventilation rates on the indoor humidity level, and the condensation and energy consumption of a radiantly cooled space. The possibility of condensation on the surface of radiant panels under different operation conditions and the space load distribution between ventilation systems and radiant cooling system have been investigated. Operating strategies to control condensation are recommended.

5.2 Simulation Case Study

The Intelligent Workplace is a small university office area that includes faculty, graduate student and staff offices and a meeting room with an area of 580m^2 (6228 ft^2). The air conditioning system was a radiant heating and cooling system combined with a passive desiccant ventilation unit before 2006. A group of sensible fan coil units is scheduled to be installed in the north zone in the winter of 2006. The space uses two types of radiant panels which are modeled and discussed in Chapters II and III. The mullion system is used to offset the heating and cooling load from the windows and to increase the indoor comfort levels. Another function of the mullion system is that grouped mullions can provide flexible heating and cooling set points based on the preference of the occupants. The second radiant system is overhead ceiling panels, which are used for spaces away from the windows. The chilled water and hot water are switched in the same piping system between summer and winter via a two-pipe system, as shown in Figure 2.1.

The exterior walls of the IW are metal with 4-inch insulation inside, providing an R-value of 20 ft^2-hr-^{o}F/Btu. The double pane windows account for 58.3% of the area of the exterior wall. The open trussed sloped roof has the same thermal resistance as the metal wall. The roof includes 648 ft^2 of skylights, which have the same R-value as the windows. Moveable shades are installed on all the skylights. Because of the large window area, the lighting load in the space is relatively small, 0.9W/ft^2. The average equipment load is 0.3 W/ft^2. 32 people are assumed to be the normal level of maximum occupants. A sensible load of 230 Btu/hr per person is assumed with a latent load of 0.13lb/hr-person.

This chapter assumes that radiant panels are the only available heating and cooling devices in the IW. The space is simulated using DOE2.1 software. The simulation model is carefully calibrated according to the procedures of Claridge et al. (2003) until the calibrated simulation model closely matches the measured consumption data. Then the calibrated model is used to predict the system load at different infiltration and ventilation conditions.

5.3 Desiccant Ventilation System

To increase energy efficiency, a radiant cooling system is typically integrated with a solid desiccant ventilation system, which can be either a passive system or an active system. The most commonly used desiccant systems are single wheel passive desiccant systems or dual wheel active desiccant systems. The desiccant wheel absorbs moisture from the fresh outside air and the wheel is regenerated with either hotter or dryer air. A passive desiccant wheel uses dry air, which is usually the building's exhaust air. An active desiccant wheel uses heated air produced by gas combustion or a heating coil. Active desiccant wheels can deeply dry the fresh outside air in all weather conditions regardless of the moisture content of the exhaust air. However, an active wheel requires heat input to dry the air, which increases the system energy consumption. A passive desiccant wheel cannot remove as much moisture as an active desiccant wheel. The moisture level of the supply air leaving the passive desiccant wheel depends upon the dryness of the exhaust air and its flow rate. Cooling is required after the passive wheel (henceforth called "post cooling") in order to remove additional moisture and to maintain a sufficiently low humidity level sufficiently low inside the space when integrated with the radiant cooling. Exhaust air reactivates the desiccant in a passive wheel adiabatically without additional heat input. The operating cost of a passive wheel is considerably lower than that of an active wheel, according to Harriman et al. (1999).

5.3.1 Passive Desiccant System

Available commercial passive desiccant systems, as shown in Figure 5.1 include single enthalpy wheel systems and duel wheel systems (which includes an enthalpy wheel plus a sensible wheel). The enthalpy wheel removes both the latent load and the sensible load, while the sensible wheel removes only the sensible load. The structure of these two wheels is similar. The key component is the "honeycomb like" transfer core, which utilizes an aluminum substrate. A commercial enthalpy wheel is normally coated with desiccant materials such as a 3Å or 4Å molecular sieve or a silica gel. The sensible wheel is a rotating heat exchanger without any desiccant coating.

Commonly used desiccant materials in HVAC applications are silica gel and molecular sieves. Silica gel can absorb up to 40% of its own weight in water. A typical value for its specific microporic surface area is ~600 m^2/g (Babus'Haq et al., 1996). The adsorption characteristics of silica gel function over a wide range of relative humidities. Molecular sieves are crystalline metal alumino-silicates (basically, ceramic materials). The most commonly used molecular sieve for air dehumidification is known as a type A zeolite. Zeolite can absorb water up to 20% of its own weight. Molecular sieves are porous crystals with large specific surface areas and uniform pore sizes, which have a specific microporic surface area of ~700m^2/g (Babus'Haq et al., 1996). A molecular sieve is usually used for low-temperature applications. A special property of molecular sieves is their ability to "selectively adsorb" materials based on their kinetic diameter, pulling in materials smaller than the size of their pore openings while excluding materials that are larger. This property can help reduce the contaminants carried over from the exhaust air to the supply air.
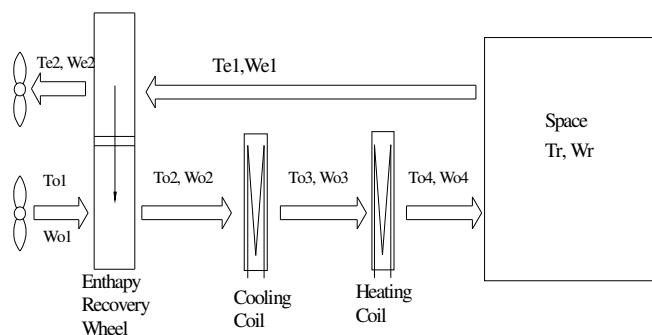
Figure 5.1 Passive Desiccant System

Enthalpy wheels normally use an aluminum substrate coated with a molecular sieve material or silica gel. The effectiveness of an enthalpy wheel depends upon the load of the desiccant materials, the diameter and depth of the wheel, the face flow velocity, the rotational speed and other operating conditions. Bulk et al. (1985) proposed $\varepsilon - NTU$ correlations for the design calculation of both the latent and total effectiveness of enthalpy wheels coated with silica gel. Simonson et al. (1999a, 1999b) developed a more accurate complex correlations for the sensible, latent and total effectiveness of enthalpy wheels. Their model works well on balanced flow silica gel and molecular sieve enthalpy wheels. Simonson et al. (2000) modified the above correlations to make them apply to unbalanced flow. Freund et al. (2003) developed a simple and generalized method to predict enthalpy wheel performance based on the classical $\varepsilon - NTU$ approach. Jeong and Mumma (2005) proposed a group of correlations to calculate the sensible, latent and total effectiveness of enthalpy wheels at non-standard conditions, based on statistical methods.

At design rotational speed and face velocity, latent heat transfer effectiveness, ε_L, and sensible heat transfer effectiveness, ε_S, can be found in the manufacturers' manuals. The parameters of supply and exhaust air can be calculated according to the following equations based on energy and mass balance, once the effectiveness and inlet conditions on both sides of the wheel are known.

$$T_{o2} = T_{o1} - \varepsilon_s \frac{(\dot{m}C_p)_{\min}}{(\dot{m}C_p)_s}(T_{o1} - T_{e1}) \tag{5.1}$$

$$w_{o2} = w_{o1} - \varepsilon_l \frac{\dot{m}_{\min}}{\dot{m}_o}(w_{o1} - w_{e1}) \tag{5.2}$$

$$T_{e2} = T_{e1} - \varepsilon_s \frac{(\dot{m}C_p)_{\min}}{(\dot{m}C_p)_e}(T_{o1} - T_{e1}) \tag{5.3}$$

$$w_{e2} = w_{e1} - \varepsilon_l \frac{\dot{m}_{\min}}{\dot{m}_e}(w_{o1} - w_{e1}) \tag{5.4}$$

5.3.2 Active Desiccant System

An active desiccant wheel is made up of fiberglass, paper, or sometimes aluminum substrate coated with silica gel. The most common active ventilation system is shown schematically in Figure 5.2. It is a combination of one desiccant wheel and one sensible energy wheel. The regeneration air can be provided by exhaust air or outside air. The supplied outside air first

passes through the desiccant wheel where the outside air (OA) is dried and the temperature increases. Then the OA passes through the sensible wheel, where it is cooled. Finally, the OA is cooled further by the cooling coil and its temperature is adjusted to the required temperature. The exhaust air first passes through the evaporative cooler and the sensible energy wheel to cool the supply air. After passing through the sensible wheel, part of the exhaust air is heated by the heating coil or by a natural gas burner to 150°F-225 °F and used to regenerate the desiccant wheel. The other part of the exhaust air is discharged into the ambient air. In a typical configuration, 75% of the desiccant wheel face area is in the fresh outside air path, while the remaining 25% is in the regeneration air path.
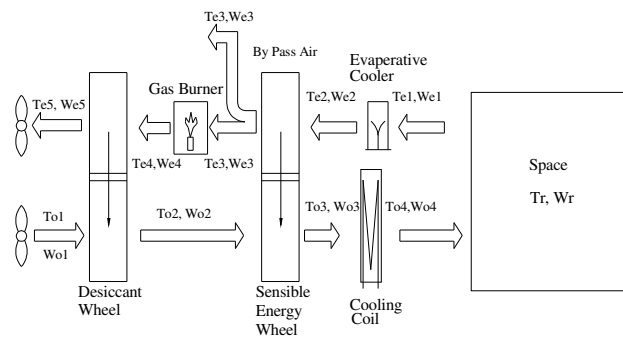
Figure 5.2. Active Desiccant System

The effectiveness of an active desiccant wheel depends upon both structural parameters and operating conditions such as the depth of the wheel, the type and quantity of the desiccant, the surface area of the honeycomb, and the temperature and humidity ratio of the outside air and regeneration air, the wheel rotational speed, the face flow velocity, etc. Adjusting the regeneration temperature is the approach most commonly used by commercial manufacturers to change the wheel's moisture removal capacity. The higher the regeneration air temperature, the more moisture removed by the desiccant wheel. When moisture is removed from the desiccant wheel, the latent heat of the moisture is converted to sensible heat. About 80% to 90% (Harriman et al. 1999) of the temperature rise of the outside air comes from the conversion of latent heat, while the remainder is the sensible heat carried over by the wheel. Jurinak (1983) developed the

following model to evaluate the effectiveness of a silica gel-operated active desiccant wheel by a curve that fits with the derived wave front propagation characteristics.

$$F1 = \frac{-2865}{T^{1.49}} + 4.344 w^{0.8624} \tag{5.5}$$

$$F2 = \frac{T^{1.49}}{6360} - 1.127 w^{0.07969} \tag{5.6}$$

$$\varepsilon_{F1} = \frac{F1_{o,2} - F1_{o,1}}{F1_{r,1} - F1_{o,1}} \tag{5.7}$$

$$\varepsilon_{F2} = \frac{F2_{o,2} - F2_{o,1}}{F2_{r,1} - F2_{o,1}} \tag{5.8}$$

F1 and F2 correspond to isopotential lines of enthalpy and relative humidity. ε_{F1} and ε_{F2} represent the effectiveness of the total energy and moisture removal at optimum rotary speeds. The subscripts "o" and "r" refer to the OA and regeneration air, respectively. The subscripts "1" and "2" correspond to the inlet and outlet. T is temperature in K and w is the humidity ratio in kg (moisture)/kg (dry air). The outlet temperature and the humidity of the OA and the regeneration air can all be found iteratively by using this model.

Because of the temperature increase when the OA passes through the desiccant wheel, the sensible energy wheel is integrated into the system to cool down the outside air and increase the energy efficiency. The amount of heat removed from the outside air depends upon the temperature on the other side of the heat exchanger. The maximum efficiency can be obtained when the system takes the exhaust air from the space and cools it via evaporative cooling. When exhaust air is not available, outside air can be used and cooled by an evaporative cooler; then passed through the sensible wheel to cool down the fresh outside air, as shown in Figure 5.2.

The advantage of the active desiccant system is that this system can continuously and deeply dry the outside air in all weather conditions, regardless of the moisture content of the exhaust air. The desiccant wheel can be regenerated with either the exhaust air or the outside air, which provides installation flexibility for places where exhaust air is not available.

5.4 Transient Model of Dehumidification

When the dew point of the indoor air is higher than the chilled panel surface temperature, water starts to condense on the surface of the cooling panels. The dew point of the indoor air is

decided by the moisture balance among indoor latent heat, the infiltration moisture and the mechanical ventilation moisture. This transient study is necessary to decide the relationship among these parameters and to determine how much earlier the dehumidification unit needs to be started before the chilled panels are operated, in order to avoid condensation. The steady model used in the latter section of this condensation study is derived from the transient model.

5.4.1 Dehumidification of Passive Desiccant System

If we take a space, as shown in Figure 5.1, as a control space, the moisture balance inside the space can be described by the following equation:

$$V_r \rho_r \frac{dw_r}{dt} = \dot{V}_s \rho_s (w_s - w_r) + ach_i V_r \rho_o (w_o - w_r) + \dot{m}_{gen} \tag{5.9}$$

w_r, w_o, w_s are the room humidity ratio, the outside air humidity ratio and the supply air humidity ratio, respectively. For the passive desiccant system shown in Figure 5.1, the parameters of the supply air after the desiccant wheel can be calculated by changing equations (5.1)-(5.4), as follows:

$$T_{o2} = T_{o1} - \varepsilon_s \frac{(C_p \dot{m})_{min}}{(C_p \dot{m})_s} (T_{o1} - T_{e1}) = T_{o1} - \varepsilon_s \beta (T_{o1} - T_r) \tag{5.10}$$

$$w_{o2} = w_{o1} - \varepsilon_l \frac{\dot{m}_{min}}{\dot{m}_s} (w_{o1} - w_{e1}) = w_{o1} - \varepsilon_l \beta (w_{o1} - w_r) \tag{5.11}$$

$$\beta \approx \frac{\dot{m}_{min}}{\dot{m}_s} \approx \frac{V_{min}}{V_s} \tag{5.12}$$

The subscript "min" in Equations (5.10) – (5.12) represents the smaller of the supply air flow rate and the exhaust air flow rate. The subscript "s" indicates supply air while β is the ratio of the smaller flow rate to the larger flow rate. In a balanced system, the volume flow rate of supply air is equal to the exhaust air, and $\beta = 1$.

5.4.1.1 Case 1. No Post Cooling Used

Post cooling is the availability of cooling after desiccant wheel. When the cooling after desiccant wheel is not available, $w_s = w_{02}$. Then Equation (5.11) is substituted into Equation (5.9), in order to obtain the following equation:

$$\frac{dw_r}{dt} = -w_r \frac{1}{V_r \rho_r} (\dot{V}_s \rho_s (1 - \varepsilon\beta) + ach_i V_r \rho_o) + \frac{1}{V_r \rho_r} (ach_i V_r \rho_o w_o + \dot{V}_s \rho_s w_0 (1 - \varepsilon\beta) + \dot{m}_{gen}) \tag{5.13}$$

Considering the initial conditions, $w_r\big|_{t=0} = w_{r0} = w_o$, the above equation can be solved as:

$$w_r = (w_{r0} - \frac{b}{a})e^{-at} + \frac{b}{a} \qquad (5.14)$$

In equation (5.14),

$$a = \frac{1}{V_r \rho_r}\left(\dot{V}_s \rho_s (1 - \varepsilon\beta) + ach_i V_r \rho_o\right) \qquad (5.15a)$$

$$b = \frac{1}{V_r \rho_r}\left(ach_i V_r \rho_o w_o + \dot{V}_s \rho_s w_0 (1 - \varepsilon\beta) + \dot{m}_{gen}\right) \qquad (5.15b)$$

In the equilibrium state,

$$w_r = \frac{b}{a} \qquad (5.16)$$

5.4.1.2 Case 2. Post cooling is used with the supply air condition: 55°F, 0.0092lb/lb.

Equation (5.9) can be written as:

$$\frac{V_r \rho_s dw_r}{dt} = -\dot{V}_s \rho_s (0.0092 - w_r) + ach_i V_r \rho_o [w_o - w_r] + \dot{m}_{gen} \qquad (5.17)$$

Solving the above equation, we can obtain an equation similar in format to Equation (5.14) with

$$a = \frac{1}{V_r \rho_r}\left(\dot{V}_s \rho_s + ach_i V_r \rho_o\right) \qquad (5.18a)$$

$$b = \frac{1}{V_r \rho_r}\left(ach_i V_r \rho_o w_o + 0.0092\dot{V}_s \rho_s + \dot{m}_{gen}\right) \qquad (5.18b)$$

At the equilibrium state,

$$w_r = \frac{b}{a} \qquad (5.19)$$

Using Equations (5.14) (5.15) and (5.18), the transient processes of dehumidification with and without post cooling can be plotted as shown in Figures 5.3 and 5.4, when the outside air condition is 61°F and $w_o = 0.0107$ lb/lb. This transient process assumes that the initial humidity ratio in the space equals the outside air humidity w_o and 25 people are using the space when the

ventilation system begins operation. 0.13lb/hr per person is assumed for moisture generation. An infiltration rate of 0.45 air changes per hour is assumed. This value is based on the calibrated simulation model and site measurements.

Figure 5.3 shows that the passive desiccant wheel actually adds moisture to the space instead of removing moisture from the space when the cooling coil is turned off. This means that the dehumidifying function of a passive desiccant wheel depends upon the dryness of the exhaust air. For a balanced flow passive desiccant system, the higher the ventilation rate, the lower the indoor humidity level. When the indoor humidity level reaches equilibrium, the inside humidity level is higher than the outside level. The desiccant wheel actually absorbs moisture from the exhaust air and releases it to the supply air when the humidity ratio of the exhaust air is higher than the supply air. This is the reason the passive desiccant wheel does not lower the space's humidity or even increases humidity levels when post cooling is not available, and there are no other dehumidification sources.
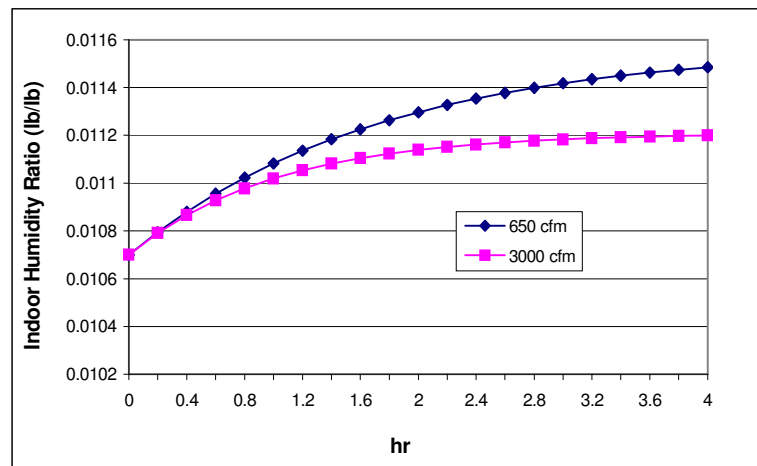
Figure 5.3. Transient Behavior of Indoor Humidity for a Passive Desiccant System with No Post Cooling.
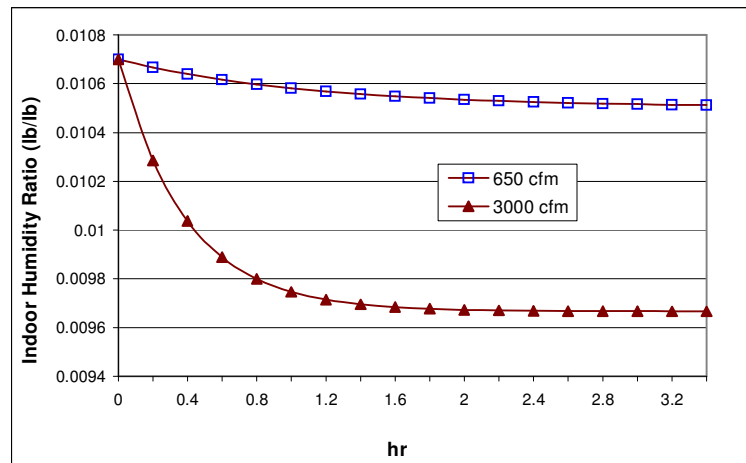
Figure 5.4. Transient Behavior of Indoor Humidity for a Passive Desiccant System with Post Cooling.

Figure 5.4 shows that the high ventilation rate quickly dries the space when the post cooling is on (the supply air is cooled to 55°F, 0.0092lb/lb). However, it also creates another problem. To cool or heat a large volume of outside air will consume more energy. Figures 5.3 and 5.4 indicate that the moisture removing ability of a passive desiccant wheel requires the presence of post cooling.
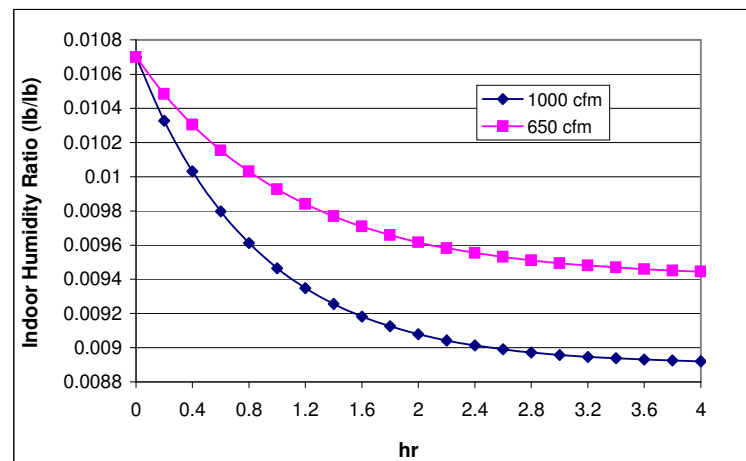
Figure 5.5. Transient Behavior of Indoor Humidity for an Active Desiccant System

5.4.2 Dehumidification with an Active Desiccant System

The active desiccant system shown in Figure 5.2 can dry a space more effectively than a passive system, because the humidity ratio after the desiccant wheel can be set to a relatively low level by adjusting the regeneration air temperature to a high value. The transient behavior of an active desiccant system is the same as that of a passive desiccant unit with post cooling as analyzed in the previous section. When the humidity ratio after the desiccant wheel is set to 0.007 lb/lb (dew point 48°F), the space humidity decreases, as shown in Figure 5.5. The humidity ratio of the supply air is decided by the regeneration air temperature and humidity. The active desiccant system can reduce the supply air humidity ratio to a lower level than a passive desiccant system. The reason is that the chilled water temperature at the inlet of the post cooling coil in passive desiccant units depends upon the operating conditions of the chiller or the DX coil. Normally this temperature cannot be lower 40°F in a university campus loop. Figure 5.6 shows the relationship between the humidity ratio after the wheel and the regeneration air temperature based on Jurinak's model (1983) (Equations (5.5)-(5.8)). Desiccant wheel inlet air conditions of 61°F, 0.0107lb/lb; $\varepsilon_{F1} = 0.3$, $\varepsilon_{F2} = 0.85$ are assumed in Figure 5.6. w_{r1} in Figure 5.6 is the regeneration air humidity ratio. It can be seen that the ideal supply air humidity ratio of the air leaving the desiccant wheel has a nearly linear relationship with the regeneration air temperature.
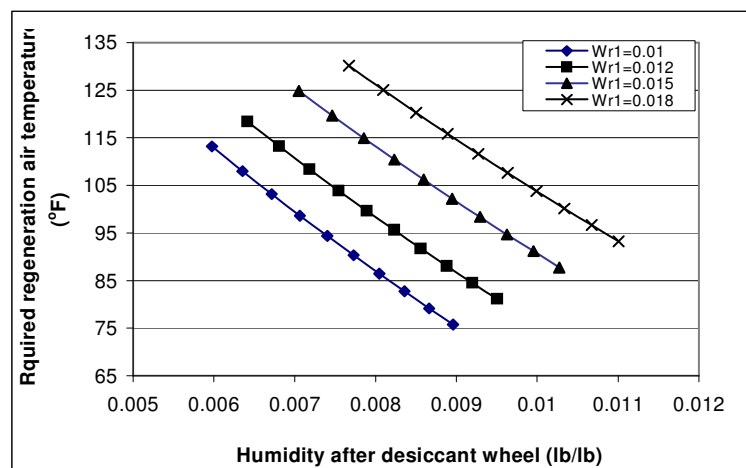
Figure 5.6 Relationship Between Humidity Ratio and Regeneration Air Temperature

5.5 Condensation and Energy Consumption Analysis

Condensation is often a major problem when applying the radiant cooling system. An indoor humidity ratio higher than the saturation humidity ratio at the radiant panel surface temperature will cause water to condense on the surface of the radiant cooling panels, which results in the shutting down of the cooling panels by the control system and the overheating of the space. To avoid condensation, the dew point of the indoor air must be below the surface temperature of the radiant cooling panels. The normal design conditions for the indoor air is 75°F and a 50% relative humidity ratio, which corresponds to a dew point of 55°F and an absolute humidity ratio of 0.0092 lb (water)/lb (dry air). ASHRAE Standard 55-2004 recommends an upper limit for indoor humidity of 0.012 lb/lb, which corresponds to a dew point of 62°F. To ensure that there is no condensation, the design surface temperature of a radiant panel is normally 1-3°F higher than the dew point of the indoor air. Therefore, the inlet chilled water temperature of the radiant panels is often set to 62-65°F. Increasing the panel surface temperature will increase the safety, but will decrease the cooling capacity. To avoid water condensation, the indoor humidity ratio needs to be controlled below 0.012 lb/lb, which corresponds to a dew point of 62°F.

Radiant heating and cooling of a space is typically integrated with a ventilation system that provides humidity control. The ventilation system can be a 100% outside air handling unit, a simple passive desiccant system, as shown in Figure 5.1, or an active desiccant system, as shown in Figure 5.2. An air-handling unit is easier to control, but is less efficient. An active desiccant system usually is considered when the dew point of the supply air is required to be below 45°F (humidity ratio below 0.0063lb/lb) according to Gatley (2000). An active desiccant system often has a life cycle cost advantage when the dew point temperature of the ventilation air is required to be below 40°F. Radiant cooling integrated with a passive desiccant ventilation system has been shown to be a cost effective way to maintain a healthy and comfortable indoor air environment (2001). Several factors in this type of system have an important impact on the indoor humidity ratio. These include the infiltration rate, the outside air flow rate, and the outside humidity ratio.

The Intelligent Workplace used a passive desiccant system before 2006, as shown in Figure 5.1. Chilled water is available only from June to September each year. Consequently, radiant cooling with post cooling of the passive desiccant wheel is used only from June to September. The infiltration rate has been estimated to average 0.45 air changes per hour on a yearly basis, as

noted earlier. Condensation occurs on the surface of the mullion system during the summer. The hourly indoor humidity has been simulated under eight different conditions by using the model of Equations (5.9) to (5.19). These eight conditions are shown in Table 5.1. Figures 5.7-5.10 show the simulated indoor humidity ratio over a one year period. The occupancy is assumed to be 25 from 9:00am to 8:00pm. The corresponding moisture generation in the space is about 3.25lb/hr. The ventilation system is assumed to run continuously in order to clearly show the humidity trend in an hourly time series over the year. Equilibrium conditions are assumed in the hourly simulation.

When the ventilation air flow rate is equal to the exhaust air flow, the space pressure is neutral. The infiltration rate has a significant impact on the indoor humidity ratio. Figures 5.7a (Case 1) and 5.7b (Case 2) indicate when the OA is 650CFM and the supply air humidity ratio is 0.0092 lb/lb (dew point of 55°F), the indoor humidity level can be controlled below 0.011lb/lb over the whole summer in a tight building (ACH equals 0.001). In a leaky condition (ACH equals 0.45), a significant number of hours have a humidity level higher than 0.012 lb/lb (dew point of 62°F) in the summer. During these periods, water will condense on the surface of the radiant cooling panels when the panel surface temperature is 62°F or lower. Condensation has been observed at times during the summer. Another important trend to be noted is that the indoor humidity level during some hours in April, May and October is much higher than 0.012 in a tight building, because the post cooling is turned off. High humidity may cause indoor comfort problems during these periods. The tested space has operable windows, so this problem is not as serious as that which is demonstrated in the graphs.

Table 5.1. Simulation Conditions

	Infiltration (ACH)	Supply (CFM)	Supply Air Humidity Ratio (lb/lb)	Return (CFM)
Case 1	0.001	650	0.0092	650
Case 2	0.450	650	0.0092	650
Case 3	0.001	1600	0.0092	1600
Case 4	0.450	1600	0.0092	1600
Case 5	0.001	650	0.008	650
Case 6	0.450	650	0.008	650
Case 7	0.000	650	0.0092	0
Case 8	0.000	850	0.0092	650
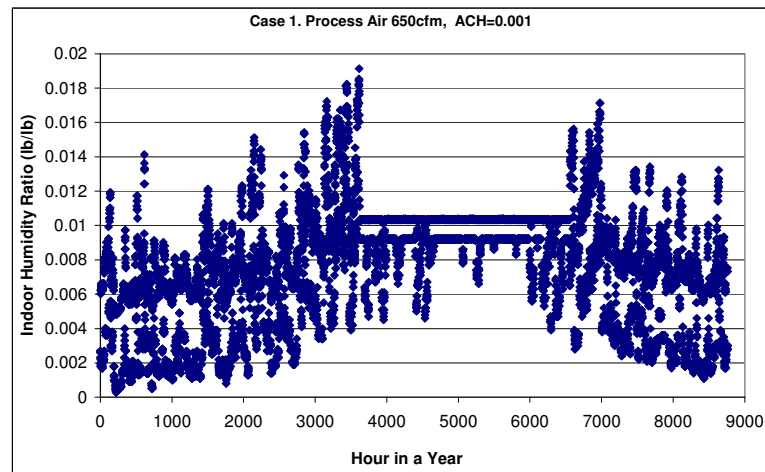
Figure 5.7A. Case 1. OA: 650CFM, ACH:0.001, Supply Air Humidity Ratio: 0.0092 lb/lb.
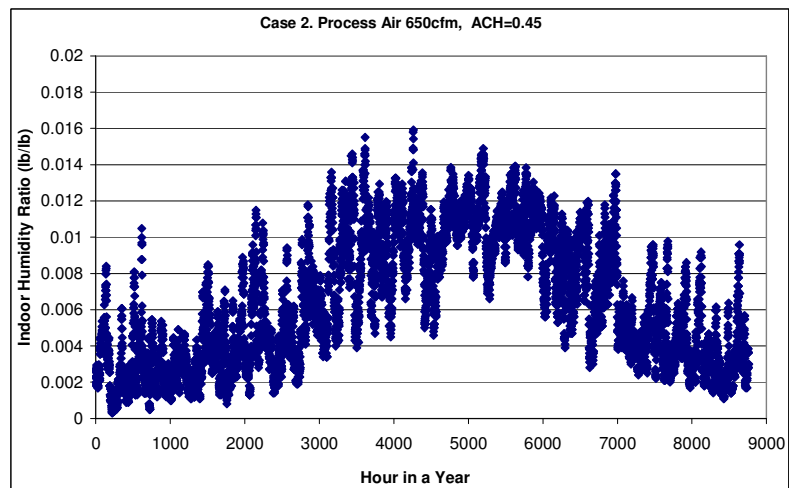
Figure 5.7B. Case 2. OA: 650CFM, ACH:0.45, Supply Air Humidity Ratio: 0.0092 lb/lb.
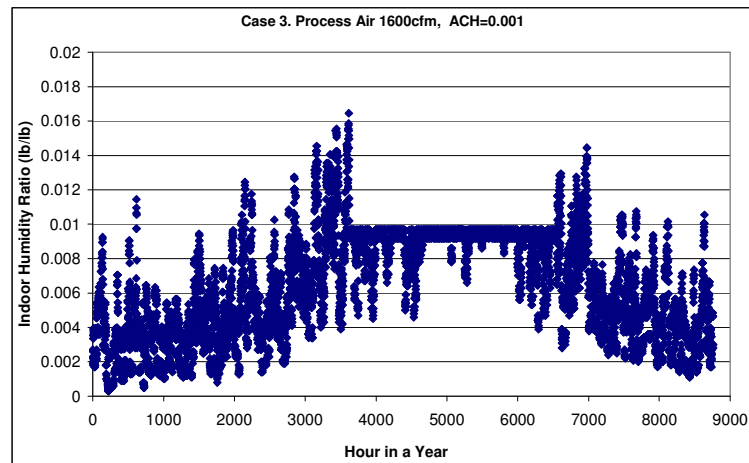
Figure 5.8A. Case 3. OA: 1600CFM, ACH:0.001, Supply Air Humidity Ratio: 0.0092 lb/lb.
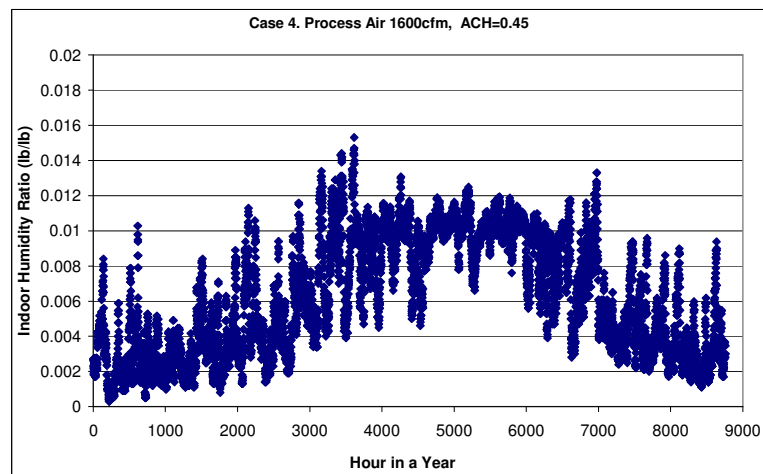
Figure 5.8B. Case 4. OA: 1600CFM, ACH:0.45, Supply Air Humidity Ratio: 0.0092 lb/lb.

In order to reduce the indoor humidity level during the summer, two approaches can be taken. One is supplying more dried outside air to the space, as shown in Cases 3 and 4. The other is to further reduce the humidity ratio of the supply air, as in Cases 5 and 6. Indoor humidity ratios for an increased ventilation rate are shown in Figures 5.8a and 5.8b. 1600CFM is the potential maximum outside air requirement. If the desiccant ventilation unit runs at 1600CFM with an infiltration rate of 0.001ACH, the summer indoor humidity ratio can be controlled under 0.01lb/lb (dew point of 60°F). At the current leakage level of 0.45ACH, the humidity ratio can

also be controlled under 0.012lb/lb (dew point of 62°F) during most summer hours at the ventilation rate used in Figure 9b. However, energy consumption needs to be considered. The higher ventilation rate will increase the energy consumption in conditioning the outside air, even though the heat recovery by the enthalpy wheel also increases.
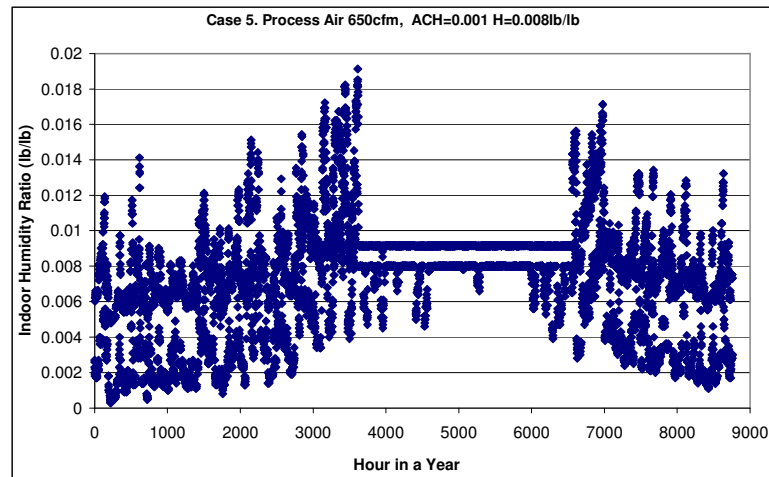
Figure 5.9A. Case 5. OA: 650CFM, ACH:0.001, Supply Air Humidity Ratio: 0.008 lb/lb
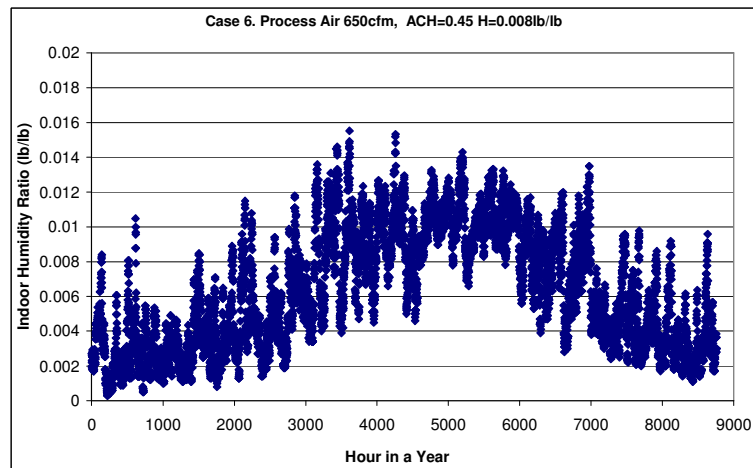
Figure 5.9B. Case 6. OA: 650CFM, ACH:0.45, Supply Air Humidity Ratio: 0.008 lb/lb.

Another option for reducing indoor humidity levels in summer is to reduce the supply air humidity ratio, as shown in Figures 5.9a (Case 5) and 5.9b (Case 6). The humidity ratio of the

supplied ventilation air is set to 0.008 lb/lb (dew point of 52°F). Comparing Figure 5.9a with Figure 5.8a, it can be seen that the indoor humidity level in summer is even lower at an OA rate of 650CFM with a humidity ratio of 0.008lb/lb than at 1600CFM with a humidity ratio of 0.0092 lb/lb in a tight building. Figure 5.9b illustrates that the condition of Case 6 cannot effectively control the humidity level below 0.012 lb/lb during the summer season. Moisture condensation on cooling panels cannot be avoided under these conditions. Figure 5.9a shows that the humidity level in the tight space of Case 5 is frequently higher than that in the leakier space of Case 6 (Figure 5.9b) during the winter, spring and fall, when post cooling is not available. The reason for the difference is that when a building is leaky, the drier outside air removes the indoor moisture in winter, spring and fall, in a dry climate.
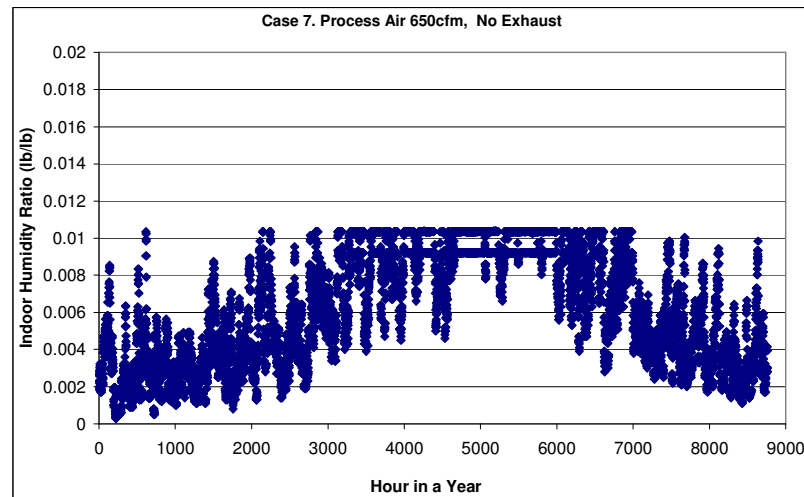
Figure 5.10A. Case 7. OA:650CFM, No Exhaust Air, ACH:0, Supply Air Humidity Ratio: 0.0092 lb/lb

Because the infiltration has a significant impact on the indoor humidity ratio in a radiantly cooled space, measures must be taken to reduce the infiltration. One method is to pressurize the building to reduce or stop the outside air entering the space during the summer. Two cases (Cases 7 and 8) are simulated. Case 7 assumes that 650CFM of OA is supplied without exhaust air and heat recovery in order to pressurize the space, as shown in Figure 5.10a. Case 8 assumes that 850CFM of OA is supplied and 650CFM of air is exhausted with the heat recovery to slightly pressurize the space, as shown in Figure 5.10b. Figures 5.10a and 5.10b indicate that the

indoor humidity ratio can easily be controlled under 0.011 lb/lb (dew point of 52°F) in both conditions, if the space is pressurized and the infiltration is reduced to be close to zero. However, there is another drawback. In Case 7 of Figure 5.10a, there is no heat recovery because there is no exhaust air. In Case 8 of Figure 5.10b, increasing the ventilation air from 650CFM to 850CFM will increase energy consumption.
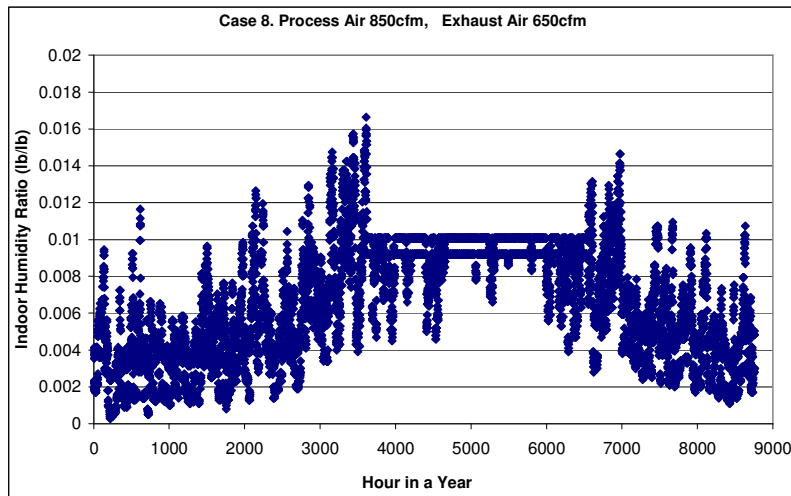
Figure 5.10B. Case 8. OA: 850CFM, Exhaust Air 650CFM, ACH:0.001, Supply Air Humidity Ratio: 0.0092 lb/lb.
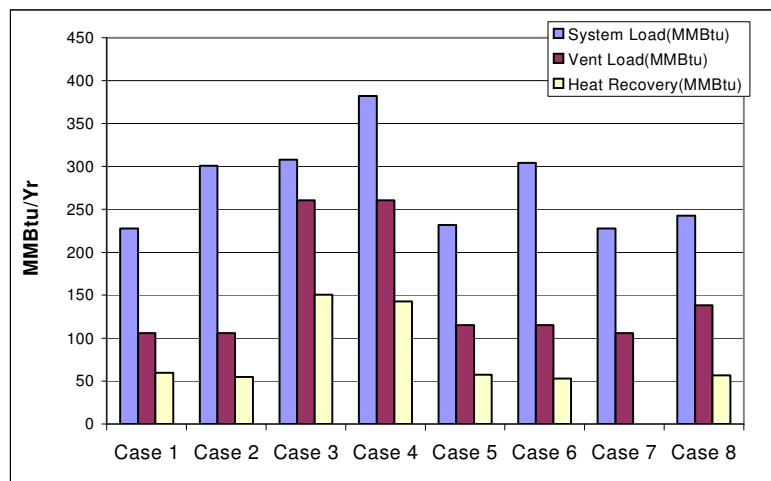
Figure 5.11A. System Load, Ventilation Load and Heat Recovery of Different Cases
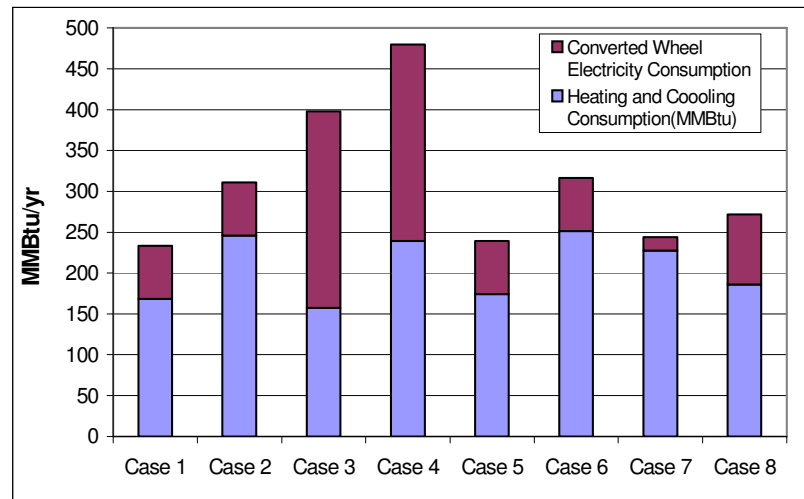
Figure 5.11B Estimation of Primary Energy Consumption per Year

Energy consumption values for each of Cases 1 (Figure 5.7a) through 8 (Figure 5.10b) have been simulated. The results are shown in Figures 5.11a and 5.11b. The conditions corresponding to each of Cases 1 to 8 are given in Table 5.1. The ventilation system is assumed to run from 6:00am to 8:00pm. The total building system load is compared with the ventilation load and the heat recovery in each case. The results are shown in Figure 5.11a. The total system load is calculated by assuming that the OA is conditioned by a normal air-handling unit without heat recovery. The ventilation load is calculated by assuming that 100% of the ventilation air is conditioned by a cooling or heating coil in the desiccant unit without heat recovery in order to compare it with the heat recovered by the desiccant wheel. From Figure 5.11a, it can be seen that the higher the ventilation rate, the higher the building system load and ventilation load. The heat recovery is also higher. The amount of heat recovered by a passive desiccant wheel accounts for 50% of the ventilation load. Figures 5.11a and 5.11b show that the infiltration and ventilation ratios are two important factors affecting the total system load. These two factors explain why the system load and the ventilation load of Cases 3 and 4 are the largest, as shown in Figure 5.11a. By considering the electricity used by the passive desiccant wheel itself, the net primary energy consumption is as shown in Figure 5.11b. Thermal energy is converted to primary energy

by considering a generic boiler efficiency of 0.75. Electricity consumption (kWh) is converted to primary energy (MMBtu) by a conversion factor of 3.52, which is based on a national electricity generation and distribution efficiency of 0.284 (EIA, 2006). The result shows that Case 1 (OA 650CFM, ACH 0.001) uses the least energy. The primary energy consumption of Cases 1, 5, 7 and 8 are relatively close to each other. The infiltration and ventilation rate have a significant impact on energy consumption in an oversized ventilation system. The primary energy consumption can increase of 35.7% when infiltration rate increases from 0.0 (Case 1) to 0.45 (Case 2); and at the same infiltration condition of 0.45 ACH, the primary energy consumption could increase about 42.4% when the ventilation rate increases from 650 CFM (Case 2) to 1600 CFM (Case 4).

Compared with the indoor humidity levels in Figures 5.7 to 5.10, it can be concluded that Case 8 is the best solution for a leaky space with a radiant cooling system. This means that pressurizing the space or sealing the leakage sites is very important to control condensation in a radiantly cooled space.

5.6 Operation Strategies to Control Condensation

To avoid condensation in a radiantly cooled space, the following operating strategies are recommended.

Occupants and infiltration air are the main sources of moisture for the indoor environment during the summer. Infiltration air can lead to condensation on the radiant panels. Checking and caulking leakage points in the space will reduce infiltration and eliminate condensation if the infiltration is sufficiently reduced. Window openings should be restricted in summer when the radiant cooling is running. The supply air rate should be higher than the exhaust air flow, as shown in Case 8, to pressurize the space. Although some energy is lost when pressurizing the space, this can be an effective means for controlling indoor humidity level.

The desiccant ventilation system should start at least one hour before the space is occupied. When the space is highly occupied, the humidity sensor in the space should be able to modulate the cooling coil control valve in the desiccant unit to reduce the supply air temperature and the humidity ratio. Meanwhile, when the measured dew point of the indoor air is close to the inlet water temperature of the radiant panel, the inlet valve of the radiant panel should be shut down.

In a radiantly cooled space with an integrated desiccant ventilation system, space cooling is provided by two sources: radiant panels and ventilation air. At low loads, cooling should be provided by ventilation air. As the cooling load increases, the temperature of the supplied ventilation air should be adjusted to match the load. When the supplied ventilation air temperature drops to a low limit of 55^oF or 52^oF at high cooling loads, the inlet control valve of the radiant panels starts to modulate to maintain the room air temperature at 76^oF. The radiant panels will not be enabled until the indoor dew point is below a safe limit, such as 0.011lb/lb (dew point of 60^oF). Then the temperature of the chilled water entering the panels is modulated to meet the space-sensible load. The inlet water temperature should be controlled to be 1-2^oF higher than the space dew point temperature to avoid water condensation.

Ventilation systems in radiantly cooled spaces can be oversized in the design phase. Sometimes, the oversized ventilation systems can satisfy the cooling load alone, even on a hot day. However, the higher ventilation rate will increase energy consumption. The supply air fan should be a variable speed fan to match the ventilation air with the space fresh air requirements so that the space will not be over-ventilated.

A passive desiccant ventilation system increases the indoor humidity in spring and fall when there is no cooling load in the space and the post cooling is shut off to save energy. The indoor humidity ratio will be too high to be comfortable in a tight space, as shown in Figures 5.7a, 5.8a, and 5.9a. Windows should be allowed to open. The drier outside air can remove indoor moisture.

5.7 Summary

A passive desiccant system and an active desiccant system have been compared in this chapter. The transient processes of dehumidification in a radiantly cooled space have been studied. A transient model is set up. Hourly indoor humidity at eight different operating conditions is analyzed based on the steady state of the transient model. The corresponding energy consumption values of the different cases have been simulated. Comparing energy consumption and yearly indoor humidity trends of the eight cases, the following conclusions can be reached:

An active desiccant system dries a space deeply and continuously, while a passive desiccant system dries a space more energy efficiently. The moisture removal capacity of a passive desiccant system depends upon the dryness of the exhaust air. When a passive ventilation system is the only source of dehumidification, the system cannot remove moisture without post cooling.

High infiltration is one of the main causes of condensation in a radiantly cooled space in summer. Radiant panels cannot work without condensation in a leaky space (ACH: 0.45) even if the supply air is conditioned to 52°F, 0.008lb/lb, as shown in Figure 5.9b. A passive desiccant system may cause some humidity problems in a tight space in spring and fall when post cooling is not necessary because there is no cooling load, as shown in Figures 5.7a, 5.8a and 5.9a. Opening windows during this period of time can solve this problem.

Pressurizing the space with ventilation air is one of the possible solutions to avoid water condensation on the surface of radiant cooling panels in a leaky building.

An optimized cooling control sequence is necessary for condensation control, such as starting the ventilation system one hour before the space is occupied and cooling the space by stages.

A passive desiccant ventilation system can recover about 50% of the energy of the ventilation load and provides reasonable humidity control in a tight, radiantly cooled space.

The infiltration and ventilation rate have a significant impact on energy consumption in an oversized ventilation system. The primary energy consumption can increase of 35.7% when infiltration rate increases from 0.0 (Case 1) to 0.45 (Case 2); and at the same infiltration condition of 0.45 ACH, the primary energy consumption could increase about 42.4% when the ventilation rate increases from 650 CFM (Case 2) to 1600 CFM (Case 4).

CHAPTER VI

THE INFILTRATION STUDY OF A RADIANTLY HEATED AND COOLED OFFICE

6.1 Introduction

Chapter V identified the infiltration rate is the primary factor which affects the indoor humidity ratio, the safe operation of a radiant cooling system, and the energy consumption of the Intelligent Workplace. The objective of this chapter is to investigate the infiltration value of the IW.

Creating a comfortable and healthy indoor environment for the occupants is a primary concern of HVAC engineers. Comfort and indoor air quality depend upon many factors including thermal regulation, control of internal and external sources of pollutants, supply of acceptable air and removal of unacceptable air, and proper operation and maintenance of building systems (ASHRAE 2005). An adequate outside air supply is necessary to dilute and remove indoor air contaminants. Outside air is normally provided by mechanical ventilation in commercial buildings and natural ventilation in residential buildings. ASHRAE Standard 62.1-2004 prescribes the minimum ventilation requirement for different types of buildings. For classrooms and offices in educational facilities, the minimum ventilation rates are 0.12cfm/ft^2 and 0.06cfm/ft^2, respectively. Energy required to condition the outdoor air can be a significant portion of the total space's conditioning load. The magnitude of the outdoor airflow into the building must be known for a proper sizing of the HVAC equipment and an evaluation of energy consumption.

The outside air exchange rate of buildings can be divided into two parts. One is mechanical ventilation; the other is infiltration. In order to accurately simulate the heating and cooling consumption of the Intelligent Workplace (IW) and precisely size the equipment in the energy supply and energy distribution systems, the infiltration level of the IW needs to be carefully measured and studied. This chapter provides an overview of previous IW infiltration studies, analyzes blower door measurement results and evaluates the IW infiltration by considering the impact of wind speed and temperature differences. This chapter also evaluates IW infiltration from several other measurement methods such as CO_2 concentration and logged humidity data. Some of the possible leakage sites have been identified by a site visit.

6.2 Previous Infiltration Studies of the IW

6.2.1 Infiltration Measurement by Tracer Gas Method

Several studies have been done to estimate the real infiltration level of the IW. Mahdavi et al. (2000) measured the entire infiltration of the IW using the tracer gas method. They installed six sampling points, A1-A6, as shown in Figure 6.1, in the IW during the test conducted on March 28, 1998. They observed the average infiltration to be 0.86ACH. They performed the measurement again on April 2, 1998 using four samplers (B1, B2, B4, B6). They observed an average infiltration of 0.95ACH.
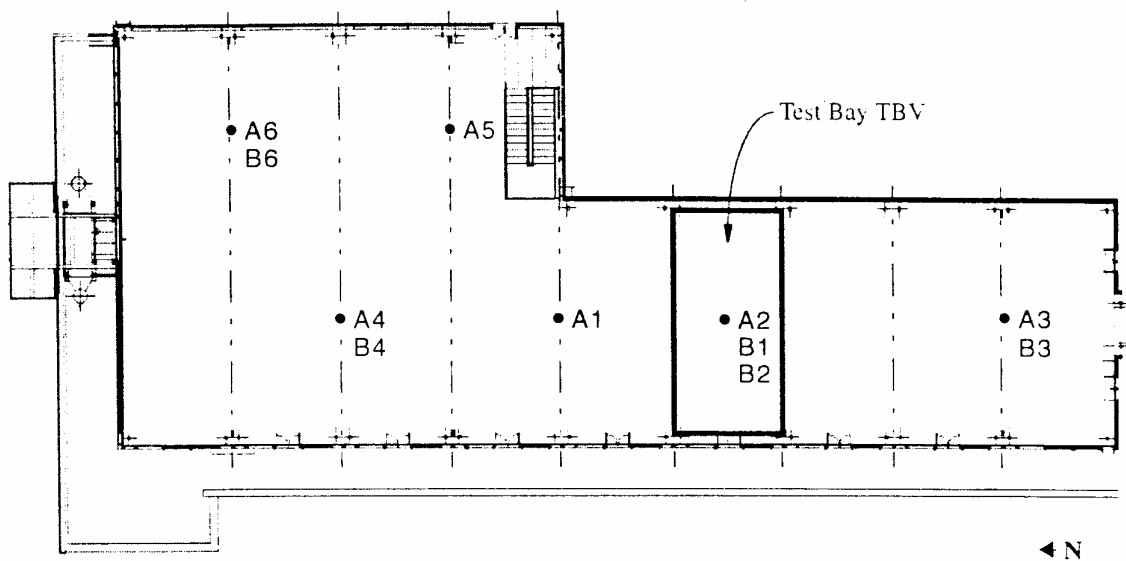
Figure 6.1.Tracer Gas Sampler Locations in the IW during the Infiltration Measurement

Boonyakiat (2003) also did a series of infiltration measurements in one bay (Bay 1) of the IW in July and August of 1999. The results he obtained are listed in Table 6.1. Experiments numbered 2, 5, 11, and 12 in Table 6.1 were performed, when windows and ventilators were fully closed.

Table 6.1. Infiltration of Bay 1 Using Tracer Gas Measurements (Boonyakiat, 2003)

Experiment 2	Experiment 5	Experiment 11	Experiment 12
1.12	1.31	0.82	0.78

6.2.2 Infiltration Measurement by CO_2 Concentration Method

Betz et al. (2006) carried on a CO_2, occupancy and ventilation study in the spring of 2006. They monitored the CO_2 concentration and the number of occupants in the IW during the ABSIC meeting of March 21 and 22, 2006, and during the Turner Construction Meeting (April , 2006). Their results are shown in Table 6.2. These results seem to be much smaller than the other estimates/measurements of infiltration. Because there is no detailed description of the infiltration analysis in the report, no clues leading to errors can be found. Consequently, the CO_2 concentration data has been re-analyzed in the following section.

Table 6.2. Calculated Infiltration Rate (Betz et al., 2006)

Date	Infiltration (L/s)	Infiltration (h^{-1})	Avg. Temperature (°F)	Avg. Wind speed (mph)
March 20-21	33.03	0.090	27.0	2.64
March 21-22	38.72	0.106	28.5	7.24
March 22-23	26.72	0.072	32.9	5.96

6.3 Analysis of CO_2 Concentration Measurement Data

This chapter re-analyzes the CO_2 concentration data obtained by Betz et al. (2006). The procedure and results are shown as follows. The CO_2 mass balance in the IW can be expressed as the following equation:

$$\frac{dm_{co2}}{dt} = \dot{m}_{in} - \dot{m}_{out} + \dot{m}_{gen} \tag{6.1}$$

Where, $\frac{dm_{CO2}}{dt}$ equals the indoor CO_2 mass change with time. The mass terms in the above equation can be expressed as the CO_2 concentration (PPM).

$$m_{CO2} = C_r * V_r * \rho * 10^{-6} \tag{6.2}$$

$$\dot{m}_{in} = C_o * \rho * \alpha * V_r * 10^{-6} \tag{6.3}$$

$$\dot{m}_{out} = C_r * \rho * \alpha * V_r * 10^{-6} \tag{6.4}$$

By substituting Equations (6.2), (6.3), (6.4) into Equation (6.1), the following equation is obtained:

$$\frac{dC_r}{dt} = -\alpha * \left(C_r - C_o - \frac{\dot{m}_{gen}}{\alpha * V_r * \rho_{CO2} * 10^{-6}} \right) \tag{6.5}$$

By assuming that the initial indoor CO_2 concentration is C_{ro} ppm, the above equation can be solved as:

$$C_r = C_o + \frac{\dot{m}_{gen}}{\alpha * V_r * \rho * 10^{-6}} + \left(C_{ro} - C_o - \frac{\dot{m}_{gen}}{\alpha * V_r * \rho * 10^{-6}} \right) e^{-\alpha t} \tag{6.6}$$

C_r in the above equation is the CO_2 level in the space.

The indoor CO_2 level and occupancy were logged every 10 minutes by three CO_2 sensors. The calibrated average CO_2 concentration was considered to provide the readings of the CO_2 levels inside the space. For every set of two successive measurements, the first measurement can be considered to be the initial CO_2 level, C_{ro}, and the second measurement can be considered to be the indoor CO_2 level, C_r. If C_{ro} and C_r are known in Equation (6.6), the infiltration value, α, can be determined from a trial and error solution of Equation (6.6).

When CO_2 concentration data were logged on March 21-23, 2006, no outside CO_2 level was recorded. On May 3rd, the outdoor CO_2 level was logged when the second measurements were taken. The night outdoor CO_2 level on May 3rd ranged from 345ppm to 405ppm during most of the hours, otherwise the CO_2 level ranged from 380ppm to 400ppm. This chapter assumes the current average worldwide CO_2 concentration, 387 PPM, as the outside CO_2 concentration level (EPA website, 2006). The calculated corresponding 10 minute ACH for March 21 and March 22 are plotted in Figure 6.2. The average hourly ACHs are listed in Table 6.3.

From Figure 6.2, it can be seen that the infiltration range is between 0.09 and 0.83ACH, but the variation of ACH is very large. This may be caused by the sensitivity of CO_2 sensors and the frequent changes in the level of occupants. The outdoor CO_2 concentration is assumed to remain constant during the calculation. In reality, the outdoor CO_2 concentration varies over time instead of remaining a constant value, which may result in an inaccurate calculation of infiltration. Moreover, the infiltration is a function of wind speed and temperature difference. The infiltration

should be lower at noon and higher during the morning and evening. This tendency can be seen from data points collected on March 22, 2006, and shown in Figure 6.2.
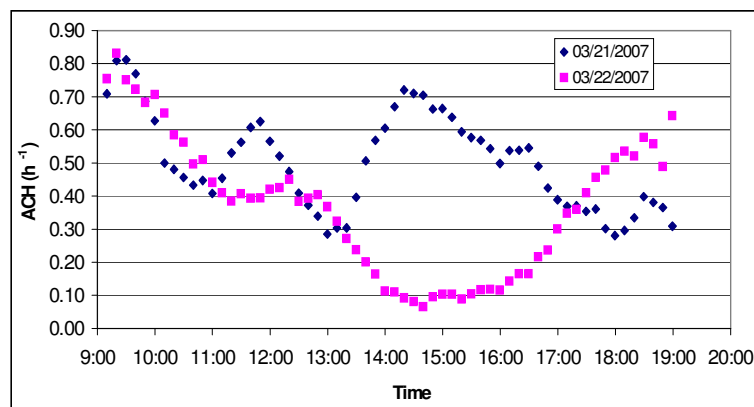
Figure 6.2. Air Change Rate During the ABSIC Meeting on March. 21 and 22, 2006

Table 6.3 Recalculated Infiltration Rate during ABSIC Meeting on March. 21-22, 2006

Time	9:00	10:00	11:00	12:00	1:00	2:00	3:00	4:00	5:00	6:00
3/21/2006 Occupants	37	38	20	35	20	34	36	30	11	5
3/21/2006 Infiltration, ACH	0.63	0.89	0.26	0.74	0.25	0.42	0.83	0.53	0.51	0.28
3/21/2006 Occupants	35	32	27	21	18	5	5	5	8	5
3/22/2006 Infiltration, ACH	0.58	0.83	0.46	0.36	0.51	0.12	0.09	0.09	0.18	0.5

To eliminate the disturbance of frequent changes in occupancy and the variation of the outside CO_2 concentration, another set of CO_2 data was taken on the night of May 3, 2006. The outdoor CO_2 concentrations were recorded at this time. Approximately 3-6 people stayed inside the IW during that night. Figure 6.3 shows the inside and outside CO_2 concentration levels.
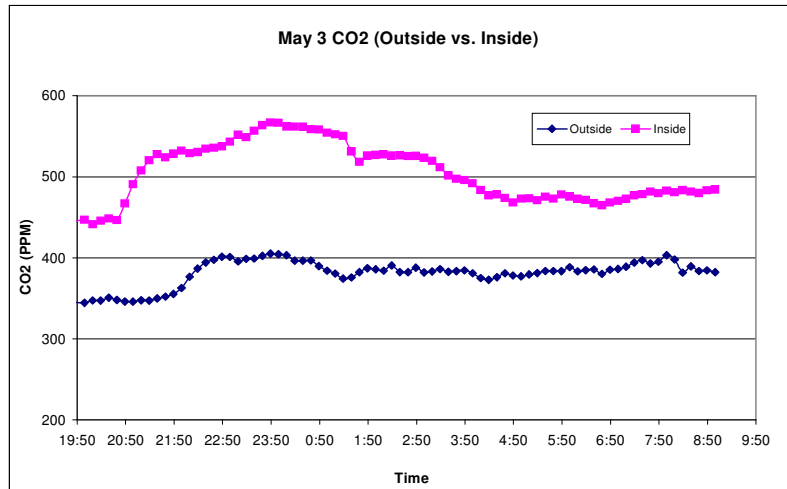
Figure 6.3 Indoor and Outdoor CO$_2$ Concentrations on the Night of May 3, 2006

The infiltration level at each data point can be calculated based on Equation (6). The nighttime infiltration levels for this set of data are plotted in Figure 6.4. It can be seen that the variation of ACH is much smaller when compared to Figure 6.2. The nighttime ACH varies from 0.1 to 0.5.
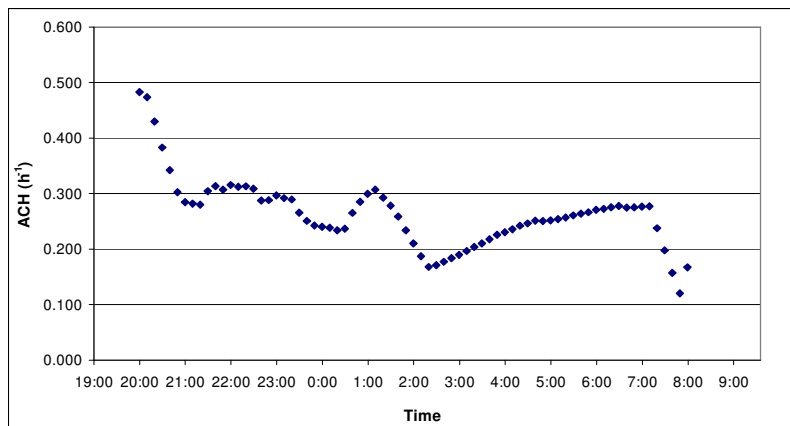
Figure 6.4 Overnight ACH Based CO$_2$ Measurement on May 3, 2006

The above analysis shows the air change rate between the indoor air and outdoor air ranges between 0.09 and 0.83, based on the CO$_2$ concentration measurements.

The accuracy of CO_2 concentration method depends on the accuracy of CO_2 sensors. The relationship between the CO_2 concentration measurement and the infiltration rate, α, can be decided by the following equations. By differentiating equation (6.6), the following equation can be obtained

$$\frac{dC_r}{d\alpha} = \frac{\dot{m}_{gen}}{V_r * \rho * 10^{-6}} * \alpha^{-2}(-1 + e^{-\alpha t}) + \left[(C_{r0} - C_0) * (-\alpha) + \frac{\dot{m}_{gen}}{V_r * \rho * 10^{-6}}\right] * e^{-\alpha t} \quad (6.7)$$

$$\frac{\alpha}{d\alpha} dC_r = \frac{\dot{m}_{gen}}{V_r * \rho * 10^{-6}} * \alpha^{-1}(-1 + e^{-\alpha t}) + \left[(C_{r0} - C_0) * (-\alpha) + \frac{\dot{m}_{gen}}{V_r * \rho * 10^{-6}}\right] * \alpha * e^{-\alpha t} \quad (6.8)$$

Let

$$f(\alpha) = \frac{\dot{m}_{gen}}{V_r * \rho * 10^{-6}} * \alpha^{-1}(-1 + e^{-\alpha t}) + \left[(C_{r0} - C_0) * (-\alpha) + \frac{\dot{m}_{gen}}{V_r * \rho * 10^{-6}}\right] * \alpha * e^{-\alpha t} \quad (6.9)$$

The relative error of infiltration value, $\dfrac{d\alpha}{\alpha}$, can be calculated by the following equations

$$\frac{d\alpha}{\alpha} = \frac{dC_r}{f(\alpha)} \quad (6.10)$$

By assuming initial indoor CO_2 level of 420 PPM, 20 people in the office, measurement time step is 10 minutes and real infiltration is close to 0.6, the infiltration errors induced by the CO_2 measurement errors are listed in Table 6.4.

Table 6.4 Relative Infiltration Errors Induced by CO_2 Measurement

dC_r (PPM)	5	10	15	20	25	30	35	40	45	50
$d\alpha / \alpha$	0.104	0.207	0.311	0.414	0.518	0.621	0.725	0.829	0.932	1.036

From Table 6.4, it can be found that if the error of indoor CO2 measurement is 5PPM, the relative errors of calculated infiltration is 10.4%. If the error of the indoor CO2 measurement is 50PPM, the relative error of calculated infiltration is 103.6%. It can be seen that the calculated infiltration rate is very sensitive to the errors of CO2 measurement.

6.4 Analysis of Blower Door Measurement Data

The blower door is a powerful diagnostic tool for measuring the infiltration of small buildings and for helping to locate air leakage points. The blower door usually consists of an adjustable-speed fan that is sealed into an exterior fiber doorway. The fan blows air into or out of the building to create a slight pressure difference between the inside and outside. This pressure difference forces air through all of the holes and penetrations in the exterior envelope. By measuring the pressure differences between the outside and inside of the building and the air flow rate through the fan at different fan speeds, the airtightness of the entire building envelope can be calculated. The tighter the building, the less air flow the fan needs in order to create a change in building pressure.

The infiltration rates obtained from the blower door tests are ACH50, which is when air changes per each hour at 50 Pascals (Pa) of fan pressure. This value can be converted into a simple estimation of the seasonal natural air change rate (ACH) by the following relation, according to Sherman and Dickerhoff (1998):

$$ACH \approx \frac{ACH_{50}}{20} \tag{6.11}$$

The blower door test can be a pressurization test or a depressurization test in which the blower increases or decreases the pressure within a building above or below the outdoor pressure. The depressurization test is often used in small buildings to identify the leakage sources.

Two blower door measurements have been performed at the IW. One was on Oct 6, 2006, and the other was on Oct 10, 2006. The measurement results are listed in Tables 6.4 and 6.5. Because the blower door is designed for use in the buildings with a floor area less than 3000 ft^2 and the area of the IW is around 6200 ft^2, the blower door fan could not produce a 50 Pa fan pressure difference during these two tests, even through the blower door cover ring was left wide open. Therefore, Equation (6.11) cannot be used to estimate the natural infiltration based on the measured data. The natural infiltration can be calculated by using the equivalent leakage area method (Equation 6.12) according to the ASHRAE Handbook 2005. When the equivalent leakage area is known, the infiltration is a function of the temperature difference and wind speed, and can be expressed by Equation (6.13).

$$A_L = C_5 Q_r \frac{\sqrt{\rho/2\Delta P_r}}{C_D} \tag{6.12}$$

$$Q = A_L \sqrt{C_S \Delta t + C_W U^2} \tag{6.13}$$

$$\alpha = \frac{Q}{V_r} \tag{6.14}$$

Table 6.5. Blower Door Measurement Results on Oct. 6th, 2006

Pressure (Pa)	10.2	11.2	8.6	9	8.8
CFM	5950	5925	5952	5935	5963
Baseline (Pa)	0.94		Wind speed	6 mph	
Wind Direction	NE		Temperature	38ºF	
RH	53%				

Table 6.6. Blower Door Measurement Results on Oct. 10th, 2006

Pressure (Pa)	8.6	8.2	9.1	8.4	8.6	9.2	9	9.3
CFM	6026	6010	5922	6012	5992	6002	5992	5972
Baseline (Pa)	0.46		Wind speed	7 mph				
Wind Direction	NE		Temperature	63ºF				
RH	73%							

Based on the blower door measured data, the equivalent leakage areas of these two tests can be calculated. The results are shown in Table 6.7. The equivalent leakage area of the IW is about 1680 in^2. From the Pittsburgh TMY2 weather data file, the hourly temperature and wind speed can both be known. Therefore, the hourly infiltration can be calculated by Equation (6.13), once the equivalent leakage area A_L is known. The hourly and average daily ACH for a TMY weather year are plotted in Figures 6.5 and 6.6.

Table 6.7. Equivalent Leakage Areas

	Qr	C$_5$	Cd	DP(Pa)	Dp(in WG)	rho	A$_L$ (in2)	A$_L$(ft2)
6-Oct-06	5945	0.186	0.65	9.56	0.0384312	0.075	1680.4	11.67
10-Oct-06	5990	0.186	0.65	8.72	0.03504234	0.075	1773.2	12.31

Table 6.8 Predicted IW Monthly Average Air Change Rate

Month	Temp(F)	Humidity	Wind (mph)	Indoor Temp(°F)	Temp Diff (°F)	AL(in2)	Q(CFM)	ACH
Jan	26.2	0.0021	9.6	72	45.8	1680	2137	1.49
Feb	27.6	0.0022	8.7	72	44.4	1680	2009	1.40
Mar	43.1	0.0038	8.8	72	28.9	1680	1852	1.29
Apr	47.6	0.0043	7.7	72	24.4	1680	1650	1.15
May	60.8	0.0076	6.9	72	11.2	1680	1353	0.94
Jun	69.7	0.0105	6.7	72	2.3	1680	1173	0.82
Jul	70.7	0.011	6.2	72	1.3	1680	1073	0.75
Aug	71.3	0.012	6.2	72	0.7	1680	1061	0.74
Sep	63.5	0.0096	5.4	72	8.5	1680	1091	0.76
Oct	51.7	0.006	7	72	20.3	1680	1502	1.05
Nov	41.5	0.0042	9.2	72	30.5	1680	1925	1.34
Dec	33.5	0.0031	8.7	72	38.5	1680	1946	1.36
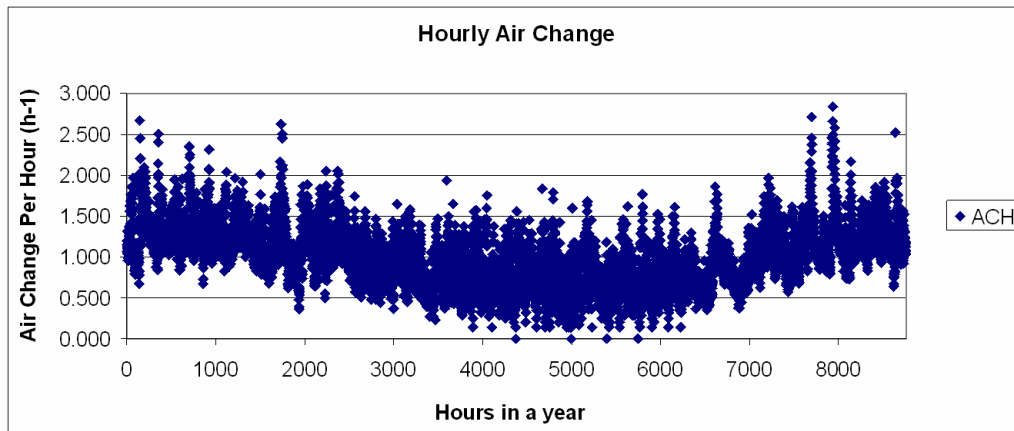
Figure 6.5 IW Hourly Infiltration Based on Interpretation of Blower Door Measurement Data
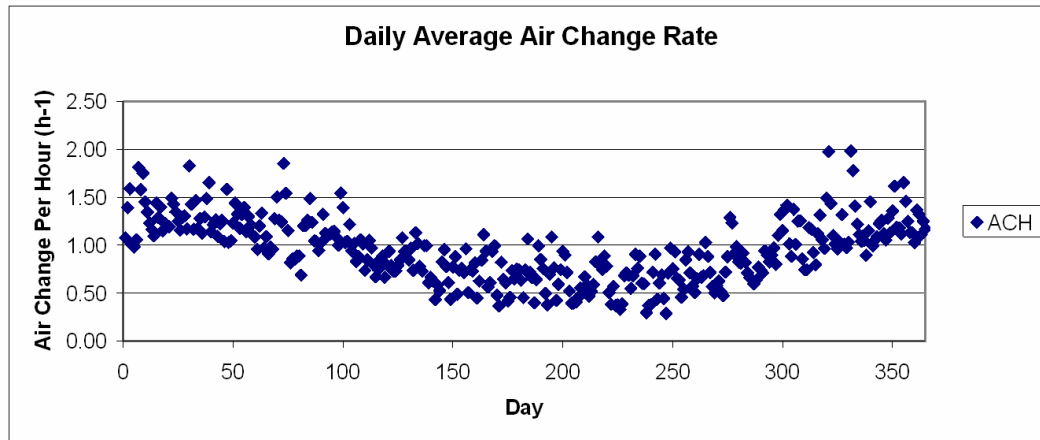
Figure 6.6 IW Average Daily Infiltration Based on Interpretation of Blower Door Measurement Data

From Figures 6.5 and 6.6, it can be seen that the infiltration rate is between 0.5 and 1.5ACH for most of a typical year. The air exchange rate is higher in the winter and lower in the summer. The average monthly infiltration rates are listed in Table 6.8. From Table 6.8, we can see that the monthly average air change rate varies from 0.74 in the summer to 1.49 in the winter which is, in general levels, consistent with the tracer gas measurement results.

6.5 Analysis of Logged Humidity Data

The new IW control system logs the operation status of the active desiccant ventilation unit, SEMCO REV2250, from 2006. The recorded supply air humidity ratio, indoor humidity ratio and outdoor humidity ratio all provide an alternative approach to estimating the infiltration of the IW. The moisture balance of the IW can be written as:

$$\dot{W}_{in} - \dot{W}_{out} + \dot{W}_{gen} = \dot{W}_{storage} \tag{6.15}$$

$$\dot{W}_{in} = 60 * \rho * \dot{V}_s * w_s + \alpha * \rho * V_r * w_o \tag{6.16}$$

$$\dot{W}_{out} = 60 * \rho * \dot{V}_L * w_r + \alpha * \rho * V_r * w_r \tag{6.17}$$

By substituting Equations (6.16) and (6.17) into Equation (6.15) and rearranging the equation, the following infiltration equation can be obtained:

$$\alpha = \frac{60 * \dot{V}_s * w_s - 60 * \dot{V}_L * w_r + \dot{m}_{gen} / \rho}{V_r * w_r - V_r * w_o} \tag{6.18}$$

In the above equation, $\dot{V}_s$, $\dot{V}_e$, w_s , w_r and w_o can be obtained from the control system; V_r is known. Therefore, the infiltration can be calculated based on the logged SEMCO unit operation data. One week's data (August 6-12, 2006) was taken from the control system in the summer of 2006. The supply air flow rate and humidity ratios for the time period of August 6, 2006, to August 8, 2006, are plotted in Figures 6.7 and 6.8. From this measured information, the air change rate can be calculated for every 15 minute period. The results are shown in Figure 6.9.
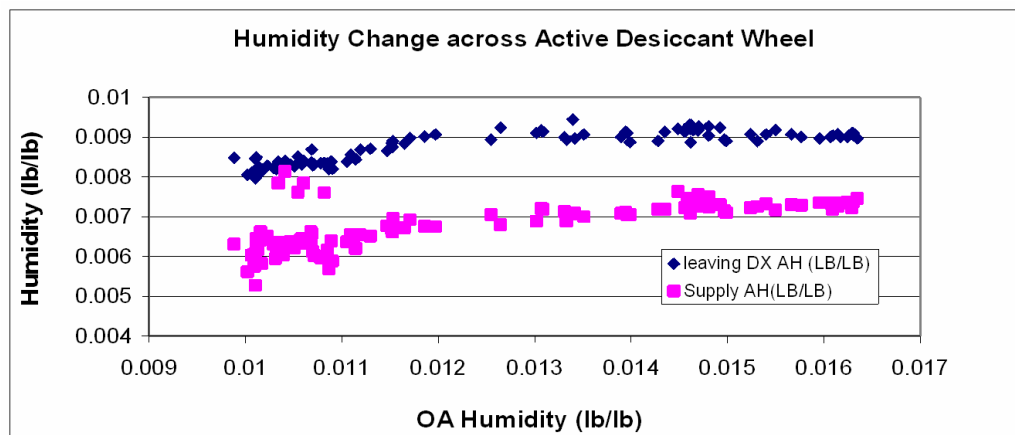
Figure 6.7 Supply Air Humidity Ratios
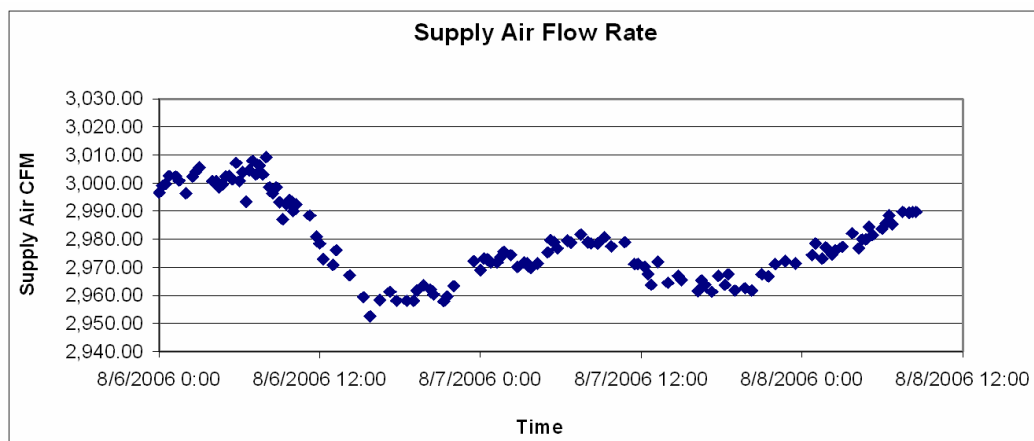
Figure 6.8 Supply Air Flow Rate (CFM)
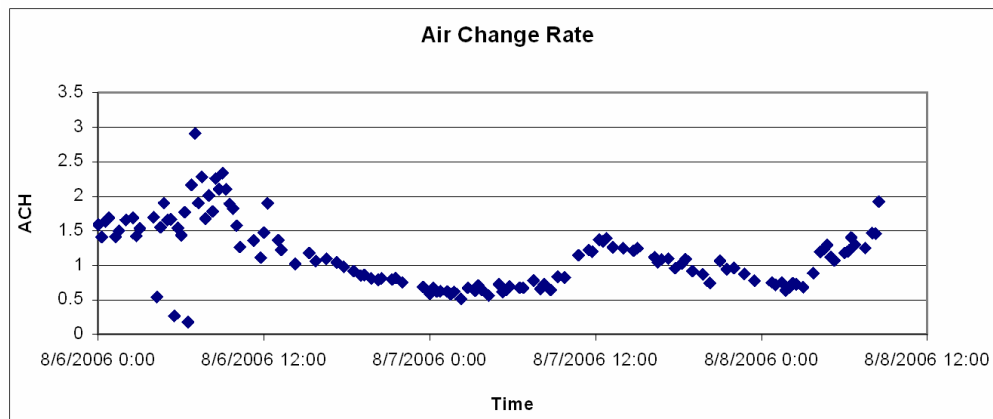
Figure 6.9 Air Exchange Rate Based on Measured Ventilation Data

From Figure 6.9, it can be seen that the infiltration rate varies from 0.5 to 2.5ACH during this two and a half day period, and most of the values are located between 0.5 and 1.5ACH, which is larger than the values predicted by the blower door measurement method and the CO_2 measurement for the summer. These results will be discussed in the following section.

6.6 Discussion

6.6.1 Infiltration Rate Estimated by Four Different Approaches

The IW infiltration rate has been analyzed by four different approaches in the previous sections. These approaches are the tracer gas method, the CO_2 concentration method, the blower door measurement method and the humidity data analysis method. Table 6.9 shows the IW infiltration ranges obtained from the four methods and their corresponding dates.

Table 6.9 Infiltration Analysis Results

Approach	Tracer Gas	CO_2 Concentration	Blower Door Measurement	Humidity Data Analysis
Infiltration Range	0.86-0.95	0.09-0.83	0.4-1.5	0.5-2.0
Applicable Dates	July, August	March	Year round	August

Because the infiltration is a function of the indoor and outdoor temperature difference and the wind speed, it varies from month to month. The applicable date in Table 6.9 means the date the infiltration was measured or calculated. In summer, the blower door measurement results (Table 6.8) are nearly consistent with the tracer gas measurement results, the CO_2 concentration results, and the humidity data analysis results. The summer infiltration rate ranges from 0.5 to 1.2. However, the results from the humidity data analysis seem to be larger than the results obtained from the CO_2 concentration measurements and the blower door tests. The reason is that the doors and windows might have been opened when the SEMCO unit was running. All spaces adjacent to the IW are unconditioned space during the summer. Additional moisture can be brought into the space when the doors and windows are open. Therefore, the calculated infiltration rates based on logged humidity dates would have been higher than the actual rates of infiltration from the outdoors. The CO_2 concentration method gave a relatively smaller infiltration rate, which may have been affected by the CO_2 given off by the plants inside the IW[2]. Also, if infiltration air comes from the plenum and third floor, the CO_2 concentration of the IW may be affected by the CO_2 concentration of the third floor air. The CO_2 concentration method tends to give a smaller infiltration value, because the CO_2 concentration of the third floor is higher than in the outside air.

6.6.2 Air Leakage from the Third Floor

During the blower door measurements, a significant amount of air was found to blow into the space from the IW plenum. By checking the plenum and third floor ceiling, it was found that the leaking air came from the third floor. Therefore, air leakage in the IW can be divided into two parts, the internal leakage from the third floor and external leakage from the outside air. In the winter, the conditioned third floor air leaking into the IW will either not affect the heating load if there is no difference between the air temperature of the IW and the third floor or reduce the heating load if the air temperature of the third floor is higher than the IW. In the summer, the stack effect drives the hot third floor air into the IW. The cooling load will then be larger than that considering only the thermal envelope air leakage. Because infiltration air from outside accounts for a significant part of the building heating and cooling load, the calibrated simulation of the IW would give some clues to the amount of outside air infiltration if the heating and cooling measurement data is available.

---

[2] The CO2 level given out or being eaten by the indoor plants has not been quantified and the effect of the plants on the indoor CO2 level is not quite clear at this time.
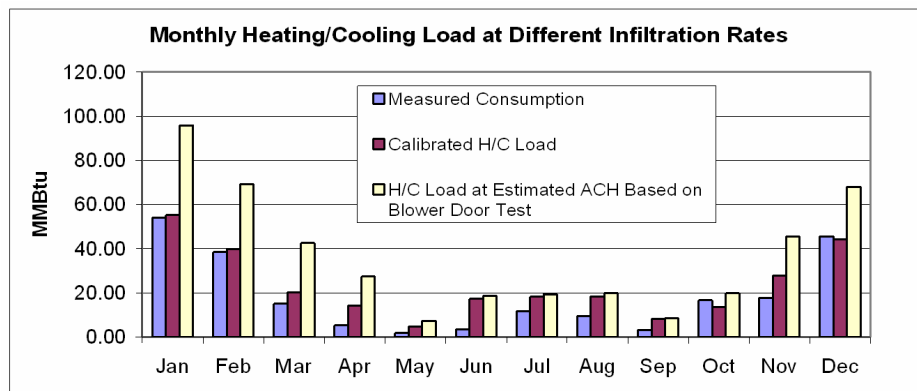
Figure 6.10 Monthly Heating/Cooling Load at Simulated and Blower Door Predicted Infiltration Rates

Chapter V described the calibrated simulation of the IW. Because the measured cooling data are not available, the calibration simulation of summer cooling is based on the estimated cooling loads reported by the IW in the 2003 project meeting. These estimated IW cooling loads are treated as measured loads and may not be reliable. Therefore, the calibration simulation will give a closer indication of the infiltration in winter than that it will give in summer. The heating and cooling loads at the infiltration rates estimated by the calibration and predicted by the blower door measurements are listed in Table 6.10. Figure 6.10 compares the monthly measured heating and cooling loads[3] with those of the calibrated infiltrations and estimated infiltrations based on the blower door measurements. From Figure 6.10, it can be seen that the heating loads at the infiltration rates predicted by the blower door measurements are much larger than the measured heating loads if all the infiltration air is assumed to be outside air. The simulation results mean that a significant part of the infiltration air does not affect the heating load of the IW. The difference between the infiltration predicted by the blower door measurement and the calibrated infiltration rate does not affect the heating load. This part of the infiltration can be considered to be the third floor conditioned air leaking into the IW. Therefore, it is believed that the calibrated infiltration rates are actually outside air exchange rates recorded during this period. The air leakage from the third floor may vary from 0.46 to 1.03ACH during the year. However, the temperature difference between the third floor and the IW should be much smaller than from the

---

[3] The measured cooling loads here are actually estimated loads. The simulated cooling loads do not match the measured cooling loads very well.

IW to the outside, so the actual air leakage from the third floor may be smaller than the range estimated above.

6.6.3 Possible Leakage Points

   The IW façade is a high quality product. The windows, doors, and roofs are all tight. However, several possible leakage sites in the IW envelope were identified by the site visit. The first is the joints between the metal roof and the walls. The seals at these joints may not be tight. Figure 6.11 shows a picture of one of the potential leakage sites. The second is the roof ventilators, as shown in Figure 6.12. The roof ventilators used to be directly open to the outside in order to balance the pressure difference. Now the ventilators are permanently closed and pinned. However, there is still a small gap between the ventilator damper and the damper frame on every ventilator. Some louvers behind the ventilator damper are not closed.

Figure 6.11 Potential Leakage Site-Joint Sections Between Metal Roof and Wall

   A significant amount of leaking air was found coming from the plenum through the gaps between the plenum floor tiles and the ventilation ducts. When the plenum air leaks into the IW, the third floor conditioned air leaks into the IW plenum through places where the air ducts and hot water pipelines penetrate the third floor ceiling. Figures 6.13, 6.14 and 6.15 show that a gap exists where the air duct and pipeline penetrate through the third floor ceiling.
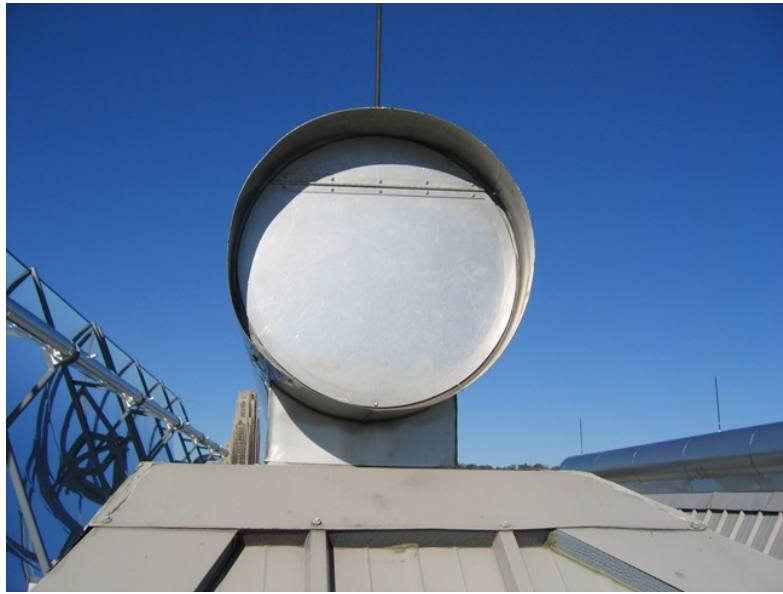
Figure 6.12 Potential Leakage Sites–Roof Ventilators

Figure 6.13 Potential Leakage Points - Where Ducts Penetrate the Third Floor Ceiling

Figure 6.14 Potential Leakage Points-Where Pipeline Penetrates the Third Floor

Figure 6.15 Potential Leakage Points-Drain Pipe Penetrates the Third Floor Ceiling

Table 6.10 Heating and Cooling Load at Calibrated Infiltration and Blower Door Predicted Infiltration

Month	Measured Consumption (MMBtu)	Air Change Rates Based on Calibrated DOE2 Simulation, (hr^{-1})	Simulated Monthly Heating and Cooling Load[4], (MMBtu/month)	Estimated Air Change Rates Based on Blower Door Measurement, (hr^{-1})	Simulated Monthly Heating and Cooling Load[5], (MMBtu/month)	Estimated Air Change Rates with Third floor, (hr-1)
Jan	54.20	0.46	55.26	1.49	95.87	1.03
Feb	38.55	0.4	39.86	1.4	69.15	1
Mar	15.13	0.2	20.22	1.29	42.52	1.09
Apr	5.33	0.16	14.3	1.15	27.34	0.99
May	1.81	0.12	4.72	0.94	7.19	0.82
Jun*	3.455	0.1	17.2	0.82	18.54	0.72
Jul*	11.746	0.1	18.16	0.75	19.34	0.65
Aug*	9.575	0.1	18.42	0.74	19.94	0.64
Sep*	3.257	0.3	8.33	0.76	8.44	0.46
Oct	16.58	0.4	13.594	1.05	19.8	0.65
Nov	17.72	0.46	27.74	1.34	45.44	0.88
Dec	45.63	0.5	44.12	1.36	67.94	0.86

*From June to September, the loads shown in the above table are cooling loads; from September to May, the loads shown in the above table are heating loads. There is no overlap between heating and cooling.

---

[4] Values in this column were simulated assuming the air change rates given in the third column from the left for each month
[5] Values in this column were simulated assuming the air change rates given in the fifth column from left for each month

6.7 Summary

To investigate the infiltration level of the IW, separate blower door measurements were made at the IW on Oct. 6th and 10th 2006. This chapter analyzes the blower door measurement results and estimates year-round IW infiltration levels by considering the factors of temperature difference and wind speed. The results show that the average IW infiltration may vary from 0.4ACH in the summer to 1.5ACH in the winter, which includes infiltration air from the outside and from the third floor.

This chapter also reviews the previous infiltration study of the IW that used the tracer gas method, reanalyzes the CO_2 concentration data, and evaluates the infiltration by using logged humidity data. The results for the IW infiltration range from 0.78-1.31ACH by the tracer gas method, 0.09-0.83ACH by the CO_2 concentration method, and 0.5-2.0ACH from the logged humidity data.

A significant portion of the leaking air has been found to come from the plenum and the third floor. A simulation study of the IW using DOE2.1 identified an estimated rate of outside air leakage, based on a calibration of the simulation to a measured amount of heating consumption data. Combining the results of the calibrated DOE2 simulation and the blower door measurement, the third floor air leakage into the IW can be estimated. This process gives outside air leakage ranging from 0.1-0.5ACH, while the third floor air leaking into the IW may range from 0.46-1.03ACH, or less.

Some possible leakage points were discovered during the site visit. The places where the ducts and pipelines penetrate the third floor ceiling are major sources of third floor air leaking into the IW. The roof ventilators and joint sections between the roof and walls are the main sources of outside air leakage.

CHAPTER VII

THE PERFORMANCE STUDY OF THE SENSIBLE HEATING AND COOLING
SYSTEM INTEGRATED WITH A SOLID DESICCANT VENTILATION UNIT

7.1 Introduction

Radiant heating and cooling gained a reputation of energy efficiency for the following reasons: first, it reduces the fan power consumption which normally accounts for 25%-30% of the total building energy consumption in air heating and cooling systems. Second, it allows a higher chilled water supply temperature to meet the space sensible load. The chilled water temperature can be 55°F or higher, while it is around 40°F to 50°F for the conventional air heating and cooling system. The general rule of thumb is that a one degree Fahrenheit increase in supply temperature corresponds to a decrease in compressor electricity consumption of 1.7% in chillers (Liu et al., 2002). Third, radiant heating and cooling reduces the heat dissipated by air supply fans within the conditioned space. A radiant heating and cooling system is normally used in parallel with a dedicated outside air system. This configuration decouples the sensible and latent functions of an HVAC system. The indoor humidity ratio can be controlled by the dedicated outside air system, while a conventional all-air VAV system only has a limited capability to remove the moisture from the space. Some researchers (Mumma et al. 2001a, 2001d, 2002; Brunk 1993; Behne 1995; Niu et al. 1995, Simmonds 1994) suggest that this decoupled sensible/latent configuration improves the indoor comfort level.

Many studies have been carried out to compare the energy efficiency of radiant heating and cooling with a conventional all air VAV system. Roth et al. (2002) reported an analysis comparing the energy consumption of a conventional VAV system with a radiant ceiling with a dedicated outside air system (DOAS) and found that a radiant ceiling reduces cooling energy by 15% to 20%, overall. Jeong et al. (2003) compared the simulation results for a 3200 ft^2 academic office with a radiant ceiling and dedicated ventilation system with an all-air VAV system. They reported the chiller energy consumption of the radiant system to be 25% less than the VAV case, and also reported that the radiant cooling plus the DOAS system could save 42% of the total primary energy consumption annually, as compared with the VAV system. Stetiu (1999) simulated a radiant cooling system in a 700 square meter building and reported 30% energy savings in a warm and dry area. No yearly measured consumption has so far been reported to confirm these savings.

The above simulations are all based on optimal system configurations and operating conditions. This chapter presents a simulation study of an integrated heating and cooling system consisting of radiant mullions, radiant panels, fan coils and a desiccant ventilation unit based on the actual system in the Intelligent Workspace. It compares the energy consumption of the integrated system using an active desiccant ventilation unit or a passive desiccant ventilation unit with the energy consumption of a single duct VAV air heating and cooling system based on similar conditions. The occupancy, lighting and equipment load assumptions are the same as the assumptions in Chapter V (Section 5.2). The primary assumptions in the single duct VAV system are: design air flow: 1cfm/ft^2; minimum air flow ratio: 0.3; no terminal reheat in summer; deck setting temperature range: 55˚F~60˚F (depending upon outside air conditions); indoor air temperature setting: 72˚F in winter and 73˚F in summer. The OA rate for both the active desiccant system and the passive desiccant system is 1000CFM, while it is 10% of the supply air flow rate for the VAV system.

7.2 Sensible Heating and Cooling Devices in the IW

The current IW energy distribution system is shown in Figure 2.1. This system includes radiant mullions, radiant panels, cool waves (a type of sensible cooling device), and fan coils which are proposed to be installed in the near future. All the heating and cooling devices in the IW are designed to meet only sensible loads. The latent load is left to the ventilation system. The chilled water currently comes from the campus loop and is supplied by the building chilled water pump. Hot water is supplied by the hot water pump and the steam-water heat exchanger in the basement. The hot water and chilled water pumps are building pumps which supply water for the whole building use. The IW has a mullion pump and a fan coil pump to supply chilled water and hot water for the building use. The parameters and assumptions made for each device in the simulation study are described in the following sections.

7.2.1 Mullions

There are 104 radiant mullions in the south and north zones of the IW. These mullions are divided into 26 groups. Each group is controlled by one control valve. The radiant mullions are the primary heating and cooling devices in this space. This simulation assumes that the upper limit of the hot water supply temperature is 125°F, and the lower limit of the chilled water supply temperature is 55°F. The heating and cooling heat input is adjusted by controlling the supply water temperature.

7.2.2 Radiant Panels

There are four groups of suspended ceiling radiant panels in the IW. There is no top insulation on the top of these radiant panels. These radiant panels can meet both heating and cooling loads of the space. The total sum of the areas of these radiant panels is approximately 354 ft^2. Radiant panels are assumed to be used whenever the mullions cannot meet the heating and cooling loads of the spaces. The inlet water temperature is assumed to be the same as that of the mullions.

7.2.3 Cool Waves

There are ten cool waves located in the north zones. Nine of them can be used. Cool waves can only meet sensible cooling loads. The specific cooling capacity is 32W/K. The oscillating fan power is 20W per fan. The cool waves are the last choice for meeting the cooling load after the fan coils because the cool waves are located in the unoccupied meeting room in this office complex.

7.2.4 Fan Coils

15 VKB floor fan coils, 6 VKD ceiling fan coils, and 1 FVD fan coil have been proposed for installation in the near future. The specifications of the VKB and VKD units are shown in Table 7.1. The fan coils are the third device in the order of meeting the building heating and cooling loads. The Qk/Δt is the specific cooling, and the Qh/Δt is the specific heating with the unit of W/K. They are rated at their different design flow rates. The design flow rate for the VKB fan coil is 200 kg/h (cooling) and 100 kg/h (heating). The design flow rate for the VKD fan coil is 300 kg/h (cooling) and 100 kg/h (heating).

Table 7.1 Specification Data of Fan Coil Units

	VKD Fan Coil			VKB Fan Coil		
Fan Speed	Qk/Δt	Qh/Δt	Power, W	Qk/Δt	Qh/Δt	Power, W
1	51	35	16	45	38	15
2	78	42	24	55	44	17
3	95	46	32	64	50	20
4	104	49	40	71	57	22
5	116	52	57	80	62	27

7.2.5 Pumps

There are two types of pumps in this system. One is building pumps like the building hot water and chilled water pumps. These pumps were sized for the whole building rather than for the IW. The other is the equipment pumps such as the mullion pump, fan coil pump, cool wave pump, and radiant panel pump. These pumps were sized only for the IW. The power consumption of the second type of pump is considered in the simulation processes. The mullion pump, the fan coil pump, the cool wave and radiant panel pumps are assumed to have 30 feet of pressure head based on loop resistance calculations. The operational flow rate for the mullion pump is 24gpm. The operational flow rate for the fan coil pump is 22gpm (4800lb/hr) in cooling mode, and 9.3gpm (2100kg/hr) in heating mode. The pump power is a product of the pump head and the pump flow rate. The overall efficiency of the pump and pump motor is assumed to be 0.7.
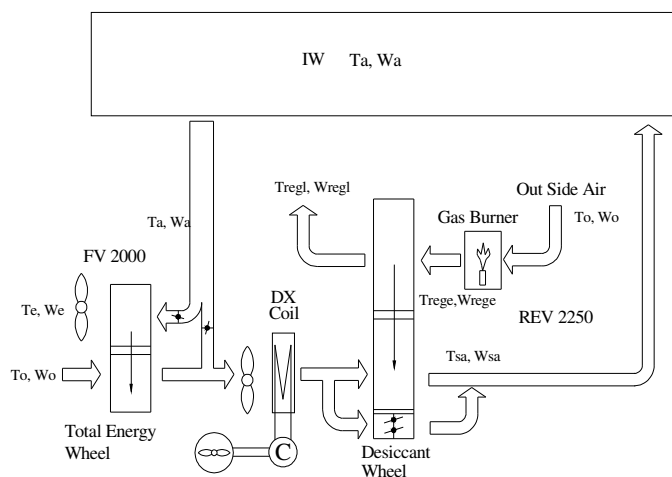
Figure 7.1 The Active Desiccant Ventilation System

7.3 System Simulation of Mullions, Radiant Panels, Fan Coils and Cool Waves with an Integrated Active Desiccant Ventilation Unit

A SEMCO REV2250, an active desiccant ventilation unit with a design flow rate of 2250CFM, combined with a FV2000 unit, an enthalpy wheel with a design flow rate of 2000CFM, is currently being used in the IW as the ventilating air conditioning device. The system diagram is shown in Figure 7.1. The system consists of an enthalpy wheel, a heat pump,

and an active desiccant wheel. The active desiccant wheel uses natural gas for desiccant regeneration, while the enthalpy wheel is a passive desiccant wheel.

7.3.1 Active Desiccant Ventilation System

The available information about the active desiccant system is the online control diagram and two weeks of logged data obtained during the summer and winter. No further detailed information was available for this active desiccant system. According to the online control diagram, the supply air temperature is assumed to be 60ºF in the summer and 72°F in winter. The following assumptions have been made in the simulation processes:

A. The active ventilation system supplies 3000CFM of conditioned air with 1000CFM of OA in the summer, while it supplies 2000CFM of conditioned air with 1000CFM of OA in the winter.

B. In the summer, the supply air humidity is a function of the outdoor humidity ratio, which can be obtained from empirical data.

C. The regeneration burner is assumed to have an efficiency of 0.9. The enthalpy recovery efficiency is assumed to be 75%, based on the SEMCO product manual.

D. Electricity consumption of the heat pump is obtained by a correlation between the total power consumption and the sensible load, and the latent load taken by the heat pump DX coil. The correlations are obtained by analyzing the recorded data.

E. In winter, the gas burner is considered to be the primary heating device.

F. In winter, if the gas burner is used for heating, gas consumption varies with the temperature and humidity differences across the desiccant wheel.

G. SEMCO combined units consume both electricity and thermal energy. Electricity consumption includes the: SA fan, EA fan, outdoor fan, compressor, FV wheel drive and active wheel drive. Thermal energy is produced from gas burning.

7.3.2 Calculation Flow Chart and Control Logic

The calculation flow in the integrated system simulation is shown in Figure 7.2. The simulation uses a building-sensible load and a latent load which was obtained from a DOE2 calibrated simulation as the input, combining with the office schedule and ventilation schedule. The simulation program decides the heating or cooling mode when reading the hourly load of a

year. In heating mode, the program calls the SEMCO unit first. The building latent load is taken by the SEMCO ventilation units, and the difference between the building sensible load and the sensible load taken by the ventilation unit is left to the mullions, radiant panels and fan coils. The supply water temperature is adjusted to make the heating input of these devices match the space sensible load. All pump power and SEMCO unit electricity consumption is calculated during the simulation processes. SEMCO units normally do not take sensible loads in the heating mode because the temperature of the supply air is assumed to be the same as room air temperature. In cooling mode, the SEMCO ventilation unit will take all latent loads and part of the sensible load at a supply air temperature of 60ºF. The remaining sensible load is taken by the mullions, radiant panels, fan coils and cool waves, in the order of the priority. The cooling input of these devices is adjusted by the supply water temperature. In summer, the space cooling load is taken by one 10-ton chiller, rated at 1kW/ton. In the summer, the program outputs hourly and monthly sensible loads, latent loads and electricity loads met by the sensible system and the ventilation system, individually. The hourly outputs are converted into a daily output by a separated code. The following logic is assumed in the calculation process:
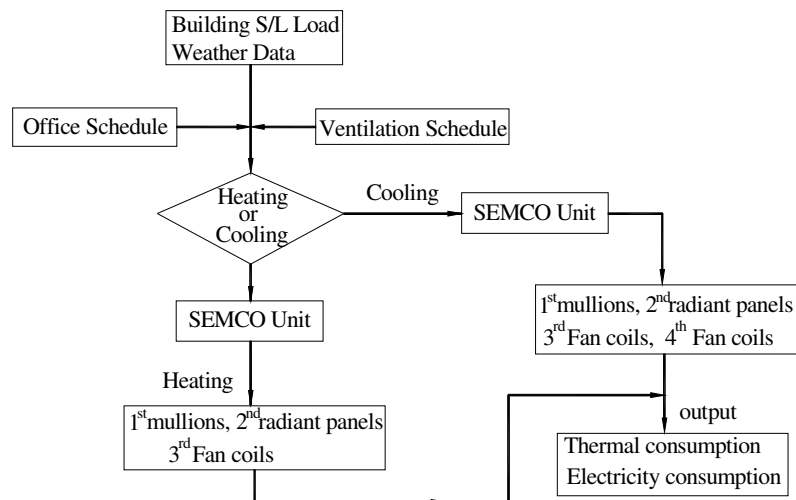
Figure 7.2 Integrated System Simulation Flow Chart

A.   Whenever the outside temperature is lower than 60ºF in the cooling season and higher than 65ºF in the heating season, the SEMCO is turned off. Operable windows are used to provide fresh air at this time. The SEMCO unit is off when the office is not in its normal work schedule.

B.   Whenever the mullions, radiant panels or cool waves are on, the mullion pump must be on, and the pump power consumption will be calculated.

C.   Whenever the fan coils are on, the fan coil pump will be on.

D.   A generic reciprocating air-cooled chiller model (Jeong et al. 2003) is used in the integrated system simulation. A 10-ton chiller is assumed based on the maximum building cooling load from the DOE2.1 simulation. The rated power input of the variable speed compressor is assumed to be 10KW.

7.3.3 Simulation Results

The simulation results of the integrated system with an active ventilation unit are shown in Figures 7.3, 7.4, 7.5 and Table 7.2. Figure 7.3 shows that the sensible load met by the energy distribution system is a function of the OA temperature. In the simulation process, the indoor air temperature is set to 72°F. The sensible heat is actually a function of the temperature difference between the indoor and outdoor air. The data are scattered because of the building operation schedule, solar radiation and the system schedule.
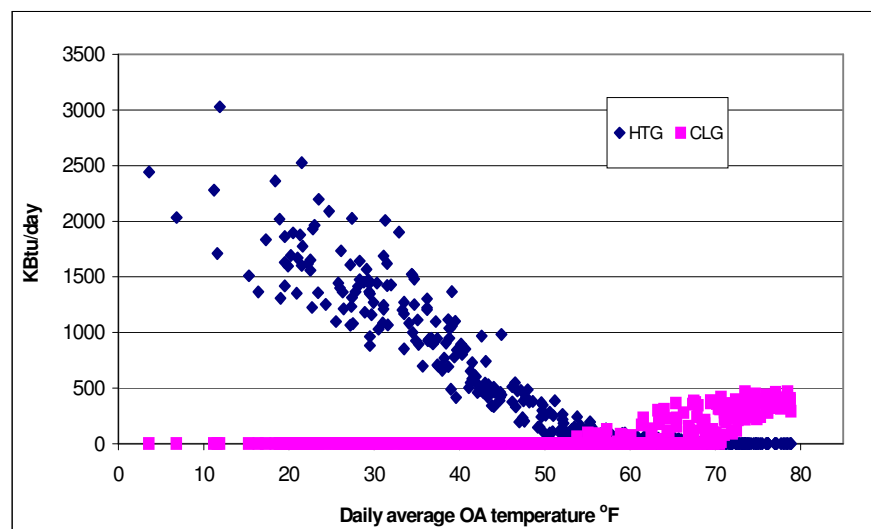
Figure 7.3 Daily Sensible Heating and Cooling Load Taken by Sensible Heating and Cooling System

Figure 7.4 shows the sensible and latent loads met by the desiccant ventilation system. The ventilation system does not meet any sensible load of the space at lower outside temperatures

during the winter because the gas burner is assumed to be heating the OA to the space air temperature of 72ºF. When the supply ventilation air temperature is the same as the space air temperature, the ventilation air does not meet any sensible load in the space, as shown in Figure 7.4. The latent load met by the active ventilation system increases as the OA temperature increases because the absolute humidity ratio normally increases as the OA temperature increases during the summer.
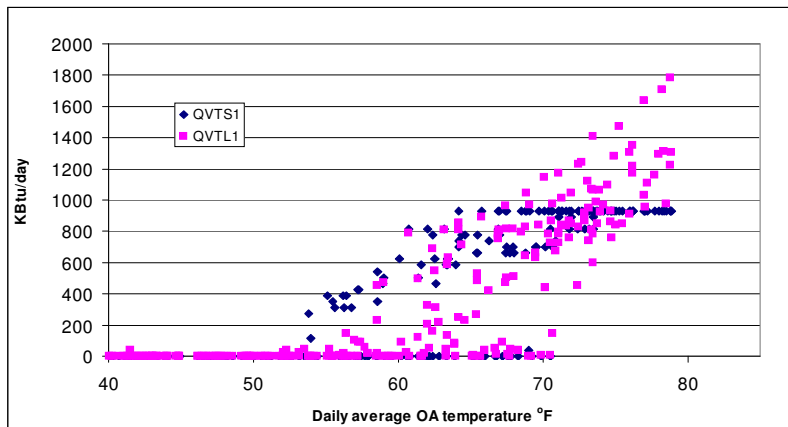
Figure 7.4 Daily Sensible and Latent Loads Met by the Active Desiccant Ventilation System
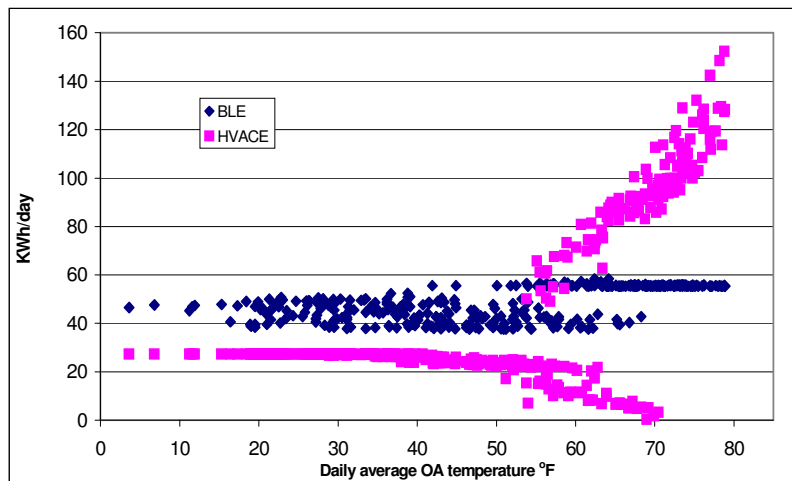
Figure 7.5 Daily Building Lighting and Equipment Load vs. HVAC Load Met by the Sensible Heating and Cooling System with an Active Desiccant Ventilation Unit

Figure 7.5 compares the building lighting and equipment load with the HVAC system (including pumps, fans, and chillers) load. This figure indicates the building L&E load is relatively constant. The HVAC electricity load is relatively constant in the winter because the mullion pump is always on whenever the OA temperature is lower than 40°F. In the summer, the HVAC load has two patterns. One is that the ventilation system and chiller is on, and the other is that the ventilation system is off and the chiller is standby during normal office hours.

Table 7.2 shows the simulated monthly load for the integrated system. The yearly integrated system electricity load is 30,717 kWh; the yearly total thermal load is 348.46MMBtu. The primary energy consumption for this system is 783.30MMBtu/year.

Table 7.2 Simulation Results of the IW Sensible Heating and Cooling System with an Integrated Active Desiccant Ventilation Unit

MONTH	Integrated System Thermal Load*, MMBtu	Integrated System Electricity Load, kWh	Integrated System Electricity Load Excluding Ventilation, kWh	Chiller Electricity Load, kWh	Integrated System Electricity Load including Chiller, kWh	Integrated System Primary Energy Consumption, MMBtu
Jan	57.1	1,985	1,334	-	1,985	97.65
Feb	44.2	1,669	1,081	-	1,669	76.90
Mar	21.0	1,652	1,051	-	1,652	46.47
Apr	15.0	1,575	1,008	-	1,575	37.70
May	5.7	1,722	1,355	-	1,722	27.40
Jun	27.6	3,729	1,364	396	4,124	77.17
Jul	29.8	4,000	1,423	418	4,418	82.91
Aug	30.4	4,080	1,391	414	4,494	84.37
Sep	25.4	3,362	1,352	338	3,700	69.87
Oct	13.9	1,637	1,106	-	1,637	37.03
Nov	30.7	1,727	1,103	-	1,727	60.19
Dec	47.6	2,015	1,364	-	2,015	85.64
Total	348.46	29,152	14,929	1565	30,717	783.30

*Summer cooling load is counted as the electricity and not the thermal load, because chilled water is produced by an electric chiller.

The supplied ventilation air humidity can be adjusted by controlling the regeneration air temperature, the ratio of bypass air, and many other measures offered by the manufacturers. The supply air humidity ratio can be controlled in a flexible way. Figure 7.6 shows the supply air humidity ratio data across the desiccant wheel during the week of August 12 to August 19, 2006.

The supply air humidity ratio can be seen as a function of the OA humidity ratio, which varies from 0.0065 lb/lb to 0.0075 lb/lb. The room air humidity ratio (the return air humidity ratio) is controlled to be below 0.011 lb/lb (RH 55%, dew point 57ºF). The sensible heating devices in the IW can be operated safely at these humidity ratios. The correlation of the supply air humidity ratio, W_{sa}, and outside air humidity, W_{oa}, can be written as the following equation, based on the trend line in Figure 7.6.

$$W_{sa} = 1313.7 * W_{oa}^{3} - 83.889 * W_{oa}^{2} + 1.6954 * W - 0.0037 \qquad (7.1)$$
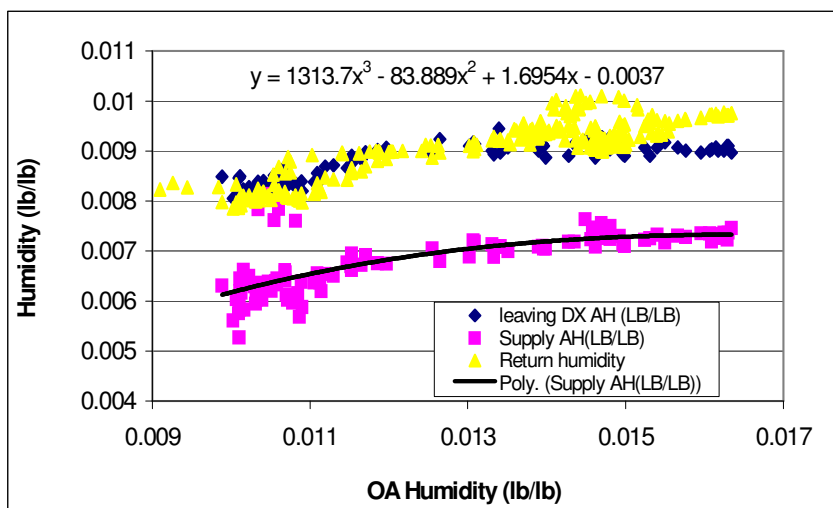
Figure 7.6 Supply and Return Air Humidity Ratio of Active Desiccant System (One Week of Data)

7.4 System Simulation of Mullions, Radiant Panels, Fan Coils and Cool Waves with an Integrated Passive Desiccant Ventilation Unit

Passive desiccant ventilation systems are often recommended for use with radiant or sensible cooling devices in the literature (Jeong et al. 2003, Niu et al. 2002, Shank and Mumma 2001). Single wheel or double wheel ventilation systems are commercially available. The previous ventilation system used by the IW was a single wheel desiccant ventilation system. The benefits of the single wheel passive system are a lower initial cost and a higher energy efficiency as compared with an active desiccant ventilation system, because there is no additional heat input

needed for desiccant wheel regeneration. However, the passive desiccant system needs a post cooling coil and the dew point of the supply air is actually related to the dry bulb temperature of the supply air in summer. The capability of removing moisture depends on the humidity ratio (or dew point) of the supply air and the flow rate of the supply air. The conditioned space needs to be relatively tight. Otherwise, the indoor humidity ratio cannot be maintained at a level low enough to ensure that no condensation collects on the radiant cooling devices, as discussed in Chapter V.

7.4.1 Single Wheel Passive Desiccant Ventilation System

In order to compare the energy consumption of the integrated radiant/sensible cooling system with an active desiccant ventilation unit to the consumption of the system with a passive ventilation unit, the IW energy distribution system is also simulated with a single wheel passive desiccant ventilation system. The simulated single wheel desiccant system (as shown in Figure 5.1) is based on the previous ventilation system used by the IW, but with several modifications. The outdoor air first passes through the passive desiccant wheel, then mixes with 67% return air. The mixed air passes through the DX cooling coil and the heating coil, and then goes into the space. The DX coil is assumed to be the same one as that which is in the active desiccant ventilation unit. The hot water is supplied by the campus loop. There is no overlap of heating and cooling in summer and winter. The chilled water in the energy distribution system in the IW space is assumed to be supplied by one independent 10 ton chiller, in order to allow an accurate comparison of the electricity consumption. The chilled water supply temperature is adjusted according to the space cooling load. Several assumptions have been made as follows:

A. In summer, the passive desiccant system supplies 3000CFM of air to the IW, which includes 1000CFM of outdoor air and 2000CFM of return air. The supply air temperature is set to 54ºF, with a humidity ratio of 0.009lb/lb.

B. In winter, the passive desiccant system supplies 1000CFM of outdoor air to the IW without mixed return air. The supply air temperature is set at 72ºF.

C. The indoor humidity ratio is calculated based on the model developed in Chapter V. The infiltration rate is considered to be a function of both the wind speed and the temperature difference between the indoors and the outdoors. According to the calibrated simulation analysis outlined in Chapter VI, the equivalent IW leakage

area is considered to be one third of the 1680 in^2 determined from the blower door measurements.

D.   The enthalpy wheel sensible and latent heat recovery efficiencies are considered to be 0.75.

E.   A generic reciprocating air cooled chiller model (Jeong et al. 2003) is used in the integrated system simulation. A 10 ton chiller is assumed based on the maximum building cooling load from the DOE2.1 simulation. The power of the variable speed compressor is rated to be 10kW, based on a power ratio of 1.0 kW/ton.

7.4.2 Calculation Flow Chart and Control Logic

The calculation flow and control logic is the same as in Section 7.3.2.

7.4.3 Simulation Results

Figure 7.7 shows the sensible heating and cooling load met by the space heating and cooling devices. Compared to Figure 7.3, the sensible cooling load on the energy distribution system is slightly lower. The reason for this is that the supply air temperature for the active desiccant ventilation system is 60ºF, and it is 54ºF for the passive desiccant ventilation system. The supply air temperature is reheated slightly by the regeneration burner in Figure 7.1, while there is no reheat in the passive ventilation system shown in Figure 5.1, in the summer.
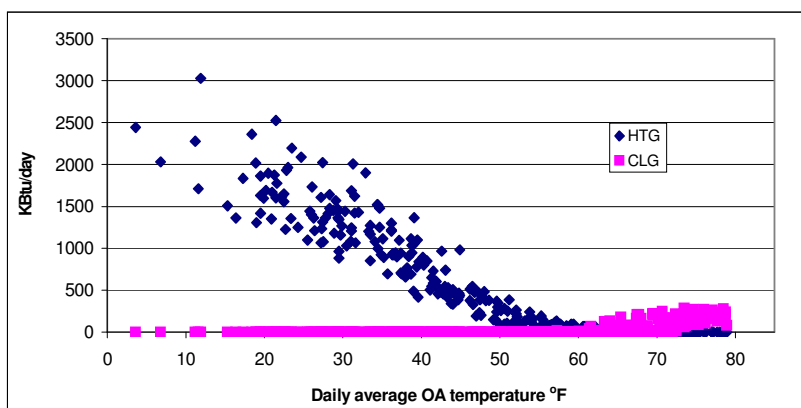
Figure 7.7 Daily Sensible Heating and Cooling Loads Met by Sensible Heating and Cooling Devices
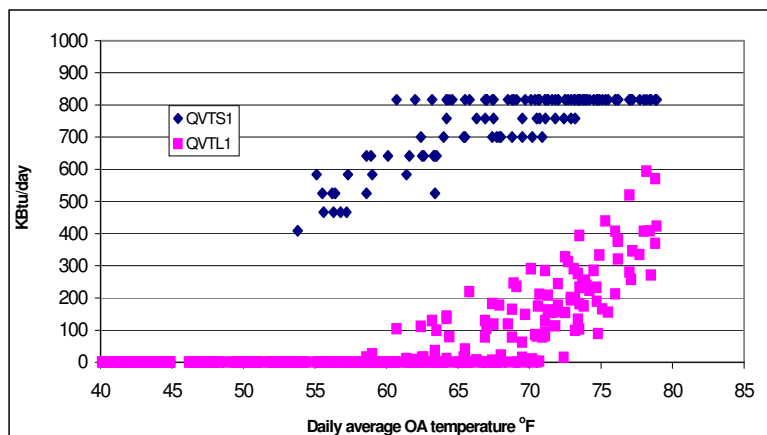
Figure 7.8 Daily Sensible and Latent Loads Met by the Passive Desiccant Ventilation System

Figure 7.8 shows the sensible and latent loads met by the passive ventilation system. Compared to Figure 7.4, the latent load met by the passive desiccant system is much lower than that of the active desiccant system. The reason for this is that the supply air humidity for the active system ranges between 0.0065lb/lb and 0.0075 lb, while for the passive system, it is measured around 0.009lb/lb. The supply air volume flow rate for these two systems is the same: approximately 3000CFM.

Figure 7.9 shows the building lighting and equipment loads and the HVAC load, as a function of the outside air temperature. As compared to Figure 7.5, the building L&E and HVAC profiles for these two systems are similar, except that the HVAC load of the passive desiccant system is smaller than that of the active desiccant system in the winter. The reason for these differences is that the supply air flow is 2000CFM for the active desiccant system, including 1000CFM of return air, while it is 1000CFM of OA only for the passive desiccant system.

Table 7.3 shows the simulated monthly load for the integrated sensible heating and cooling system with a passive desiccant ventilation unit. The yearly integrated system thermal load is 214.37MMBtu, the yearly electricity is 30,904kWh, and the primary energy consumption for this system is 657.11MMBtu/year.
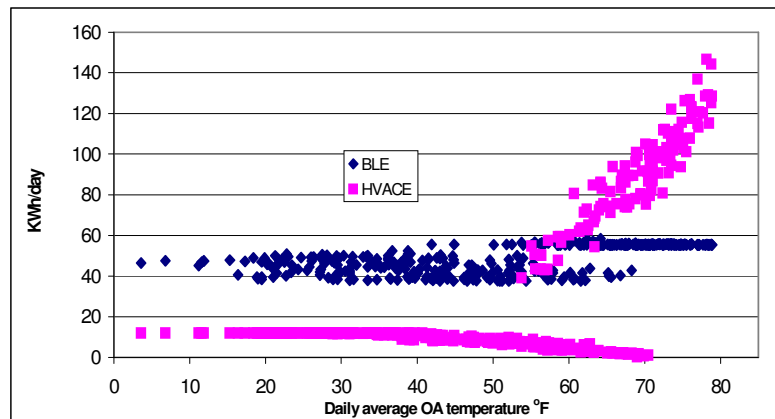
Figure 7.9 Daily Building Lighting and Equipment Load vs. the HVAC Load of the Sensible Heating and Cooling System with an Active Desiccant Ventilation Unit

Table 7.3 Simulation Results of the IW Sensible Heating and Cooling System with an Integrated Passive Desiccant Ventilation Unit

MONTH	Integrated System Thermal Load*, MMBtu	Integrated System L&E, kWh	Integrated System L&E Excluding Ventilation, kWh	Chiller Electricity Load, kWh	Integrated System, L&E plus Chiller, kWh	Integrated System Primary Energy, MMBtu
Jan	53.6	1,833	1,656	0	1,833	93.48
Feb	41.9	1,527	1,367	0	1,527	74.26
Mar	23.0	1,496	1,332	0	1,496	48.67
Apr	15.2	1,388	1,234	0	1,388	36.89
May	3.7	1,852	1,752	0	1,852	27.17
Jun	0	4,016	1,708	354	4,370	52.50
Jul	0	4,289	1,767	373	4,662	56.01
Aug	0	4,410	1,775	371	4,780	57.43
Sep	0	3,634	1,711	283	3,916	47.05
Oct	10.3	1,524	1,379	0	1,524	32.09
Nov	25.8	1,677	1,507	0	1,677	54.56
Dec	40.8	1,880	1,703	0	1,880	77.00
Total	214.37	29,525	18,890	1380	30,904	657.11

*Summer system cooling load is counted as electricity load and not thermal load, because the chilled water is produced by an electric chiller.
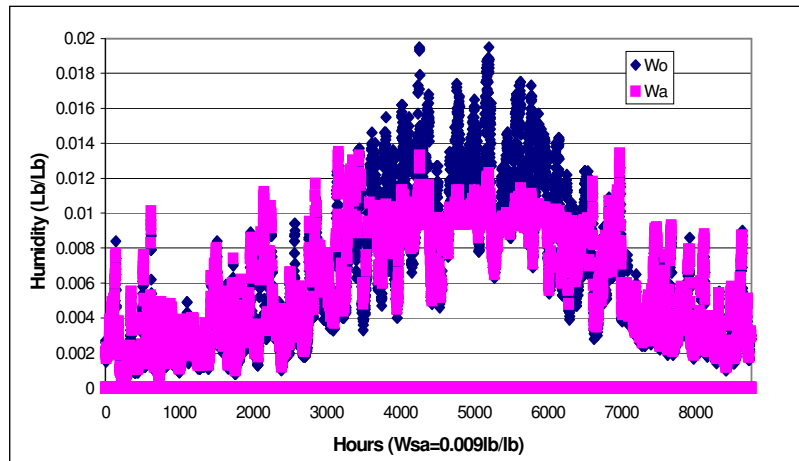
Figure 7.10 Hourly Indoor Humidity Ratio During Passive Desiccant Ventilation System Operation

The indoor humidity ratio is a major concern when applying a passive desiccant ventilation system. As the study of Chapter V demonstrates, this ventilation system cannot work very well in a leaky space. The indoor humidity ratio is also simulated based on the estimated infiltration calculated in Chapter VI. The results are shown in Figure 7.10. During most of the operating hours, the indoor humidity ratio is less than 0.012 lb/lb (RH 65%@75°F DBT), which is within the upper limit of the ASHRAE comfort zone. The chilled water supply temperature is adjusted between 55°F and 70°F, based on the cooling load of the space. Because the ventilation unit supplies 55 °F cool air to the IW, which already meets part of the cooling load, the cooling load left to the radiant mullions and fan coils is not significant. The supply chilled water temperature can be slightly higher and can vary between 57°F and 70°F. The space dew point and supply water temperatures are plotted in Figure 7.11. From Figure 7.11, it can be seen that the space dew point temperatures are lower than the chilled water supply temperature most of the time. The total number of hours when condensation is possible is 28 hours in a four month long summer season.
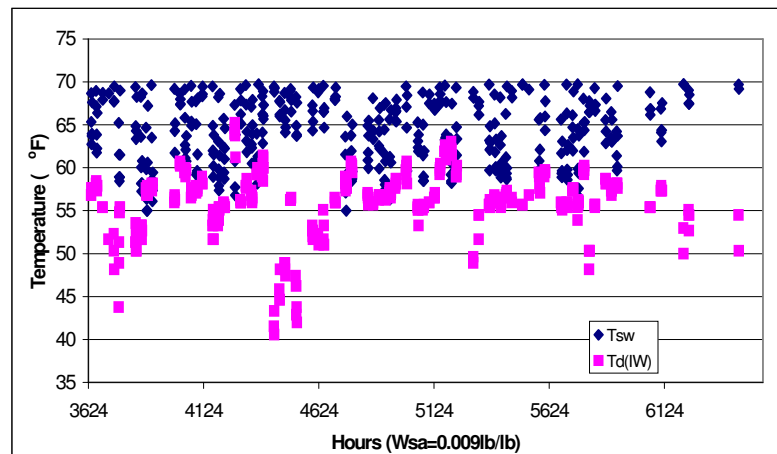
Figure 7.11 Hourly Indoor Dew Point (Td) and Supply Chilled Water Temperature(Tsw) During Passive Desiccant Ventilation System Operation

7.5 Discussion

7.5.1 Thermal and Electric Loads of Air Heating and Cooling Systems

In order to compare the performance of the sensible heating and cooling system with the air heating and cooling system, a single duct VAV system was simulated using DOE2.1 under the same infiltration level, operating schedule and OA flow. The major assumptions for the air system simulation are listed in Section 7.1. Figure 7.12 shows the heating and cooling loads of a single duct VAV system. As compared with Figure 7.3 and 7.7, the cooling loads of the single duct VAV systems in Figure 7.12 are higher than the two former integrated systems. The sensible heat recovered by the enthalpy wheel contributes to the difference. Also, the loads in Figure 7.12 include both sensible and latent loads, while the loads in Figures 7.3 and 7.7 only include the sensible load. The building lighting and equipment loads of the single duct VAV system in Figure 13 have the same pattern as both desiccant systems, with one minor difference. When the OA temperature is higher than 40°F, the HVAC load of the air system is even lower than the active desiccant system shown in Figure 7.9, because the fan power consumption is lower at the lowest heating load for the VAV air system. The active desiccant ventilation system runs at a constant 2000CFM in winter. There may not be a significant difference between the air heating systems and the integrated desiccant ventilation systems at a low heating load. Table 7.4 shows the simulated monthly load of a single duct VAV system. The annual primary energy consumption for this system is 741.44MMBtu

Table 7.4 Simulation Results of a Single Duct VAV Air Heating and Cooling System

MONTH	Qcooling MMBtu	Qheating MMBtu	Air Heating System Electricity kWh	Air Heating Chiller Electricity, kWh	Air Heating Electricity Load Including Chiller, kWh	Air heating, Thermal, MMBtu	Air heating, Primary Energy, MMBtu
Jan	0	65.354	2090	0	2090	65.354	112.25
Feb	0	50.877	1699	0	1699	50.877	88.25
Mar	0	29.035	1622	0	1622	29.035	58.20
Apr	0	20.586	1506	0	1506	20.586	45.54
May	0	6.828	2016	0	2016	6.828	33.32
Jun	28.01	0	2931	1580	4511	0	54.20
Jul	29.31	0	3029	1690	4719	0	56.69
Aug	30.31	0	3041	1664	4705	0	56.53
Sep	13.30	0	2295	1097	3392	0	40.75
Oct	0	15.179	1628	0	1628	15.179	39.80
Nov	0	33.862	1747	0	1747	33.862	66.14
Dec	0	49.472	1982	0	1982	49.472	89.77
Total	100.92	271.2	25,586	6,031	31,617	271.2	741.44
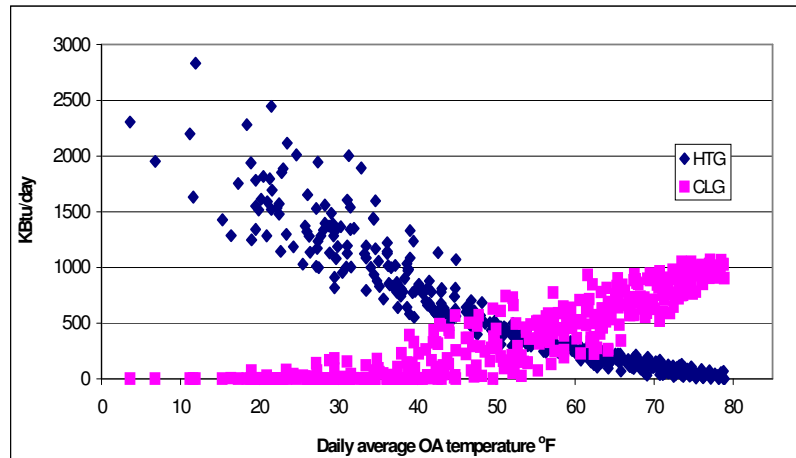
Figure 7.12 Heating and Cooling Loads of the Single Duct VAV System
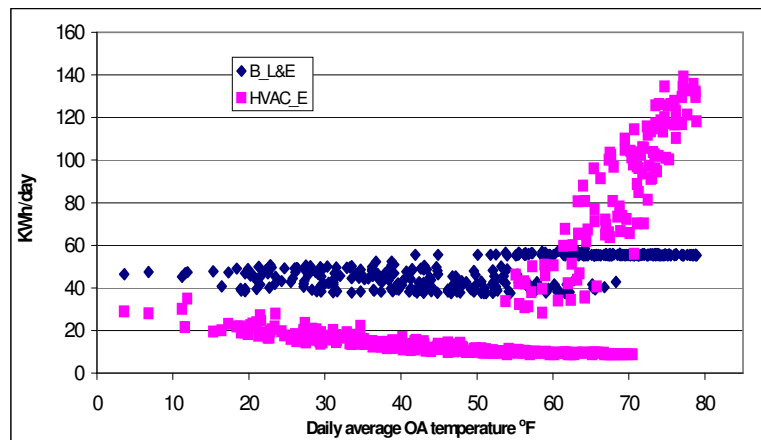
Figure 7.13 Building Lighting and Equipment Loads and HVAC Equipment Load of the Single Duct VAV System
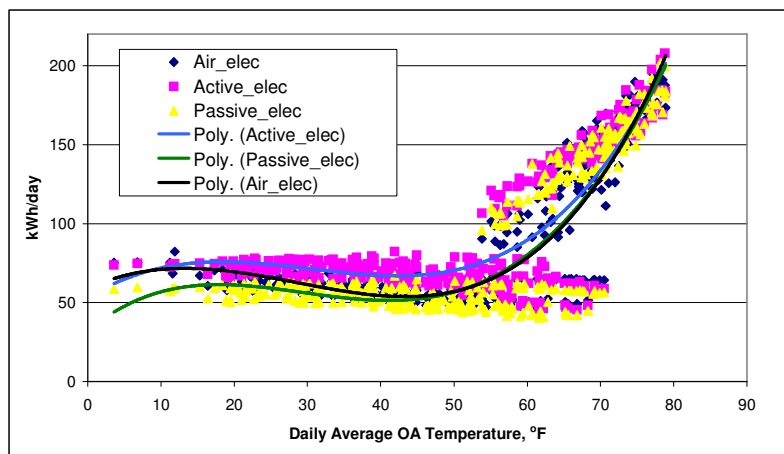
Figure 7.14. Comparison of Total Electricity Loads of Three Different Systems

7.5.2 Total Electricity Load and Primary Energy Consumption

Figure 7.14 compares the daily electricity loads of three different systems. The daily total electricity patterns are similar. The peak daily electricity load of the integrated active desiccant system in summer is slightly higher than that of air heating and the integrated passive desiccant system, because the auxiliary motor load (comprised of fan motors, a compressor motor, and the wheel driving motors) in this system is higher than in the other two. In order to compare the energy efficiency of these three systems, the electricity load and the thermal load of the three

systems are converted to the primary energy consumption by assuming an electricity generation and distribution efficiency of 0.284 (EIA, Annual Energy Outlook, 2006) and a boiler efficiency of 0.75 (Zhang and Niu, 2003). Figures 7.15 and 7.16 compare the daily thermal loads, which include hot water consumption in winter and year round gas consumption, and the primary energy consumption of the three systems. From Figure 7.15, it can be seen that the thermal load of the integrated active system steeply increases when the daily average temperature is higher than 55ºF. The reason is that the gas consumption needed for regeneration increases in order to remove the moisture inside the IW space. In Figure 7.16, the peak primary heating energy load of air heating and cooling is higher than the other two systems. When the OA temperature is higher than 55ºF, the primary energy consumption of the integrated active system is much higher than the other two systems, because of the regeneration thermal consumption of the active desiccant unit.
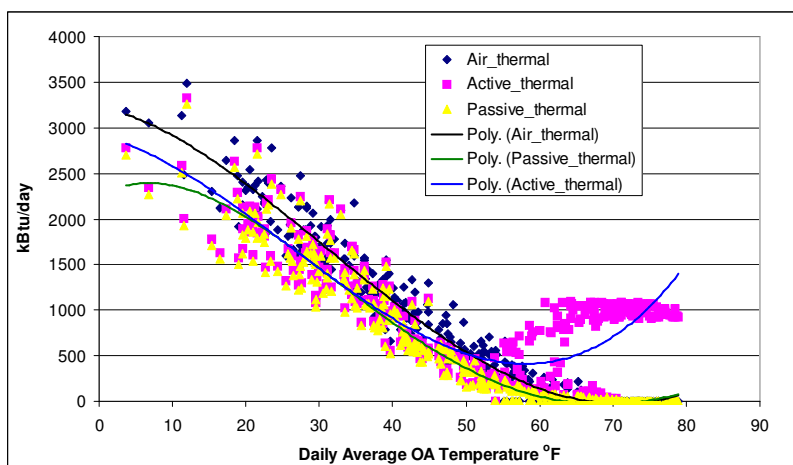
Figure 7.15 The Comparison of Total Thermal Energy Loads of Three Different Systems
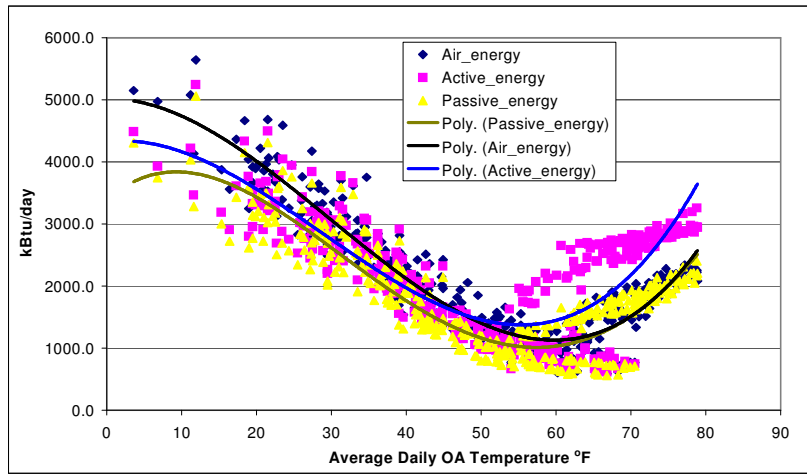
Figure 7.16 Comparison of Total Thermal and Primary Energy Consumption of Three Different Systems
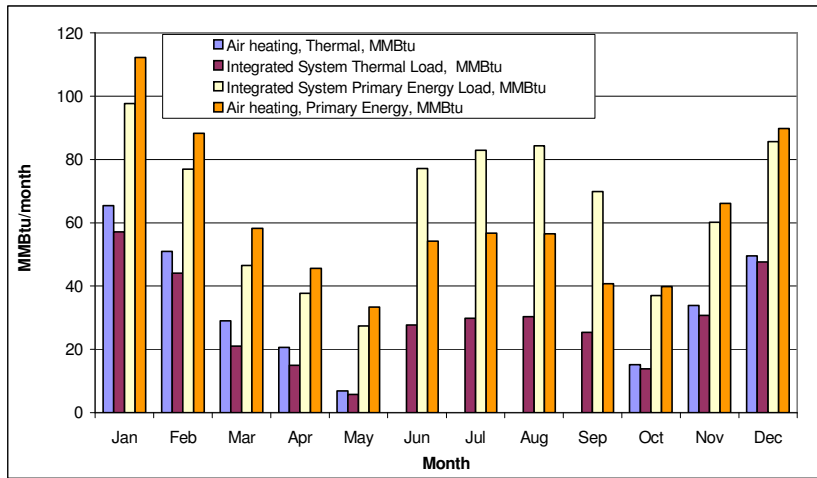
Figure 7.17 Comparisons of Thermal Loads and Primary Energy Consumption of a Single Duct VAV System and the Sensible Heating and Cooling with an Integrated Active Ventilation Unit
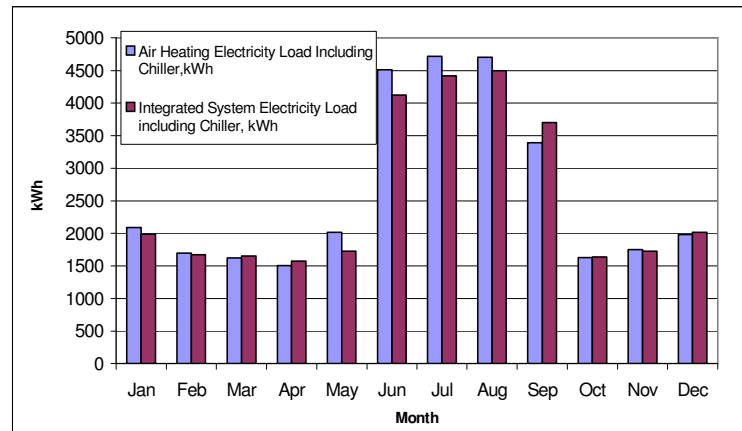
Figure 7.18 Comparison of Total Electricity Load of Single Duct VAV System and the Sensible Heating and Cooling System with an Integrated Active Ventilation Unit

Figures 7.17, 7.18, 7.19, 7.20 compare the total thermal load, total electricity load and primary energy consumption of these three systems. From these figures, the monthly electricity loads of the three systems are close; the annual electricity loads are 31,617kWh, 30,717kWh and 29,525kWh, respectively, for the air heating and cooling system, the integrated system with an active desiccant unit and the integrated system with a passive desiccant unit. In the cooling season from June to September, the primary energy consumption of the integrated system with an active ventilation unit is much higher than the air system and the integrated system with a passive desiccant ventilation unit. The reason is that the active desiccant system uses natural gas to regenerate the desiccant wheel. The regeneration processes reheat the supply air from 54 ℉ after DX to 60°F, which reduces the cooling capacity of the cooling air. On the basis of energy consumption, the single duct VAV system is slightly better than the current active desiccant system during the summer. However, the integrated active desiccant system may provide more control measures on indoor thermal comfort. Please see the discussion in Section 7.5.4 for more information on this issue. The current system with an integrated active desiccant unit consumes about 28.5% more thermal energy, 2.8% less electricity and 5.7% more primary energy than a single duct VAV air heating and cooling system, on an annual basis. The current system with a presumed passive desiccant ventilation unit consumes about 21.0% less thermal energy, 2.3% less electricity and about 11.4% less primary energy than a single duct VAV system.
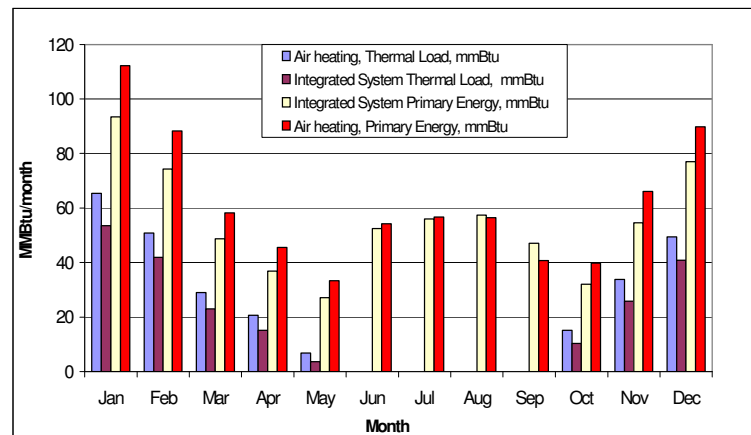
Figure 7.19 Comparisons of Thermal Loads and Primary Energy Consumption of a Single Duct VAV System and the Sensible Heating and Cooling System with an Integrated Passive Ventilation Unit
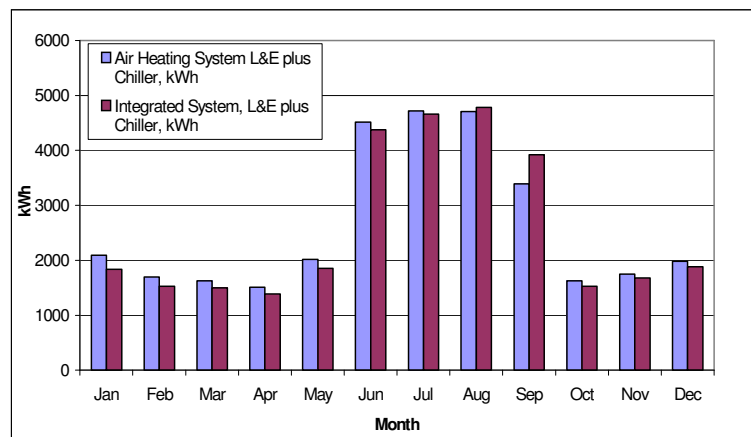
Figure 7.20 Comparisons of Electricity Loads of a Single Duct VAV System and the Sensible Heating and Cooling System with an Integrated Passive Ventilation Unit

The estimated chilled water, hot water and electricity prices are $13/MMBtu, $11.5/MMBtu and $0.09/kWh, respectively, based on current Texas A&M University physical plant data. The current natural gas price is around $10.5/MMBtu for commercial customers. Figure 7.21 indicates the energy cost for these three different systems. It can be seen that the cost of the passive desiccant system is lower than the air system and the active system, per month. The active system costs less than the single duct VAV air system in winter, but it costs more than the air system in summer. The annual cost of the passive system is 22.7% less than the single duct

VAV system, while the annual cost of the active system is 2.4% less than the single duct VAV air system.
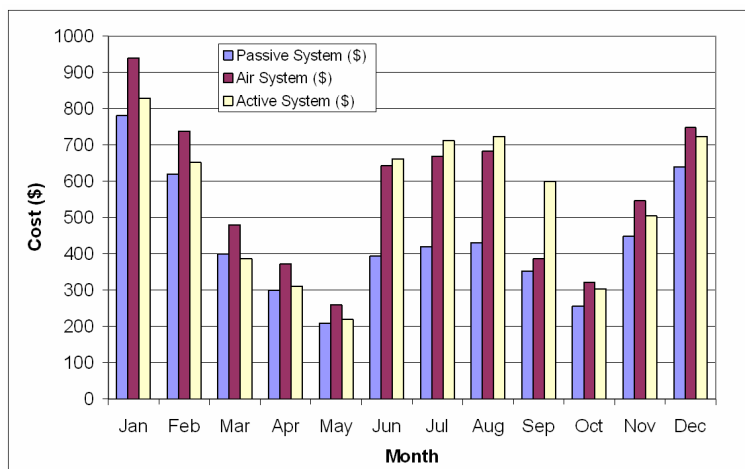
Figure 7.21 Energy Costs of the Three Different Systems

The above results are based on the simulation of the IW sensible heating and cooling system and the integrated ventilation unit. This system supplies a near constant 3000CFM of conditioned air to the IW during the summer in order to control indoor humidity to avoid moisture condensation on the radiant panels. The design flow of a single duct VAV system for the IW could be around 6000CFM. In the partial load condition of the summer, the integrated system does not have too many advantages over the air heating and cooling system.

7.5.3. Energy Consumption at Optimal Operation Conditions

The infiltration not only affects the indoor humidity of a radiantly cooled office in the summer, but also impacts the energy consumption. The comparison of primary energy consumption in the previous chapter is based on the estimated IW infiltration discussed in Chapter VI. If the sensible heating and cooling system ran in a very tight space, how would the system perform? First, when the space is very tight, the building heating and cooling loads will be smaller; second, the ventilation air flow rate can be largely reduced from 3000CFM to about 650CFM. The related fan power and energy used to condition the outside air can also be reduced. As discussed in Chapter V, 650CFM can satisfy the indoor humidity requirement when

infiltration is close to 0. Figure 7.22 compares the air heating and cooling system with two integrated solid desiccant units, respectively, at a zero infiltration condition. The following assumptions are used in the simulation process.

    A.   The ventilation rate is assumed to be 650CFM for these three different systems.

    B.   The exhaust air flow for both the active and passive ventilation units is 650CFM.

    C.   The supply air humidity ratio of the active desiccant unit is controlled by the regeneration temperature and can be calculated by Equation 7.1. The average DX coil COP is 3.1, based on the SEMCO REV 2250 measured data.

    D.   The supply air temperature after the DX is 54ºF, 0.009lb/lb.

    E.   There is no return air mixed with the supply air in both the active and passive systems.
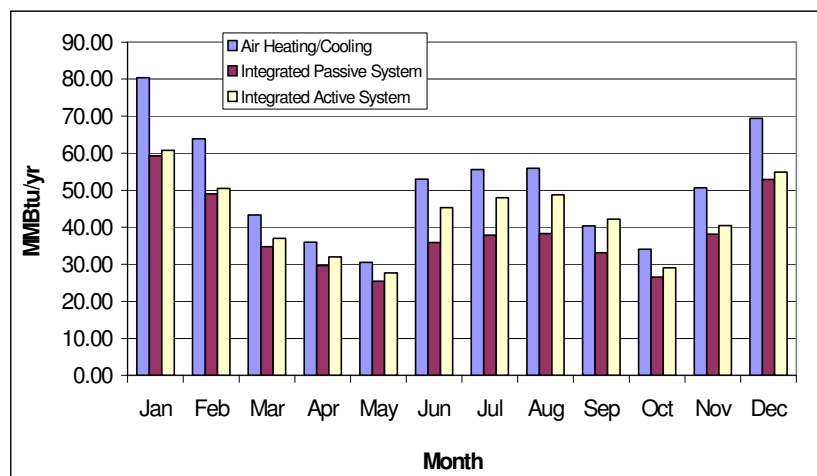
Figure 7.22 The Comparison of Primary Energy Consumption at a Zero Infiltration Condition

Figure 7.22 compares the primary energy consumption of three systems at optimal conditions, where infiltration is 0 and the ventilation flow rate is 650CFM. It can be seen that the primary energy consumption values of the two integrated desiccant systems are lower than that of the single duct VAV air conditioning system every month. The integrated active desiccant system uses more primary energy than the integrated passive desiccant system. As compared

with the air system, the integrated passive and active desiccant systems use 24.8% and 15.7% less primary energy, respectively, at optimal conditions.

By comparing Figure 7.22 with Figure 7.17, it can be found that the primary energy consumption of all three systems is reduced when the infiltration is zero and the ventilation rate is reduced to 650CFM. The primary energy consumption of a single duct VAV system would be reduced 17.3% if the building was very tight. The integrated active system consumes 34.0% less primary energy and the integrated passive system consumes 29.8% less primary energy than their consumption at current infiltration conditions. The energy consumption of the three systems is shown in the Appendix V.

Based on the energy prices listed in Section 7.5.3, the annual energy cost of the integrated active system is 26.7% less than the single duct VAV system and the annual energy cost of the integrated passive system is 35.6% less than the single duct VAV system.

7.5.4 The Integrated Active System Run as a VAV System

The current integrated active system supplies 3000 CFM in summer and 2000 CFM in winter. When outside air humidity is less than 0.008lb/lbda, the IW may not need the above amount of ventilation air for humidification, even in the high infiltration conditions. One strategy is to control the ventilation air flow based on the outdoor air humidity ratio, because the current supply air fan and return air fan are VFD controlled. When ventilation air flow rate is reduced, the fan power consumption and the energy to condition the outside air can be reduced. To ensure the operation of radiant panels without condensation, the indoor humidity ratio should be kept below 0.009 lb/lbda (dew point of 55°F) when the active system is running as a VAV system. Figures 7.23 and 7.24 compare the thermal energy consumption, primary energy consumption and electricity consumption of the IW when the active desiccant ventilation unit runs at constant volume (CV) and variable volume (VAV) conditions. The following control logic is used in the simulation process

A.   In heating conditions, when outdoor air humidity ratio (Woa) is less than 0.009lb/lb, OA flow (Voa) is set to 650 CFM, and return room air flow is set to zero. When Woa is between 0.009lb/lb and 0.011lb/lb, total supply flow is controlled by the following linear equation: $\dot{V}_{flow} = 650 + 1355\dfrac{0.011 - Woa}{0.002}$. When outdoor air humidity ratio is higher than 0.011lb/lb, the total supply air is 2000 CFM

($\dot{V}_{flow} = 2000CFM$). Voa is set to 650 cfm all the time and the return air is controlled to be $\dot{V}_{return} = 2000 - \dot{V}_{oa}$.

B.   In cooling conditions, when outdoor air humidity ratio (Woa) is less than 0.009lb/lb, OA CFM (Voa) is set to 650 CFM, and return room air CFM is set to zero. When Woa is between 0.009lb/lb and 0.011lb/lb, total supply flow is controlled by the following linear equation: $\dot{V}_{flow} = 650 + 2355\dfrac{0.011 - Woa}{0.002}$. When outdoor air humidity ratio is higher than 0.011lb/lb, the total supply air is 2000 CFM ($\dot{V}_{flow} = 2000CFM$). In summer, the supply air humidity ratio is controlled to be less than 0.008lb/lbda. The Voa is set to be 650 CFM all the time and the return air is controlled to be $\dot{V}_{return} = 2000 - \dot{V}_{oa}$
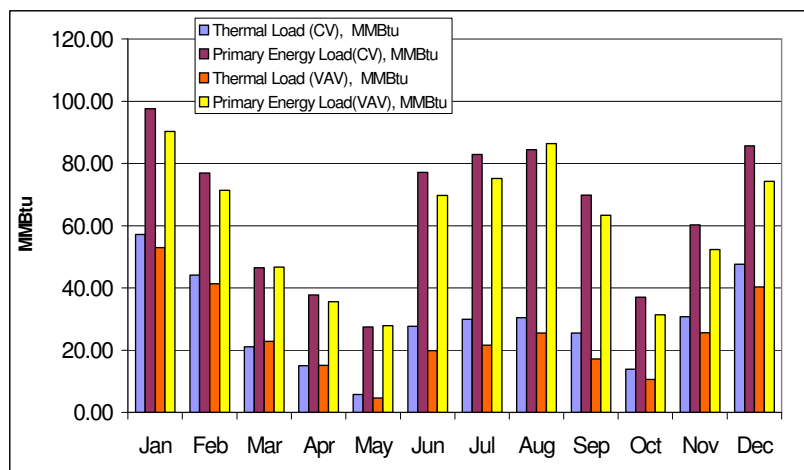
Figure 7.23 The Comparison of Thermal Load and Primary Energy Consumption of the Integrated Active System Running at Constant Volume and Variable Volume Conditions

Figure 7.23 indicates that when the active desiccant ventilation unit runs as a VAV unit (VAV model), it consumes less thermal energy than it does with CV operation, which supplies constant volume of air to the IW. The primary energy consumption of the VAV model is also less than that of the CV model in each month except August, when primary energy consumption

is almost equal. On an annual basis, the primary energy consumption of the VAV model is 2.3% less than a single duct VAV system, while the primary energy consumption of the CV model is 5.6% more than the single duct VAV system. The thermal energy and primary energy consumption of the VAV model are 14.8% and 7.6% less than those of the CV model.
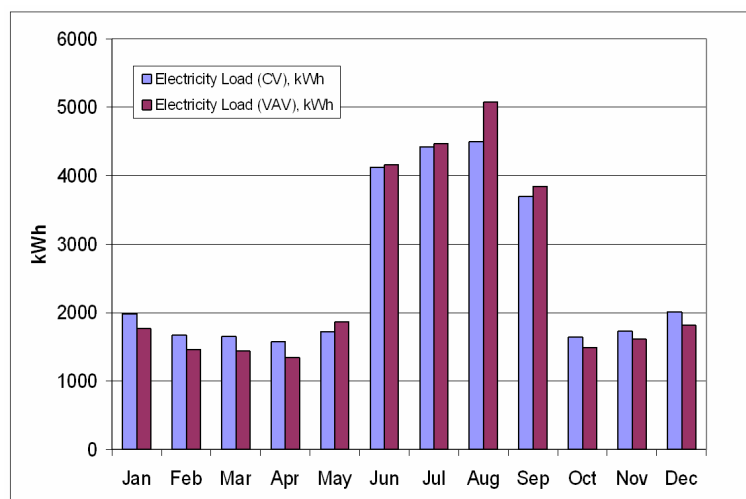
Figure 7.24 The Comparison of Electricity Load of the Integrated Active System Running at Constant Volume and Variable Volume Conditions

Figure 7.24 shows that electricity loads of the VAV model are lower than those of the CV model in winter months, but they are higher in summer months. The reason is that when the VAV model reduces the conditioned air to the space in summer, the sensible cooling system (radiant panels and fan coils etc) meet more of the sensible cooling load. The electricity consumption of the fan coil motors and pump motors increases. On an annual basis, the total electricity consumption of the VAV model is 1.2% less than that of the CV model. The simulated energy consumption of the two systems is shown in the Appendix VI.

The hourly simulation shows the indoor dew point temperature would not be above the surface temperature of the radiant panels in the summer. There will only be 6 hours in a year when the space dew point will be above the chilled water supply temperature of the radiant panels. In general, there will not be condensation problems even at current infiltration levels.

7.5.5 Humidity and Thermal Comfort

The active desiccant ventilation unit decoupled the sensible and latent loads of the IW. The humidity level of the IW can be controlled independent of the IW's sensible load. This system ensures that both the radiant cooling and sensible cooling can run safely. Also, the indoor air conditions are always within the ASHRAE comfort zone. The integrated system with a passive desiccant unit can control the space humidity ratio by adjusting the ventilation air temperature and flow rate. The radiant and sensible cooling devices in this system can operate safely during most summertime hours. However, the indoor humidity control capability of the passive desiccant system is limited to the cooling capability of the DX coil. The air temperature after the DX coil in this unit normally cannot be lower than 50ºF. This system does not work very well in a leaky space.

The sensible and latent loads are coupled together in the air heating and cooling system. The humidity control capability of the air heating and cooling system is much less than the two types of integrated systems discussed above. The capability of removing the latent load in all air system depends on the magnitude of the sensible load. The relative indoor humidity varies between 45% and 70% (0.0012lb/lb, 73°F) in the summer when using either air cooling or sensible cooling with a passive desiccant ventilation unit. The integrated system with an active ventilation unit has a superb ability to control the indoor air comfort level.

7.6 Summary

This chapter presents the sensible heating and cooling system of mullions, radiant panels, cool waves and fan coils in the IW with an integrated active desiccant ventilation unit and a passive desiccant ventilation unit, respectively. Based on the same input conditions, this chapter compared the daily and monthly thermal, electricity and primary energy consumption of the IW sensible heating and cooling system with a single duct VAV air heating and cooling system. The results show that the current system with an integrated active desiccant ventilation unit consumes about 28.5% more thermal energy, 2.8% less electricity and 5.6% more primary energy than a single duct VAV air heating and cooling system. The current system with a presumed integrated passive desiccant ventilation unit consumes 21.0% less thermal energy, 2.3% less electricity and about 11.4% less primary energy than a single duct VAV system. On the basis of thermal comfort, the current integrated active desiccant ventilation system can easily control the relative indoor humidity ratio below 50% (0.009lb/lb, 73°F) in the summertime, while the passive

desiccant ventilation system or the air heating and cooling system cannot control the indoor humidity ratio very well. The relative indoor humidity ratio varies between 45% and 70% (0.0012lb/lb, 73°F) in summer when using these two types of systems.

By assuming that the infiltration is close to zero and the ventilation is 650CFM for the three systems, it is found that the primary energy consumption of all three systems could be greatly reduced: 17.3%, 34.0%, and 29.8% for air, integrated active and passive systems, respectively. The primary energy consumption of an integrated passive desiccant system is 24.8% less than a single duct VAV air system. The primary energy consumption of the active integrated desiccant system is 15.7% less than a single duct VAV air system, and it provides much better indoor humidity control. The energy consumption comparison of the three systems studied in this chapter is show in Table 7.5.

Table 7.5 Primary Energy Consumption Comparison of Three Systems

	Integrated Active Desiccant System			Integrated Passive Desiccant System		Single Duct VAV Air System	
	Current Leakage Condition, CV	No leakage Condition, 650 CFM	Current Leakage Condition, VAV	Current Leakage Condition, CV	No leakage Condition, 650 CFM	Current Leakage Condition	No leakage Condition
Thermal Load, MMBtu	348.46	143.48	296.92	214.37	123.08	271.19	183.19
Electricity Load, kWh	30717	28133	30340	30904	24716	31617	30705
Primary Energy Consumption, MMBtu	783.30	516.83	724.16	657.11	461.05	741.44	613.14
*Primary Energy Consumption Compared with SDVAV	5.6%	-15.7%	-2.3%	-11.4%	-24.8%	0.0%	-17.3%

* Primary energy consumption of desiccant systems at no leakage condition is compared with SDVAV at no leakage condition and vice versa.

The current sensible heating and cooling systems with an integrated active desiccant ventilation unit are not very efficient for the following reasons. A high leakage rate into the space admits a significant amount of moisture during the summer. In order to reduce the space humidity and make the radiant cooling system run without condensation, the ventilation system is set to supply 3000CFM of conditioned air with regeneration reheat. The supply air flow rate is

nearly half the design flow of an air heating and cooling system. Under partial load conditions during the summer, this system works similarly to a constant volume air system with reheat, and has little advantage over a single duct VAV air heating and cooling system with regards to energy consumption. At the current infiltration condition, if the active desiccant system runs as a VAV model using VFD drive fans, the thermal energy load, electricity load and primary energy consumption could be reduced by 14.8%, 1.2% and 7.6% respectively compared with the constant volume model. The integrated active desiccant system decouples the sensible and latent loads of the space. The indoor humidity level can be controlled independently, which is helpful for improving the indoor comfort level.

CHAPTER VIII

CONCLUSIONS AND RECOMMENDATIONS

8.1 Conclusions

This research investigates a low energy consumption building which uses radiant heating, cooling and a desiccant ventilation unit. The following aspects have been studied in detail: the heat transfer process of radiant mullions and overhead radiant panels, the impact of the radiator position on heating load and thermal comfort, the influence of infiltration on indoor humidity in a radiantly cooled office with a solid desiccant ventilation unit, and an energy consumption comparison of the sensible heating and cooling systems with a single duct VAV system. The conclusions and observations are summarized as follows.

8.1.1 The Simulation and Verification Study of the Radiant Mullions

The IW radiant mullion system is one type of façade heating and cooling system. No detailed study has been found in the available literature. This dissertation studies the heat transfer process of window mullion radiators and proposes one group of models to simulate the performance of radiant mullions. The simulation results have been compared with ten days of measured data. The comparison shows that the heat transfer models predict the measured temperatures with root mean square errors (RMSE) of the hot water return temperature, mullion surface temperature, and window surface temperature of 0.90°F, 0.98°F and 1.15°F, respectively:

The performance study of radiant mullions has shown that hot water and chilled water supply temperatures are the primary factors affecting the heating or cooling capacity of radiant mullions and the mullion surface temperature. The window surface temperature distribution is affected by the mullion surface temperature and the inside and outside air temperatures. The temperature gradient on the glazing surface within one foot from the mullions is much higher than in the central part of the window. The temperatures in the central 2 feet of a 4-foot window show almost no influence from the mullion surface temperature.

The conductive thermal resistance of the mullion double tubes and gap filling plays a decisive role in controlling the mullion and window frame temperatures. The increased mullion tube conductive resistance results in a lower surface temperature for heating and a higher surface temperature for cooling. The higher surface temperature for cooling may be intended to lower the risk of moisture condensation on the surface of the mullion in the cooling condition.

However, the enhanced thermal resistance decreases the heating and cooling capacity of the mullion. If the mullions are only used for heating, a single tube structure is recommended.

From the design perspective, the window width or spacing between the mullions has little impact on the heating capacity or mullion surface temperature. However, the space between the mullions will somewhat affect the window inner surface temperature distribution and average window temperature.

8.1.2 The Simulation Study of the Overhead Panels

The heat transfer principles of the overhead radiant panels are studied and a heat transfer model has been set up, which can be solved for the supply water outlet temperature, average panel surface temperature and overall panel surface heat transfer coefficient. The study has found that the heating and cooling capacity of the overhead panel without top insulation is a semi-linear function of the supply water temperature when the flow rate is fixed.

The cooling capacity of the overhead radiant panel is around 44.63Btu/(hr-°F) at the chilled water supply temperature of 55ºF; it is greatly affected by the room air temperature and slightly affected by the water flow rate. The heating capacity of the overhead radiant panel is around 144.12 Btu/(hr-°F) at the hot water supply temperature of 120°F. Room air temperature and supply water flow rate affect the heating input of the overhead radiant panels. The heating capacity increases about 8.5% when the room air temperature drops from 72ºF to 68ºF, and it decreases about 14.2% if the hot water flow rate is reduced to half of the design flow rate.

The thermal contact resistance between the water tubes and the aluminum radiant panels has a significant impact on the thermal performance of the overhead radiant panels. When the thermal contact resistance increases to 0.2 Btu/(hr-°F), the cooling capacity drops about 18.6% and the heating capacity drops about 20.6%. The thermal contact resistance should be reduced to be as small as possible in the design processes.

8.1.3 The Impact of the Radiator Position on Heating Load and Thermal Comfort

The position of the radiators in a radiantly heated office has been shown to impact the heating load and the thermal comfort distribution inside the room. When radiators are close to the window, the increase of window surface temperature is higher than when the radiator is located in the center of the ceiling. The energy savings relative to the convective air system

depend on the outside air supply rate. When the outside air supply rate and the rate of infiltration increase, the energy savings of the radiant system also increase.

The control device used also affects the energy consumption of a radiant heating system. If the dry bulb temperature thermostat is used instead of an operative temperature thermostat in a radiantly heated space and the air temperature is set at the same point as that which is used for air heating, radiant heating will increase the heating load as much as 11.5% higher compared to the air heating for the cases studied.

On the basis of thermal comfort, radiators located close to the window can reduce down draft, prevent cold penetration inside a room and make the operative temperature distribution much more uniform than when the radiator is located in the center of the ceiling.

8.1.4 Indoor Humidity Analysis and the Desiccant Ventilation Units

The indoor humidity study has found that the active desiccant ventilation system dries a space deeply and continuously, while a passive desiccant ventilation system dries a space more energy efficiently. The moisture removal capacity of a passive desiccant system depends upon the dryness of the exhaust air. When a passive ventilation system is the only source of dehumidification, the system cannot remove moisture without post-desiccant cooling.

High infiltration is one of the main causes of condensation in a radiantly cooled space during the summer. Radiant panels cannot work without condensation in a leaky space, even if the supply air is conditioned to $52^{o}F$, 0.008lb/lb. Pressurizing the space with ventilation air is one of the possible solutions available for avoiding water condensation on the surface of radiant cooling panels in a leaky building. The infiltration and ventilation rate has a significant impact on energy consumption in an oversized ventilation system. The primary energy consumption can increase by 35.7% when the infiltration rate increases from 0.0 to 0.45; and at the same infiltration condition of 0.45 ACH, the primary energy consumption would increase about 42.4% when the ventilation rate increases from 650 CFM to 1600 CFM.

8.1.5. The Infiltration Study of the IW

The indoor humidity study has identified infiltration as a major factor that affects energy consumption and the safe operation of the radiant cooling system. This dissertation reviews the previous infiltration study of the IW that used the tracer gas method, reanalyzes the CO_2 concentration data, and evaluates the infiltration by using logged humidity data. The results for

the IW's infiltration range from 0.78-1.31ACH by the tracer gas method, 0-1.2 ACH by the CO_2 concentration method, 0.5-2.0 ACH from the logged humidity data.

A significant portion of the leaking air has been found to come from the plenum and the third floor. A simulation study of the IW using DOE2.1 identified an estimated rate of outside air leakage, based on the calibration of the simulation to the measured heating consumption data. Combining the results of the calibrated DOE2 simulation and the blower door measurement, third floor air leakage into the IW can be estimated. This process gives outside air leakage ranging from 0.1-0.5 ACH, while the third floor air leaking into the IW may range from 0.46-1.03 ACH .

8.1.6 The Comparison of a Sensible Heating and Cooling System with a Single Duct VAV System

The IW used radiant heating and cooling with a passive desiccant ventilation unit before the winter of 2005. The passive desiccant ventilation system was replaced by an active desiccant ventilation system for testing purposes during the winter of 2005. A group of fan coil units are planned for installation in the southern zone to offer additional cooling in the near future. The sensible heating and cooling system of mullions, radiant panels, cool waves and fan coils in the IW has been simulated. Based on the same input conditions, this dissertation compared the daily and monthly thermal, electricity and primary energy consumption of the IW sensible heating and cooling system with a single duct VAV air heating and cooling system. The results have shown that the current system with an integrated active desiccant ventilation unit consumes about 28.5% more thermal energy, 2.8% less electricity and 5.6% more primary energy than a single duct VAV air heating and cooling system. The current system with a presumed integrated passive desiccant ventilation unit consumes 21.0% less thermal energy, 2.3% less electricity and about 11.4% less primary energy than a single duct VAV system. On the basis of thermal comfort, the current integrated active desiccant ventilation system can easily control the relative indoor humidity ratio below 50% (0.009lb/lb, 73°F) in the summer, while the integrated passive desiccant system and the air heating and cooling system cannot control the indoor humidity ratio very well. The relative indoor humidity ratio varies between 45% and 70% (0.0012lb/lb, 73°F) in the summer by using these two types of systems.

By assuming that the infiltration is close to zero and the ventilation is 650CFM for the three systems, it is found that the primary energy consumption of all three systems could be greatly

reduced: 17.3%, 34.0%, and 29.8% for air, integrated active and passive systems, respectively. The primary energy consumption of an integrated passive desiccant system is 24.8% less than a single duct VAV air system. The primary energy consumption of the active integrated desiccant system is 15.7% less than a single duct VAV air system, and it is much better with regards to indoor humidity control.

8.2 Recommendations for Future Work

This dissertation has done a comprehensive investigation of the technical issues relative to radiant heating and cooling systems. The study has covered radiant component modeling, indoor humidity analysis, system operation strategies, an infiltration investigation, and integrated system simulations and comparisons. In order to make this research more valuable, some future work is recommended, as follows.

The overhead radiant panels are currently only used for cooling. There is no measured data available. Although the overhead panel simulation model in Chapter III produced reasonable results, the model would work better if it can be verified by measured data in the future. The following data need to be collected in order to verify the performance of the radiant panels: water flow rate, panel inlet water temperature, panel outlet water temperature, room air temperature, and panel surface temperature.

The active desiccant ventilation unit is currently the largest energy consumption unit in the Intelligent Workplace. It has been in operation for only one year. This device is tested and commissioned now. The yearly detailed operation data is not yet available. The integrated system simulation should be compared with the yearly measured data to yield more credible results.

The ultimate goal of this research project is to build a micro-cogeneration system powered by a fuel cell or diesel engine and connect this cogeneration system with the sensible heating and cooling system in the IW. When the cogeneration unit is installed, the exhaust heat from the engine or fuel cell could be used as the heat source for active desiccant wheel regeneration. If the waste heat from the prime mover is used for regeneration, the efficiency of the integrated sensible heating and cooling with an active desiccant ventilation unit would be greatly improved. The simulation of the sensible heating and cooling system needs to be integrated with the

simulation of the micro cogeneration system in order to evaluate the overall system efficiency. This work needs to be carried out in the future as the project progresses.

NOMENCLATURE

Chapter II

D_1	room air correction factor
D_2	flow rate correction factor
f_{IA}	inside air temperature weighting factor
f_{OA}	outside air temperature weighting factor
F_{win-i}	view factor between window and surface i
F_{1-i}	view factor between mullion tube and surface i
k	thermal conductivity, Btu/(hr-ft-°F)
h_c	convective heat transfer coefficient, Btu/(hr-ft^2-°F)
h_{c-win}	convective heat transfer coefficient at window indoor surface, Btu/(hr-ft^2-°F)
h_{c-m}	convective heat transfer coefficient at mullion tube, Btu/(hr-ft^2-°F)
h_{in}	convective heat transfer coefficient between water and mullion tube inside surface, Btu/(hr-ft^2-°F)
h_{ri}	radiation heat transfer coefficient between surface I and surface s, Btu/(hr-ft^2-°F)
L_1	fin length, ft
L_2	half of window frame width, ft
$\dot{m}$	hot or chilled water mass flow rate passing through single mullion, gpm
$\dot{m}_{total}$	hot or chilled water mass flow rate passing through mullion system, gpm
NU	Nusselt number
Pr	Prandtl number

$\dot{q}_s''$ heat transfer loss from mullion tube surface, Btu/(hr-ft^2)

$\dot{q}_{fin}$ conduction heat transfer rate at fin root, Btu/(hr-ft^2)

$\dot{Q}_{total}$ mullion system heating or cooling capacity, Btu/hr

R_{win} window conductive resistance, (hr-ft2-°F)/Btu

R_t conductive thermal resistance of mullion double tubes, (hr-ft2-°F)/Btu

T_{south} south zone temperature, °F

T_{north} north zone temperature, °F

T_{HW_S} hot water temperature set point, °F

T_{hw} hot water temperature, °F

T_o outside air temperature, °F

T_a room air temperature, °F

T_{a1} equivalent air temperature, °F

$T_{mullion-s}$ mullion surface setting temperature, °F

T_{ins} mullion tube inside surface temperature, °F

T_b hot water bulk temperature, °F

T_{ret} hot or chilled water return temperature, °F

T_{mu} mullion surface temperature, °F

T_{fr} window frame surface temperature, °F

T_{tube} mullion tube surface temperature, °F

T_{hws} hot water supply temperature, °F

T_{cws} chilled water supply temperature, °F

T_1 mullion tube surface temperature, °F

T_2 window glass inside surface temperature, °F

T_3 mean radiant temperature of indoor space , °F

T_4 window frame temperature, °F

T_5 window fin surface temperature, °F

thk   thickness of mullion fin, ft

U_{in1} overall heat transfer coefficient at mullion fin surface, Btu/(hr-ft^2-°F)

U_{in2} overall heat transfer coefficient at window frame surface, Btu/(hr-ft^2-°F)

U_{out} overall heat transfer coefficient of window frame, Btu/(hr-ft^2-°F)

Chapter III

A_p,   panel surface area, ft^2

C_P specific heat, Btu/(lb-°F)

D   outside diameter of the water tube, ft

D_1 room air correction factor,

D_2 flow rate correction factor

F_1 panel heat transfer efficient factor

F_f fin heat transfer coefficient

F_R panel heat recovery factor

h_{in},   water side convective heat transfer coefficient, Btu/hr-ft^2-°F

h   convective heat transfer coefficient, Btu/hr-ft^2-°F

K   thermal conductivity, Btu/hr-ft-°F

L   root length of the connection part between panel and tube, ft

M   constant used in fin heat transfer calculation

P   equivalent heat transfer area, ft^2

$\dot{q}_1$ heat transfer rate of the fin, Btu/(hr-ft^2)

$\dot{q}_2$ heat transfer rate of the base, Btu/(hr-ft^2)

$\dot{q}_p$ total heat transfer rate through the pane, Btu/(hr-ft^2)

$\dot{q}_s$ heat transfer rate through root surface, Btu/(hr-ft^2)

$\dot{q}_o$ overall heat input from one panel module, Btu/(hr-ft^2)

$\dot{Q}_{C0}^{"}$ cooling capacity per unit area, Btu/(hr-ft^2)

$\dot{Q}_{h0}^{"}$ heating capacity per unit area, Btu/(hr-ft^2)

$\dot{Q}_C$ total cooling capacity, Btu/hr

$\dot{Q}_H$ total heating capacity, Btu/hr

R_s contact thermal resistance, Btu/(hr-ft^2-°F)

R   radius of water tube, ft

T_a,   room air temperature, °F

T_b fin base temperature, °F

T_f water temperature, °F

T_{fi} water inlet temperature, °F

T_{fo} water outlet temperature, °F

T_{pm} mean panel surface temperature, °F

U_o overall heat transfer coefficient by assuming panel surface temperature is fluid inlet

     temperature, Btu/(hr-ft^2-°F)

U_P actual average panel surface heat transfer coefficient, Btu/(hr-ft^2-°F)

W   panel width, ft

ε emissivity

σ Stefan-Boltzmann constant, 0.1714x10-8, Btu/(h-ft^2-°R)

Subscripts

c,b panel bottom side convective heat transfer

r,b panel bottom side radiation heat transfer

c,t panel top side convection heat transfer

r,t panel top side radiation heat transfer

Chapter IV

C_p specific heat of air, Btu/(Lb-°F)

F_{p-i} view factor between occupant and room surfaces

F_{s-i} view factor from surface s to surface i

F_{wj-i} view factor from wall j to surface i

H   coefficient of convective heat transfer, Btu/(h-ft^2-°F)

h_c convective heat transfer coefficient of ceiling, Btu/(h-ft^2-°F)

h_{c-p} convective heat transfer coefficient of radiator surface(s) , Btu/(h-ft^2-°F)

h_{c-win} convective heat transfer coefficient of window pane inside surface, Btu/(h-ft^2-°F)

h_{c-wj} convective heat transfer coefficient of wall inside surface, Btu/(h-ft^2-°F)

h_{ri} radiant heat transfer coefficient between two surfaces, Btu/(h-ft^2-°F)

h_{rp} radiant heat transfer coefficient between surface i and radiation panels, Btu/(h-ft^2-°F)

h_{rwin} radiant heat transfer coefficient between surface i and window, Btu/(h-ft^2-°F)

h_{rwj} radiant heat transfer coefficient between surface i and wall surface, Btu/(h-ft^2-°F)

K	coefficient of thermal conductivity, Btu/(hr-ft-°F)
$\dot{m}_{fa}$	infiltration mass flow rate, Lb/hr
$\dot{m}_{vent}$	ventilation mass flow rate, Lb/hr
R_s	thermal resistance of surfaces, (hr-ft^2-°F)/Btu
R_{win}	thermal resistance of window, (hr-ft^2-°F)/Btu
$\dot{q}$	heat generation per unit area per unit time, Btu/(hr-ft^2)
$\dot{q}_{air}$	net heat input by air heating, Btu/hr
$\dot{q}_{gain}$	internal heat gain, Btu/hr
$\dot{q}_r$	net radiant heat transfer per unit area per unit time, Btu/(hr-ft^2)
$\dot{q}_{radiator}$	net heat input by radiator, Btu/hr
T_a	room air temperature, °F
T_i, T_s	surface temperature, °F
T_{mi}	average temperature of two surfaces, °F
T_o	outside air temperature, °F
T_{op}	operative temperature, °F
T_p	radiator surface temperature, °F
T_r	mean radiant temperature, °F
T_{win}	inside surface temperature of window pane, °F
T_{wj}	surface temperature of wall j, °F
T_{vent}	ventilation air temperature, °F
ε	emissivity
σ	Stefan-Boltzmann constant

Chapter V

ach_i	hourly air exchange ratio
F1	ideal isopotential line of enthalpy
F2	ideal isopotential line of relative humidity
C_p	specific heat capacity, (Btu/lb*F)
$\dot{m}$	mass flow rate, lb/hr
$\dot{m}_{gen}$	moisture generation, lb/hr
T	temperature, ^{o}F or K
V_r	space volume, ft^3
$\dot{V}_s$	supplied outside air flow volume rate, ft^3/hr
ρ	air density, lb/ft^3
W	absolute humidity ratio, lb/lb
ε_l	moisture transfer effectiveness
ε_s	sensible heat transfer effectiveness
ε_{F1}	effectiveness of total energy transfer at optimum rotary speed
ε_s	effectiveness of moisture transfer at optimum rotary speed

Subscripts

S	supply air
o	outside air
r	room air
o1	inlet of supply air at passive or active wheel
o2	outlet of supply air at passive or active wheel

e1   inlet of exhaust air at passive desiccant wheel

e2   outlet of exhaust air at passive desiccant wheel

r,1   inlet of regeneration air at active desiccant wheel

r,2   outlet of regeneration air at active desiccant wheel

min   minimum

Chapter VI

$\dot{m}_{in}$ CO_2 flow into the space, lb/hr

$\dot{m}_{out}$ CO_2 flow out of the space, lb/hr

$\dot{m}_{gen}$ CO_2 generation in the space lb/hr

V_r IW volume, ft^3

α air change rate per hour

ρ density of CO_2, kg/m^3

A_L equivalent or effective air leakage area, in^2

Q_r predicted or measured air flow rate at ΔP_r CFM

ρ air density, lb_m/ft^3

Δp_r reference pressure difference, inches. of water

C_D discharge coefficient, 0.65

C_5 unit conversion factor, 0.186

$\dot{W}_{in}$ moisture entering the space by infiltration and mechanical ventilation, Lb/hr

$\dot{W}_{out}$ moisture leaving the space by exhaust air and exfiltration, Lb/hr

$\dot{W}_{gen}$ moisture generated by the occupants, Lb/hr

$\dot{W}_{storage}$ moisture storage in the space, assumed to be 0 in this analysis, lb/hr

w_s mechanical ventilation air humidity ratio, lb/lbda

w_o outside air humidity ratio, lb/lbda

w_r indoor humidity ratio, lb/lbda

$\dot{V}_s$ supply air flow rate, CFM

V_r IW space volume, 86000 ft^3

$\dot{V}_L$ exhaust air and return air flow rate, CFM

α infiltration rate

ρ air density lb/ft^3

REFERENCES

ASHRAE. 2005. *ASHRAE Handbook-Fundamentals*. Atlanta: American Society of Heating, Refrigeration and Air-Conditioning Engineers, Inc.

ASHRAE. 2004. *ASHRAE Handbook-HVAC Systems and Equipment*. Atlanta: American Society of Heating, Refrigeration and Air-Conditioning Engineers, Inc.

ASHRAE. 2004. *ANSI/ASHRAE Standard 55-2004, Thermal Environment Conditions for Human Occupancy*. Atlanta: American Society of Heating, Refrigeration and Air-Conditioning Engineers, inc.

ASHRAE. 2001. *ANSI/ASHRAE Standard 62-2001, Ventilation for Acceptable Indoor Air Quality*. Atlanta: American Society of Heating, Refrigeration and Air-Conditioning Engineers, Inc.

Awbi, H.B., and A. Hatton. 2000. Mixed convection from heated room surfaces. *Energy and Buildings* 32: 233-244.

Babus'Haq, R.F., H. Olsen, S.D. Probert. 1996. Feasibility of using an integrated small scale CHP unit plus desiccant wheel in a leisure complex. *Applied Energy* 53: 179-192.

Behne, M. 1995. Is there a risk of draft in rooms with cooled ceilings? Measurement of air velocities and turbulences. *ASHRAE Transactions* 101(2): 744-752.

Betz, F., Z. Bornik, B. Dong, P. Kwok. 2006. CO_2, Occupancy, and ventilation in an open-plan environment, Project Report, Department of Architecture, Carnegie Mellon University.

Boonyakiat, J. 2003. A model-based approach to ventilation control in buildings, PhD dissertation, Department of Architecture, Carnegie Mellon University.

Brunk, M.F. 1993. Cooling ceilings – an opportunity to reduce energy cost by way of radiant cooling. *ASHRAE Transactions* 99(2): 479-487.

Bulk, E. V., J.W. Mitchell, S.A. Klein, 1985, Design theory for rotary heat and mass exchangers-II. Effective-number of transfer units method for rotary heat and mass exchangers, *International Journal of Heat and Mass Transfer* 28: 1587-1595.

Busweiler, U. 1993. Air conditioning with a combination of radiant cooling, displacement ventilation, and desiccant cooling. *ASHRAE Transaction* 99(2): 503-510.

Chapman, K.S., J. Rutler, R. Watson. 2000. Impact of heating system and wall surface temperatures on room operative temperature fields, *ASHRAE Transactions* 106(1): 506-514.

Chapman, K.S., J. DeGreef, and R. Watson. 1997. Thermal comfort analysis using BCAP for retrofitting a radiantly heated residence, *ASHRAE Transactions* 103(1): 959-965.

Chapman, K.S., P. Zhang. 1995. Radiant heat exchange calculations in radiantly heated and cooled enclosures, *ASHRAE Transactions* 101(2): 1236-1247.

Chen, Q. and J.V.D.R. Kooi. 1988. Accuracy: a computer program for combined problems of energy analysis, indoor air flow and air quality. *ASHRAE Transactions* 94(2): 196-214.

Claridge, D. E., N. Bensouda, S.U. Lee, G. Wei, K. Heinemeier, M. Liu. 2003. *Manual of Procedures for Calibrating Simulations of Building Systems*, Lawrence Berkeley National Laboratory, October, 2003.

Coad, W.J. 1999. Conditioning ventilation air for improved performance and air quality, *Heating/Piping/Air-conditioning*, Sept. 1998:49-56.

Collins, M. 2004. Convective heat transfer coefficients from internal window surface and adjacent sunlit venetian blind, *Energy and Buildings*, 36(3): 309-18.

Collins, M.; P.H. Oosthuizen, S.J. Harrison, D. Naylor. 2000. Numerical modeling of radiative and conductive heat transfer from an irradiated complex window assembly, *American Society of Mechanical Engineers, Heat Transfer Division, (Publication) HTD* 366: 95-106.

Conroy, C.L. and S.A. Mumma. 2001. Ceiling radiant cooling panels as a viable distributed parallel sensible cooling technilogy integrated with dedicated outdoor air systems. *ASHRAE Transaction* 107(1): 578-585.

Dale, J.D., Ackerman, M.Y. 1993. Thermal performance of a radiant panel floor-heating system, *ASHRAE Transactions* 99(1): 23-24.

DeGreef, J. and Chapman, K.S. 1998. Simplified thermal comfort evaluation of MRT gradients and power consumption predicted with the BCAP methodology. *ASHRAE Transactions* 104(2): 1090-1097.

Duffie, J.A., and W.A. Beckman. 1991. Solar Engineering of Thermal Processes, 2nd Edition, New York: Wiley Interscience.

Energy Information Adminstration. 2006. Annual energy outlook 2006, www.eia.doe.gov , accessed in December, 2006.

Environment Protection Agency. 2006. Atmosphere changes, accessed in December , 2006 http://www.epa.gov/climatechange/science/recentac.html.

Fanger, P. 1967. Calculation of thermal comfort: introduction of a basic comfort equation. *ASHRAE Transactions*. 73(2) 1-20.

Fluent Inc, 2005. *Fluent 6.2*, Comercial CFD software, Lebanon, NH.

Freund, S., S.A. Klein, D.T. Reindl. 2003. A semi-empirical method to estimated enthalpy exchanger performance and a comparison of alternative frost control strategies, *HVAC&R Research* 9(4): 493-508.

Gatley, Donald P. 2000. Dehumidification enhancements for 100 percent outside air AHUs, *Heating/Piping/Air Conditioning Engineering*, September 2000: 31-35.

Gibbs, D.R. 1994. Control of multizone hydronic radiant floor heating systems. *ASHRAE Transactions* 100(1): 1003-1010.

Gong, X. and D. E. Claridge. 2007. Impact of the position of the radiators on energy consumption and thermal comfort in a mixed radiant and convective heating system, *ASHRAE Transactions* 113(1): 494-503.

Hanibuchi, H. and S. Hokoi. 2000. Simplified method of estimating efficiency of radiant and convective heating systems. *ASHRAE Transactions* 106(1): 487-494.

Harriman, L. G. III, M. Czachorski, M.J. White, D.R. Kosar. 1999. Evaluating active desiccant systems for ventilation commercial buildings. *ASHRAE Journal* 41(10): 28-33.

Hodder, S.G., D.L. Loveday, K.C. Parsons, and A.H. Taki. 1998. Thermal comfort in chilled ceiling and displacement ventilation environments: vertical radiant temperature asymmetry effects. *Energy and Buildings* 27: 167-173.

Imanari, T., T. Omori, and K. Bogaki. 1999. Thermal comfort and energy consumption of the radiant panel system. Comparison with the conventional all-air system. *Energy and Buildings* 30:167-175.

Integrated Facades System Gartner. 1968. German Patent, Facade Manufacturer's website, http://www.josef-gartner.de/framesete.htm , Accessed in June, 2006.

Jeong, J.W., S. A. Mumma. 2005. Practical thermal performance correlations for molecular sieve and silica gel loaded enthalpy wheels, *Applied Thermal Engineering* 25: 719-740.

Jeong, J.W. and S.A., Mumma. 2003a. Energy conservation benefits of a dedicated outdoor air system with parallel sensible cooling by ceiling radiant panels. *ASHRAE Transactions* 109(2): 627-636.

Jeong, J.W. and S.A. Mumma. 2003b. Ceiling radiant cooling panel capacity enhanced by mixed convection in mechanically ventilated spaces. *Applied Thermal Engineering* 23: 2293-2306.

Jeong, J.W., S. A. Mumma, W. P. Bahnfleth. 2003. Energy conservation benefits of a dedicated outdoor air system with parallel sensible cooling by ceiling radiant panels. *ASHRAE Transactions* 109(2): 627-636.

Jurinak, J.J., J. W. Mitchell, J.W. Beckman. 1983. Open cycle desiccant air conditioning as an alternative to vapor compression cooling in residential applications. *Proceedings of the ASME Solar Energy Division Fifth Annual Conference*, Orlando, FL, USA, 374-381.

Khattar, M.K., and M.J. Brandemuehl. 2002. Separating the V in HVAC: a dual path approach. *ASHRAE Journal*, 44(5): 37-42.

Kilkis, B.I., S.S. Sager, and M. Uludag. 1994. A simplified model for radiant heating and cooling panels, *Simulation Practice and Theory* 2(2): 61-76.

Kilkis B. L. 1995. Coolp: A computer program for the design and analysis of ceiling cooling panels. *ASHRAE Transactions* 101(2): 703-710.

Kreider, J. F., P. S. Curtiss, A. Rabl. 2002. *Heating and Cooling of Buildings*, Boston, Massachusetts: McGraw Hill.

Kulpmann, R.W. 1993. Thermal comfort and air quality in rooms with cooled ceilings-results of scientific investigations. *ASHRAE Transactions* 99(2): 488-502.

Larsson, U.; B. Moshfegh, M. Sandberg. 1999. Thermal analysis of super insulated windows (numerical and experimental investigations), *Energy and Buildings* 29(2): 121-128.

Liu, M., D. E. Claridge, and W. D. Turner, 2002, *Continuous commissioning* ^{SM} *guidebook: maximizing building energy efficiency and comfort*, Federal Energy Management Program, U.S. Dept. of Energy, 2002.

Mahdavi, A., R. Ries, D. Cho. 2000. Infiltration, natural ventilation, and HVAC performance in the IW, *ASHRAE Transactions* 106(1): 728-36.

Mills, A. F. 1999. *Heat Transfer*, Upper Saddle River, New Jersey: Prentice Hall.

Min, T.C., L.F. Schutrum, G.V. Parmelee, and J.D. Vouris., 1956, Natural convection and radiation in a panel heated room, *ASHRAE Transactions* 62: 337-358.

Mumma, S.A., J. W. Jeong. 2005. Direct digital temperature, humidity, and condensate control for a dedicated outdoor air-ceiling radiant cooling panel system. *ASHRAE Transactions* 111(1): 547-558.

Mumma, S.A. 2003. Chilled ceiling condensation control, *ASHRAE IAQ Application* Fall 2003: 22-23.

Mumma, S.A., 2002. Chilled ceilings in parallel wth dedicated outdoor air systems: addressing the concerns of condensation, capacity, and cost. *ASHRAE Transactions* 108(2): 202-231.

Mumma, S.A. 2001a. Dedicated outdoor air in parallel with chilled ceiling systems. *Engineered Systems*. November 2001: 56-66.

Mumma, S.A. 2001b. Ceiling panel cooling system. *ASHRAE Journal*, 43(11): 28-32.

Mumma, S.A. 2001c, Condensation issues with radiant cooling panels. *ASHRAE IAQ Applications*, Fall 2001: 16-18.

Mumma, S.A. 2001d. Preconditioning dedicated OA for improved IAQ, Part 2. *ASHRAE IAQ Application*, Summer 2001: 21-23.

Mumma, S.A. and B.W. Lee. 1998. Extension of the multiple spaces concepts of ASHRAE Standard 62 to include infiltration, exhaust/exfiltration, interzonal transfer and additional short circuit paths. *ASHRAE Transactions* 104(2): 1232-1241.

Muneer, T.; N. Abodahab, A. Gilchrist. 1997. Combined conduction, convection, and radiation heat transfer model for double-glazed windows, *Building Service Engineering Research & Technology* 18(4): 183-191.

Niu, J.L., L.Z. Zhang, and H.G. Zuo. 2002. Energy savings potential of chilled-ceiling combined with desiccant cooling in hot and humid climates. *Energy and Buildings* 34: 487-495.

Niu, J.L., and J.V.D. Kooi. 1994. Thermal climate in rooms with cool ceiling systems. *Building and Environment* 29: 283-290

Niu, J.L., J.V.D. Kooi, and H.V.D. Ree. 1995. Energy saving possibilities with cooled ceiling systems. *Energy and Buildings* 23: 147-158.

Nielson, P. V. 1998. The selection of turbulence models for prediction of room airflow, *ASHRAE Transactions* 104(1): 1119-1127.

Olesen, B.W. 1994. Comparative experimental study of performance of radiant floor-heating systems and a wall panel heating system under dynamic conditions. *ASHRAE Transactions* 100(1): 1011-1023.

Omori, T.; S. Murakami, S. Kato. 1997. Numerical simulation of solar heat absorption within indoor space by means of composite grid method, *ASHRAE Transactions* 103(1): 164-171.

Palmer, J. and K.S. Chapman. 2000. Direct calculation of mean radiant temperature using radiant intensities. *ASHRAE Transactions* 106(1): 477-486.

Roth, K. W., D. Westphalen, J. Dieckmann, S. D. Hamilton, W. Goetzler. 2002. *Energy consumption characteristics of commercial building HVAC systems-Volume III: energy saving potential*. Final report to US Department of Energy, Office of Building Technology, www.doas.psu.edu/papers.html, Accessed in December 2006.

Shank, K.M., and S.A. Mumma. 2001. Selecting the supply air conditions for a dedicated outdoor air system working in parallel with distributed sensible cooling terminal equipment. *ASHRAE Transactions* 107(1): 562-571.

Sherman, M. H., and Dickerhoff, Darryl J. 1998. Airtightness of U.S. dwellings, *ASHRAE Transactions* 104(1): 1359-1367.

Simonson, C.J., W. Shang, R.W. Besant, 2000, Part-load performance of energy wheels: Part I-wheel speed control, *ASHRAE Transactions* 106(1): 286-300.

Simonson, C.J., R.W. Besant, 1999a, Energy wheel effectiveness. Part 1-development of dimensionless groups. *International Journal of Heat and Mass Transfer* 42(12): 2161-2170.

Simonson, C.J., R.W. Besant, 1999b, Energy wheel effectiveness. Part 2-correlations, *International Journal of Heat and Mass Transfer* 42(12), 2171-2185.

Simmonds, P., 1996, Practical applications of radiant heating and cooling to maintain comfort conditions. *ASHRAE Transactions* 102(1): 659-666.

Simmonds, P. 1994. Control strategies for combined heating and cooling radiant systems. *ASHRAE Transactions* 100(1): 1031-1039.

Sodec, F. 1999. Economic viability of cooling ceiling systems. *Energy and Buildings* 30: 195-201.

Steinman, M., L.N. Kalisperis, and L.H. Summers. 1989. The MRT-correction method – An improved method for radiant heat exchange. *ASHRAE Transactions* 95(1): 1015-1027.

Stetius, C. 1999, Energy and peak power savings potential of radiant cooling systems in US commercial buildings, *Energy and Buildings* 30: 127-138.

Stetius, C. and H.E. Feustel. 1995. *Development of a Model to Simulate the Performance of Hydronic/radiant Cooling Ceilings*. Lawrence Berkeley Laboratory (LBL) Report No. 36636, Berkeley, CA.

Tassou, S. A., W. Xiang, and M. Kolokotroni. 2000. Church heating: numerical modeling and comparison between radiant and forced convection systems, *ASHRAE Transactions* 106(1): 495-505.

Truelove, J.S. 1987. Discrete-ordinates solutions of the radiative transport equation. *Journal of Heat Transfer* 109: 1048-1051.

U.S. Department of Energy, *Radiant floor heating and cooling systems* http://www.eere.energy.gov/consumerinfo/ factsheets/bc2.html, Accessed in July 2005.

Xia, Y.; and S. A. Mumma. 2006. Ceiling radiant cooling panels employing heat-conducting rails: deriving the governing heat transfer equations, *ASHRAE Transactions* 112(1): 34-41.

Yin, H., 2006, An absorption chiller in a micro BCHP application: model based design and performance analysis, PhD dissertation, Department of Architecture, Carnegie Mellon University.

Zhang, L.Z, J.L Niu. 2003. Indoor humidity behaviors associated with decoupled cooling in hot and humid climates, *Building and Environment* 38: 99-107.

APPENDIX I

PERFORMANCE OF A SINGLE MULLION AT HEATING CONDITION

To ($^{\circ}$F)	T_{hws} ($^{\circ}$F)	T_{return} ($^{\circ}$F)	Flow (lb/s)	Q_{input} (Btu/hr)	T_{tube} ($^{\circ}$F)	T_{win} ($^{\circ}$F)	T_{wall} ($^{\circ}$F)	T_{frame} ($^{\circ}$F)	T_{fin} ($^{\circ}$F)	Rt (ft^2-hr-$^{\circ}$F))
38	75	74.2	0.232	94.5	73.6	61.4	72.5	72.5	72.8	0.041
38	77	76.0	0.232	120.3	75.2	61.4	72.5	73.9	74.3	0.041
38	79	77.7	0.232	147.3	76.8	61.4	72.5	75.3	75.7	0.041
38	81	79.5	0.232	175.3	78.3	61.5	72.5	76.6	77.2	0.041
38	83	81.2	0.232	204.0	79.9	61.5	72.5	78.0	78.6	0.041
38	85	83.0	0.232	233.3	81.5	61.6	72.5	79.3	80.0	0.041
38	87	84.7	0.232	263.1	83.0	61.6	72.5	80.6	81.4	0.041
38	89	86.5	0.232	293.4	84.5	61.6	72.5	82.0	82.7	0.041
38	91	88.2	0.232	324.2	86.1	61.7	72.5	83.3	84.1	0.041
38	93	89.9	0.232	355.4	87.6	61.7	72.5	84.5	85.5	0.041
38	95	91.7	0.232	387.0	89.1	61.8	72.5	85.8	86.8	0.041
38	97	93.4	0.232	418.9	90.7	61.8	72.5	87.1	88.2	0.041
38	99	95.1	0.232	451.2	92.2	61.9	72.5	88.4	89.5	0.041
38	101	96.8	0.232	483.8	93.7	61.9	72.5	89.6	90.8	0.041
38	103	98.5	0.232	516.7	95.2	61.9	72.5	90.9	92.2	0.041
38	105	100.3	0.232	549.9	96.7	62.0	72.5	92.2	93.5	0.041
38	107	102.0	0.232	583.5	98.2	62.0	72.5	93.4	94.8	0.041
38	109	103.7	0.232	617.2	99.7	62.1	72.5	94.6	96.1	0.041
38	111	105.4	0.232	651.3	101.2	62.1	72.5	95.9	97.4	0.041
38	113	107.1	0.232	685.6	102.6	62.2	72.5	97.1	98.7	0.041
38	115	108.8	0.232	720.2	104.1	62.2	72.5	98.3	100.0	0.041
38	117	110.5	0.232	755.0	105.6	62.3	72.5	99.5	101.3	0.041
38	119	112.2	0.232	790.1	107.1	62.3	72.5	100.8	102.6	0.041
38	121	113.9	0.232	825.4	108.5	62.3	72.5	102.0	103.9	0.041
38	123	115.6	0.232	860.9	110.0	62.4	72.5	103.2	105.2	0.041
38	125	117.3	0.232	896.7	111.5	62.4	72.5	104.4	106.4	0.041

APPENDIX II

PERFORMANCE OF A SINGLE MULLION AT COOLING CONDITION

T_o ($^\circ$F)	T_{hws} ($^\circ$F)	T_{return} ($^\circ$F)	Flow (lb/s)	Q_{input} (Btu/hr)	T_{tube} ($^\circ$F)	T_{win} ($^\circ$F)	T_{wall} ($^\circ$F)	T_{frame} ($^\circ$F)	T_{fin} ($^\circ$F)	Rt (ft^2-hr-$^\circ$F)
68.6	45.0	48.4	0.232	-399.4	51.0	72.5	74.0	54.1	53.2	0.041
68.6	47.0	50.2	0.232	-369.1	52.6	72.6	74.0	55.4	54.6	0.041
68.6	49.0	51.9	0.232	-339.1	54.1	72.6	74.0	56.7	56.0	0.041
68.6	51.0	53.7	0.232	-309.1	55.7	72.6	74.0	58.0	57.3	0.041
68.6	53.0	55.4	0.232	-279.4	57.2	72.7	74.0	59.3	58.7	0.041
68.6	55.0	57.2	0.232	-249.8	58.8	72.7	74.0	60.7	60.1	0.041
68.6	57.0	58.9	0.232	-220.4	60.3	72.8	74.0	62.0	61.5	0.041
68.6	59.0	60.6	0.232	-191.3	61.9	72.8	74.0	63.3	62.9	0.041
68.6	61.0	62.4	0.232	-162.5	63.5	72.9	74.0	64.7	64.3	0.041
68.6	63.0	64.2	0.232	-133.9	65.0	72.9	74.0	66.0	65.7	0.041
68.6	65.0	65.9	0.232	-105.7	66.6	73.0	74.0	67.4	67.2	0.041

APPENDIX III

PERFORMANCE OF OVERHEAD RADIANT PANEL AT HEATING CONDITIONS

M_0 (gpm)	T_a (°F)	T_{hws} (°F)	T_{return} (°F)	T_{PM} (°F)	Uo (Btu/hr-ft^2-°F)	Q (Btu/ft^2-hr)
0.22	72	80	78.31	79.44	2.69	19.99
0.22	72	82	79.84	81.26	2.75	25.44
0.22	72	84	81.37	83.07	2.80	31.01
0.22	72	86	82.89	84.86	2.85	36.68
0.22	72	88	84.40	86.65	2.90	42.45
0.22	72	90	85.91	88.42	2.94	48.30
0.22	72	92	87.40	90.19	2.98	54.24
0.22	72	94	88.90	91.96	3.02	60.25
0.22	72	96	90.38	93.71	3.06	66.34
0.22	72	98	91.86	95.46	3.09	72.49
0.22	72	100	93.33	97.20	3.12	78.71
0.22	72	102	94.80	98.94	3.15	85.00
0.22	72	104	96.26	100.67	3.19	91.34
0.22	72	106	97.72	102.40	3.22	97.75
0.22	72	108	99.17	104.11	3.24	104.21
0.22	72	110	100.62	105.83	3.27	110.73
0.22	72	112	102.06	107.54	3.30	117.31
0.22	72	114	103.50	109.24	3.33	123.93
0.22	72	116	104.93	110.94	3.35	130.61
0.22	72	118	106.36	112.63	3.38	137.34
0.22	72	120	107.79	114.32	3.41	144.12

APPENDIX IV

PERFORMANCE OF OVERHEAD RADIANT PANEL AT COOLING CONDITIONS

M_0 (gpm)	T_a (°F)	T_{hws} (°F)	T_{return} (°F)	T_{PM} (°F)	Uo (Btu/hr-ft^2-°F)	Q (Btu/ft^2-hr)
0.22	72	45	51.00	47.20	2.86	70.82
0.22	72	47	52.53	49.01	2.84	65.29
0.22	72	49	54.06	50.82	2.82	59.78
0.22	72	51	55.60	52.64	2.80	54.29
0.22	72	53	57.14	54.45	2.78	48.83
0.22	72	55	58.68	56.27	2.76	43.41
0.22	72	57	60.22	58.10	2.73	38.02
0.22	72	59	61.77	59.92	2.70	32.67
0.22	72	61	63.32	61.75	2.67	27.37
0.22	72	63	64.87	63.59	2.63	22.13
0.22	72	65	66.44	65.44	2.58	16.96

APPENDIX V

ENERGY CONSUMPTION COMPARISON OF SDVAV, ACTIVE AND PASSIVE DESICCANT SYSTEMS AT NO LEAKAGE OPERATION CONDITION

MONTH	Single Duct VAV Air System			Integrated Passive System			Integrated Active System		
	Thermal, MMBtu	Electricity, KW	Primary Energy, MMBtu	Thermal, MMBtu	Electricity, KW	Primary Energy, MMBtu	Thermal, MMBtu	Electricity, KW	Primary Energy, MMBtu
Jan	43.30	1887	80.41	53.60	1763	59.26	27.42	2082	60.82
Feb	33.86	1558	63.87	41.94	1458	49.00	22.62	1746	50.48
Mar	18.51	1550	43.30	23.03	1419	34.80	12.70	1714	37.05
Apr	13.82	1462	35.98	15.16	1313	29.66	10.03	1590	32.08
May	4.81	2009	30.55	3.69	1810	25.45	3.08	1990	27.70
Jun	0.00	4411	52.99	0.00	2989	35.90	6.06	3268	45.33
Jul	0.00	4624	55.55	0.00	3153	37.88	6.48	3458	48.02
Aug	0.00	4654	55.91	0.00	3188	38.31	6.86	3487	48.75
Sep	0.00	3362	40.39	0.00	2759	33.15	5.61	3049	42.24
Oct	11.05	1609	34.06	10.34	1461	26.55	6.55	1721	29.04
Nov	22.82	1688	50.71	25.81	1593	38.14	13.58	1899	40.42
Dec	35.01	1892	69.41	40.81	1809	52.95	22.48	2128	54.90
Total	183.19	30705	613.14	214.37	24716	461.05	143.48	28133	516.83

APPENDIX VI

ENERGY CONSUMPTION COMPARISON OF INTEGRATED ACTIVE DESICCANT SYSTEMS OPERATED AT CV, VAV MODEL, AND CURRENT LEACKAGE CONDITION

MONTH	Active System at Constant Volume			Active System at VAV			Single Duct VAV System		
	Thermal Load (CV), MMBtu	Electricity Load (CV), kWh	Primary Energy Consumption (CV), MMBtu	Thermal Load (VAV), MMBtu	Electricity Load (VAV), kWh	Primary Energy Consumption (VAV), MMBtu	Thermal Load, MMBtu	Electricity Load, kWh	Primary Energy Consumption, MMBtu
Jan	57.12	1985	97.65	52.95	1767	90.29	65.35	2090	112.25
Feb	44.16	1669	76.90	41.33	1465	71.40	50.88	1699	88.25
Mar	21.04	1652	46.47	22.74	1441	46.69	29.04	1622	58.20
Apr	14.98	1575	37.70	15.10	1343	35.47	20.59	1506	45.54
May	5.73	1722	27.40	4.57	1861	27.83	6.83	2016	33.32
Jun	27.61	4124	77.17	19.77	4161	69.77	0.00	4511	54.20
Jul	29.84	4418	82.91	21.49	4466	75.15	0.00	4719	56.69
Aug	30.38	4494	84.37	25.48	5073	86.42	0.00	4705	56.53
Sep	25.42	3700	69.87	17.07	3845	63.27	0.00	3392	40.75
Oct	13.88	1637	37.03	10.58	1492	31.26	15.18	1628	39.80
Nov	30.73	1727	60.19	25.55	1612	52.41	33.86	1747	66.14
Dec	47.57	2015	85.64	40.30	1812	74.20	49.47	1982	89.77
Total	348.46	30717	783.30	296.92	30340.2	724.16	271.19	31617	741.44

VITA

Name: Xiangyang Gong

Address: 4020 New Broad Circle. #308

Oviedo, FL 32765

Email Address: garygong01@gmail.com

Education: B.S., North China Institute of Electric Power, Baoding, China, 1992

M.S., Southern Illinois University, Carbondale, IL, USA, 2003

Ph.D, Texas A&M University, College Station, TX, USA, 2007